POLITECNICO DI TORINO INSTITUTO QUÍMICO DE SARRIÀ

Master's Degree in Biomedical Engineering





Master's Degree Thesis

Design and Nanobody Functionalization of Nanoparticles for Targeted Gene Delivery and Tumor Therapy

Supervisors

Candidate

Prof. Valentina Alice Cauda

Michele Savastano

Prof. Cristina Fornaguera

Dr. Jennifer Fernández Alarcón

Abstract

Among the emerging strategies for cancer theranostics, nanomedicine offers significant promise in advancing both patients' diagnosis and treatment. In combination with nanobodies, nanomedicine can potentially enhance the selectivity and efficiency of a drug or imaging agent delivery, addressing key limitations of current approaches, such as off-target toxicities. The proposed strategy focuses on the use of nanostructured systems of both polymeric, employing $poly(\beta$ -amino esters) (pBAEs) and inorganic, using gold nanoparticles (AuNPs), materials. Both nanosystems were functionalized with anti-EGFR nanobodies aiming at combining selective targeting properties with diagnostic and therapeutic applications. Anti-EGFR nanobody functionalization represents a crucial step in enhancing the selectivity of the nanosystems, as it enables them to recognize the target in a direct and precise manner without significantly altering their physicochemical properties.

Two pBAE polymers, C6 and C32, were synthesized and subsequently modified via Steglich esterification to introduce maleimide groups. This modification provided specific reactive sites for subsequent thiol—maleimide conjugation with engineered nanobodies, ensuring a stable covalent linkage via click chemistry. In parallel, the polymer backbone was end-modified with a cationic peptide (Cys-Arg-Arg-Arg) to enhance the positive charge density and in order to promote efficient electrostatic complexation with nucleic acids. This represents a critical step for nanoparticle formation.

As proof of concept, the incorporation of the newly developed maleimide-pBAEs into a model nanoformulation was shown to be fully compatible with the formation of the polyplexes, their biophysical characterization, and all their in vitro functional features. First, the expression of the EGFR receptor was tested via flow cytometry and western blot analysis *in vitro* using four different human cancer cell lines (MDA-MB-231, BT549, A375 and SK-MEL-28). Thus, MDA-MB-231 cell line was selected as the main system to test both nanoformulations, previously synthesized and characterized, for cytotoxicity and targeting properties of the anti-EGFR NPs.

The preliminary results demonstrated the feasibility of realizing the two nanostructured systems. In vitro studies displayed a possible advantage related to the functionalization with anti-EGFR nanobodies, highlighting the importance of a targeted approach to address the limitations of current treatments. The data obtained constitute a solid basis for the optimization of the nanosystems, with the aim of contributing to the identification of selective and effective novel strategies in oncology

Acknowledgment

Se penso a questi due anni di Magistrale non può che venirmi in mente un rollercoaster di emozioni caratterizzato da una nuova città, nuove amicizie ma sopratutto un percorso universitario di cui sono fiero di aver intrapreso con curiosità e ambizione. Parto dal ringraziare la mia famiglia che mi ha sostenuto al 100% durante questo percorso sia emotivamente che umanamente dato che, anche se a distanza, è sempre riuscita a darmi preziosi consigli su come gestire diverse situazioni. Seguono poi le amicizie che sono nate durante questa avventura, ringrazio gli amici che mi sono fatto durante la mia esperienza al CX: Niccolò, Paola, Filippa, Anna, Simona. Poi ci sono gli amici universitari che mi hanno accompagnato durante il percorso e in particolar modo Andrea, Alessia, Alba, Alessandro e Matilde compagni non solo di risate ma anche fedeli compagni in numerosi lavori di gruppo. In merito all'esperienza di tesi, ringrazio la Professoressa Cauda per aver fatto da tramite e avermi dato la possibilità di intraprendere questa esperienza di tesi magistrale all'estero e la Professoressa Fornaguera per avermi ospitato nei laboratori dell'IQS a Barcellona e avermi permesso di vivere una splendida esperienza formativa. Un ringraziamento va a Jennifer per avermi affiancato come tutor durante tutta l'attività sperimentale, dandomi sempre preziosi consigli. Vorrei poi ringraziare Elisa e Vincenzo, che hanno condiviso la mia stessa esperienza a Barcellona e grazie a loro la distanza e i ritmi in laboratorio si sono rivelati quasi irrilevanti. Un ringraziamento speciale va poi ad Alessandra che in diversi momenti è stato un solido punto di riferimento, che fossero solo giornate NO o il bisogno di consigli utili o anche solo una chiacchierata per staccare il cervello. Ringrazio infine l'esperienza di Torino in generale che ha fatto scoprire lati di me che prima non conoscevo e tenevo nascosti e che ora sono consapevole che sono presenti e so come sfruttarli per migliorare ogni giorno la mia persona.

Contents

Abstract					I
A	ckno	wledgr	\mathbf{nent}		II
Li	ist of	Figur	es		VI
1	Intr	roduct	ion		1
	1.1	Overv	riew of Ca	ancer and tumor microenvironment	1
	1.2	Breas	t carcinor	na	3
	1.3	Melan	oma cano	cer	5
	1.4	Cance	er traditio	onal therapies	7
	1.5	Nano	carriers.		8
	1.6	Shift	to novel t	herapies	11
2	Ain	n of th	e study	and objectives	15
3	Materials and Methods				
	3.1	.1 Materials			
	3.2	Cell li	lines		
	3.3	Methods			
		3.3.1	pBAE N	Nanoparticles	18
			3.3.1.1	Synthesis of pBAE Polymers	18
			3.3.1.2	Protection of Maleimide with Furan	19
			3.3.1.3	Conjugation of Protected Maleimide to pBAE (C6 and	
				C32)	19
			3.3.1.4	Peptide attachment to pBAE chain	20
			3.3.1.5	Deprotection of maleimide	20
			3.3.1.6	Nanoparticles formation	20
			3.3.1.7	Nanobodies functionalization	21
		3.3.2	Gold na	anoparticles synthesis and functionalization	21
			3.3.2.1	Synthesis	21
			3.3.2.2	AuNPs functionalization with PEG-SH and nanobodies	22
		3.3.3	Physico	chemical characterization	22
			3.3.3.1	Nuclear Magnetic Resonance (NMR) for Chemical Struc-	
				ture Verification	22

5	Con	clusio	ns		79
		4.3.3	Transfec	tion efficiency by flow cytometry	76
		4.3.2	Cytotox	icity by MTT Assay at 24 h and 48 h	74
			4.3.1.2	EGFR protein levels by Western blotting	73
			4.3.1.1	Quantification of surface EGFR by flow cytometry $$	70
		4.3.1	EGFR e	xpression profiling across four cell lines	70
	4.3	In vitr	vo evaluat	ion	70
		4.2.2	UV-Vis	absorbance of AuNPs	68
		4.2.1	Hydrody	vnamic diameter via DLS and NTA and zeta potential .	64
	4.2	Gold I	Vanoparti	cles: synthesis and characterization	63
			NTA .		61
		4.1.7	pBAE N	Ps functionalization and subsequent characterization by	
		4.1.6		erization of pBAE NPs at different ratios	57
		4.1.5		de deprotection by ¹ H NMR	53
		4.1.4	-	nalization of the polymer with the arginine-ending peptide	49
				³ C, HSQC, and HMBC NMR	38
		4.1.3		rmation by maleimide attachment and characterization	
		4.1.2		ion of maleimide protection by ¹ H NMR spectrum analysis	
	4.1	4.1.1	-	s and characterization of C6 and C32 by ¹ H NMR	31
'±	4.1			ticles: synthesis and characterization	28
4	Res	ulte or	nd Discu	ssion	28
			3.3.4.4	Western blot	26
			3.3.4.3	Flow Cytometry	26
			3.3.4.2	Cell transfection	25
			3.3.4.1	Cell Viability	24
		3.3.4	In Vitro	studies	24
				ation	23
			3.3.3.5	Agarose Gel Electrophoresis for Nucleic Acid Complex-	
			3.3.3.4	UV-Vis Spectroscopy for Optical Properties	23
				centration	23
			3.3.3.3	Nanoparticle Tracking Analysis (NTA) for Size and Con-	20
			5.5.5.2	and Zeta Potential	23
			3.3.3.2	Dynamic Light Scattering (DLS) for Size Distribution	

6	Future Perspectives	81
Bi	bliography	83

List of Figures

Figure 1	Comparison between normal cell division and malignant cell di-	4
Figure 2	vision	
Figure 3	The five main molecular subtypes of breast cancer	ļ
Figure 4	Schematic overview of the four stages of melanoma	(
Figure 5	Schematic classification of nanocarriers	6
Figure 6	General nanobody structure and types of nanobodies	1
Figure 7	5-amino-1-pentanol (1 H NMR, DMSO- d_{6})	2
Figure 8	1,4-butanediol diacrylate (${}^{1}H$ NMR, DMSO-d ₆)	30
Figure 9	1-hexylamine (${}^{1}H$ NMR, DMSO-d ₆)	3
Figure 10	C6 polymer molecular structure	35
Figure 11	¹ H NMR spectrum of C6 polymer; solvent used: DMSO	3
Figure 12	C32 polymer molecular structure	3
Figure 13	$^1\mathrm{H}$ NMR spectrum of C32 polymer; solvent used: DMSO	3
Figure 14	maleimide-COOH molecular structure	3
Figure 15	$^1{\rm H}$ NMR spectrum of the unprotected male imide-COOH	30
Figure 16	maleimide protection reaction	3'
Figure 17	$^1\mathrm{H}$ NMR spectrum of the furan-protected male imide	38
Figure 18	${\it C6}$ polymer-protected male imide complex molecular structure .	39
Figure 19	C32 polymer-protected maleimide complex molecular structure	40
Figure 20	¹ H NMR spectrum of the reaction between C6 and the furan-	
	protected maleimide	4
Figure 21	$^{13}\mathrm{C}$ NMR spectrum of the reaction between C6 and the furan-	
	protected maleimide	4
Figure 22	HMBC NMR spectrum of the C6-protected maleimide complex	4
Figure 23	HSQC NMR spectrum of the C6-protected maleimide complex	4
Figure 24	$^{1}\mathrm{H}$ NMR spectrum the reaction between C32 and the furan-	
	protected maleimide	4
Figure 25	$^{13}\mathrm{C}$ NMR spectrum of the reaction between C32 and the furan-	
	protected maleimide	4
Figure 26	HMBC NMR spectrum of the C32-protected maleimide complex	4
Figure 27	HSQC NMR spectrum of the C6-protected maleimide complex	4
Figure 28	C6-protected maleimide complex functionalization with CRRR	
	peptide	49

Figure 29	C32-protected maleimide complex functionalization with CRRR	
	peptide	50
Figure 30	$^1\mathrm{H}$ NMR spectra of C6 - protected male imide - CRRR peptide	51
Figure 31	$^1\mathrm{H}$ NMR spectra analysis of C32 - protected male imide - CRRR	
	peptide	52
Figure 32	Deprotection reaction of C6 polymer complex	53
Figure 33	Deprotection reaction of C32 polymer complex	54
Figure 34	$^1\mathrm{H}$ NMR spectra of C6 - male imide - CRRR peptide	55
Figure 35	$^1\mathrm{H}$ NMR spectra of C32 - maleimide - CRRR peptide $\ \ldots \ \ldots$	56
Figure 36	${ m C6}$ / ${ m C32}$ final molecular structure after the recation steps	57
Figure 37	Characterization of C6/C32 pBAE NPs via DLS $\dots \dots$	59
Figure 38	Agarose Gel electrophoresis results	60
Figure 39	Results from pBAE functionalization with anti-EGFR nanobod-	
	ies via NTA	62
Figure 40	AuNPs characterization via DLS	64
Figure 41	AuNPs characterization via NTA results	65
Figure 42	AuNPs characterization via NTA before and after functionaliza-	
	tion with anti-EGFR nanobodies at different ratios	67
Figure 43	AUNPs surface charge characterization via DLS	67
Figure 44	Optimal results from AuNPs functionalization with anti-EGFR	
	nanobodies	68
Figure 45	UV-Vis Results for gold nanoformulations	69
Figure 46	EGFR expression profiling of MDAMB231 cell line	71
Figure 47	EGFR expression profiling of BT549 cell line	72
Figure 48	Wester Blot results of EGFR protein levels in four cell lines	73
Figure 49	MTT assay results of AuNPs treatment	75
Figure 50	MTT assay results of pBAE NPs treatment	76
Figure 51	Transfection Efficiency results via flow cytometer	78

1 Introduction

1.1 Overview of Cancer and tumor microenvironment

Cancer is a heterogeneous disease characterized by the rapid and uncontrolled growth of cells, which leads to tissue degeneration and, in several cases, metastasis to sites distant from primary tumors. At the molecular level, cancer is considered a genetic disease due to increased genomic alterations and epigenetic remodelling [1]. When a single cell acquires a mutation at the genomic level, it confers a selective advantage such as higher proliferation and differentiation in comparison with normal cells [2] [3].

The mutation occurs in genes that, in a physiological context, are responsible for physiological cellular activities and for the regulation of cell growth by the immune system (Figure 1). The first class is represented by proto-oncogenes, which under physiological conditions are responsible for promoting cell proliferation. A mutation in these genes promotes an amplification of cellular proliferation, resulting in uncontrolled cell division [4].

The second class is represented by tumor suppressor genes, such as TP53 or RB1. These genes act by physiologically halting the cell cycle and by preserving genomic integrity. A mutation in these genes, most often characterized by their inactivation, leads to the loss of control of mechanisms responsible for detecting mutations or triggering apoptosis, resulting in the enhanced survival of damaged or mutated cells [5] [6] [7].

A third class is constituted by DNA repair genes. These genes, under normal conditions, maintain genomic stability by correcting spontaneous replication errors or other types of DNA damage. When these pivotal functions are compromised, the mutation rate rises exponentially [8]. This can favour the accumulation of genetic alterations and contributing to the genetic multiplicity of the tumour microenvironment.

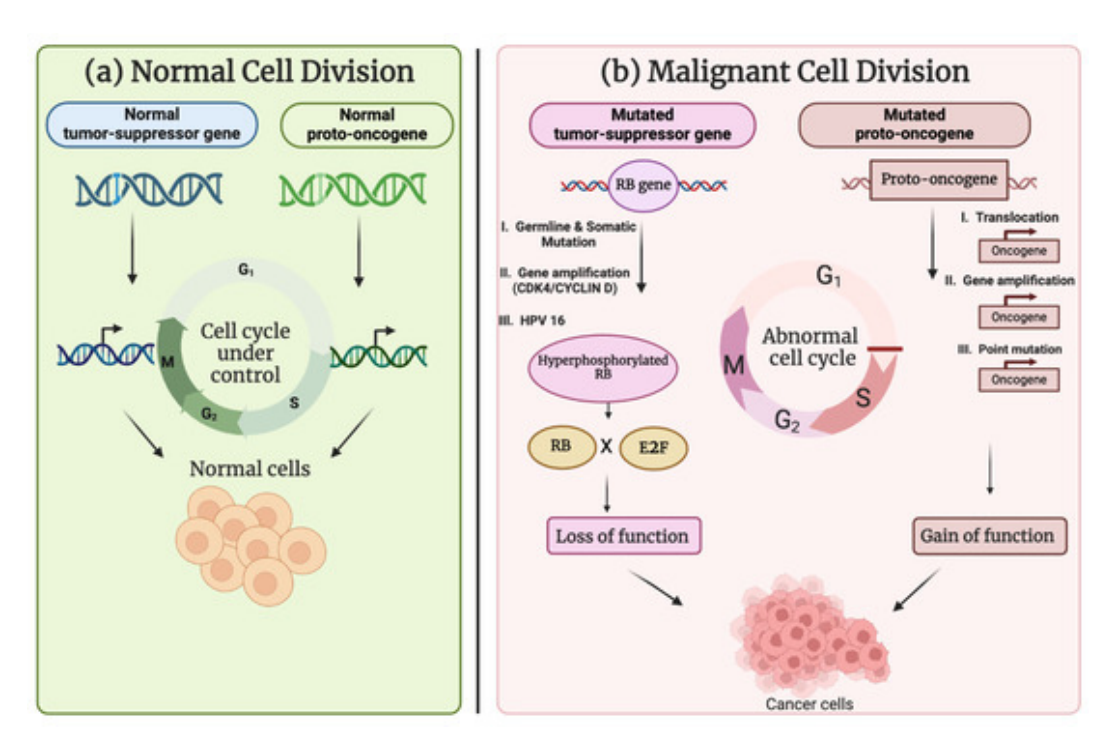


Figure 1: Comparison between normal cell division and malignant cell division. (a) With the support of typical proto-OGs and TSGs, a normal cell division preserves tissue homeostasis by self-renewing and supplying the differentiated cell types inside the tissue through a regulated sequence of cell cycles. (b) A malignant cell division that causes uncontrolled tumor growth when it undergoes excessive cell divisions due to dysregulated function of mutated proto-OGs and TSGs [7].

This advantage allows the mutated cell to proliferate more rapidly and, if not corrected in time by the immune system, it can be passed to the subsequent population. However, tumorigenesis is rarely the result of a single genetic alteration; once the first mutation has been acquired, the new population of mutated cells can develop additional mutations, diversifying the tumour microenvironment (TME) [9]. Each new alteration at the genomic level can confer additional capabilities, such as the ability to evade apoptosis, to receive continuous proliferative signals, or to acquire the capacity to produce extracellular matrix-degrading enzymes, thereby invading surrounding tissues (metastasis) [10] (Figure 2). This multiplicity of genetic mutations plays a central role in tumour progression and represents the starting point of cancer's adaptability and its resistance to therapies [11] [12].

In light of this general overview of cancer genetics and tumor progression, the subsequent sections will specifically focus on breast carcinoma and melanoma, highlighting their molecular characteristics, heterogeneity, and clinical relevance.

They are in fact two different types of tumors, both characterized by the overexpression

of specific receptors that were exploited to design the targeted therapy investigated in this study.

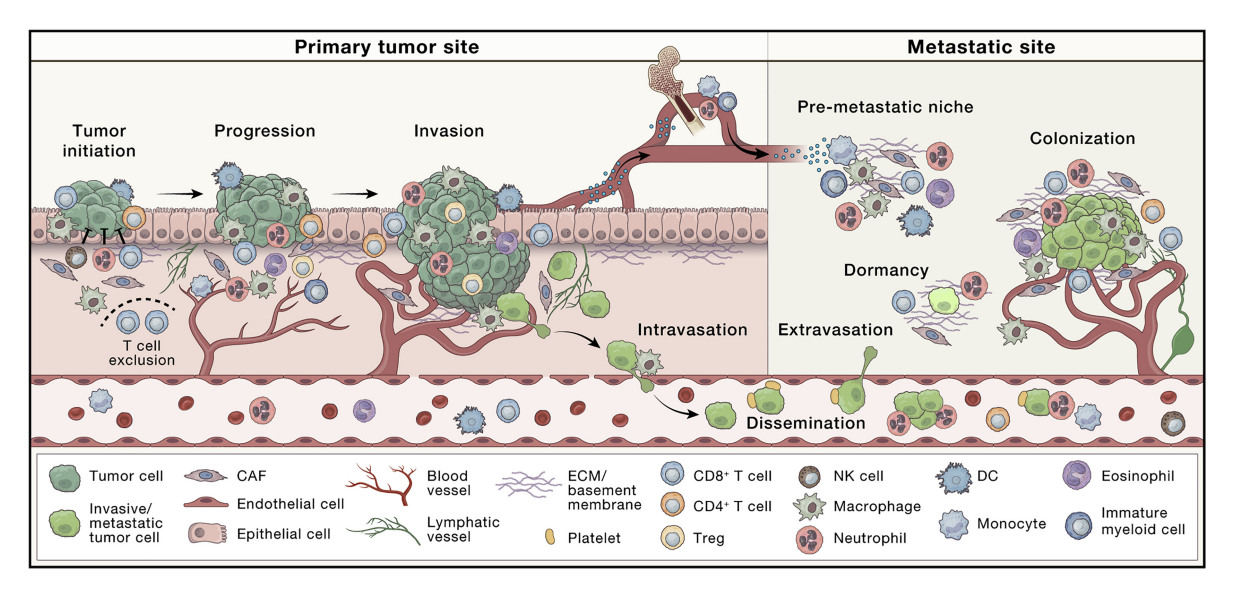


Figure 2: The evolving tumor microenvironment (TME) during all stages of cancer progression is depicted with key representative cell types shown. The TME includes diverse immune cells, cancer-associated fibroblasts (CAFs), endothelial cells, and the extracellular matrix (ECM), among others. These components may vary by tissue type and co-evolve with the tumor as it progresses. The normal tissue microenvironment can constrain cancer outgrowth through the suppressive functions of immune cells, fibroblasts, and the ECM. However, for cancer to advance, it must evade these functions and instead influence cells in the TME to become tumor promoting, resulting in increased proliferation, invasion, and intravasation at the primary site.

Cells and factors of the TME also play a vital role in preparing the premetastatic niche, regulating cancer cell survival in the circulation, and promoting extravasation. During the metastatic stages, the TME helps to control metastatic cell dormancy, emergence from this state, and subsequent metastatic outgrowth [10].

1.2 Breast carcinoma

Breast cancer is characterized by a vast number of genetic mutations, reflecting its complexity and heterogeneity [13], being the most frequent malignancy in women worldwide [14]. Due to heterogeneity there are different classifications of breast cancer based on the gene expression [15], characterized by different prognoses and responses to therapy (Figure 3). In detail, the main subtypes are:

• Luminal A and B, characterized by the expression of hormonal receptors like estrogenic receptor (ER) and progesterone receptor (PR). Patients belonging to this subtype benefit from hormonal therapies but differ in tumor proliferation and aggressiveness. Indeed, Luminal B tumors show a higher proliferation rate and a less favourable prognosis.

- Human epidermal growth factor receptor 2 (HER2)-positive, characterized by the overexpression of the HER2/ErbB2 tyrosine kinase receptor.
- Triple-negative breast cancer (TNBC): this is characterized by the absence of ER, PR, and HER2 receptors. This subtype, which represents about 10–15% of breast carcinomas, is associated with particular aggressiveness, high metastatic potential, and especially the absence of consolidated therapeutic targets. Precisely in this context, the importance of additional surface receptors such as epidermal growth factor receptor (EGFR), frequently overexpressed in TNBC and considered an alternative therapeutic target, emerges [16] [17].

Focusing the analysis on EGFR (ErbB1 or HER1), it belongs to the ErbB family of tyrosine kinase receptors, which also includes HER2, HER3, and HER4. EGFR is a transmembrane receptor with intracellular tyrosine kinase activity, activated by binding to specific ligands such as EGF and TGF-alpha. In a physiological context, EGFR activation promotes proliferation, survival, and cellular differentiation, but if mutated or overexpressed, as previously mentioned, it can lead to the onset of several cellular dysfunctions [18]. Accordingly, in triple-negative breast carcinoma, this receptor is often overexpressed or hyperactivated, a process that determines the constant activation of downstream biochemical pathways such as the RAS/RAF/MEK/ERK cascade (involved in proliferation) and the PI3K/AKT/mTOR pathway (linked to survival and resistance to apoptosis) [19].

The overactivity of the EGFR receptor is responsible for the uncontrolled growth of affected cells but also promotes angiogenesis and invasive processes through the overproduction of enzymes that degrade the extracellular matrix, such as metalloproteases, and various pro-angiogenic factors [20]. These peculiarities make EGFR a crucial oncogenic driver in specific subtypes of breast carcinoma and a therapeutic target to be considered.

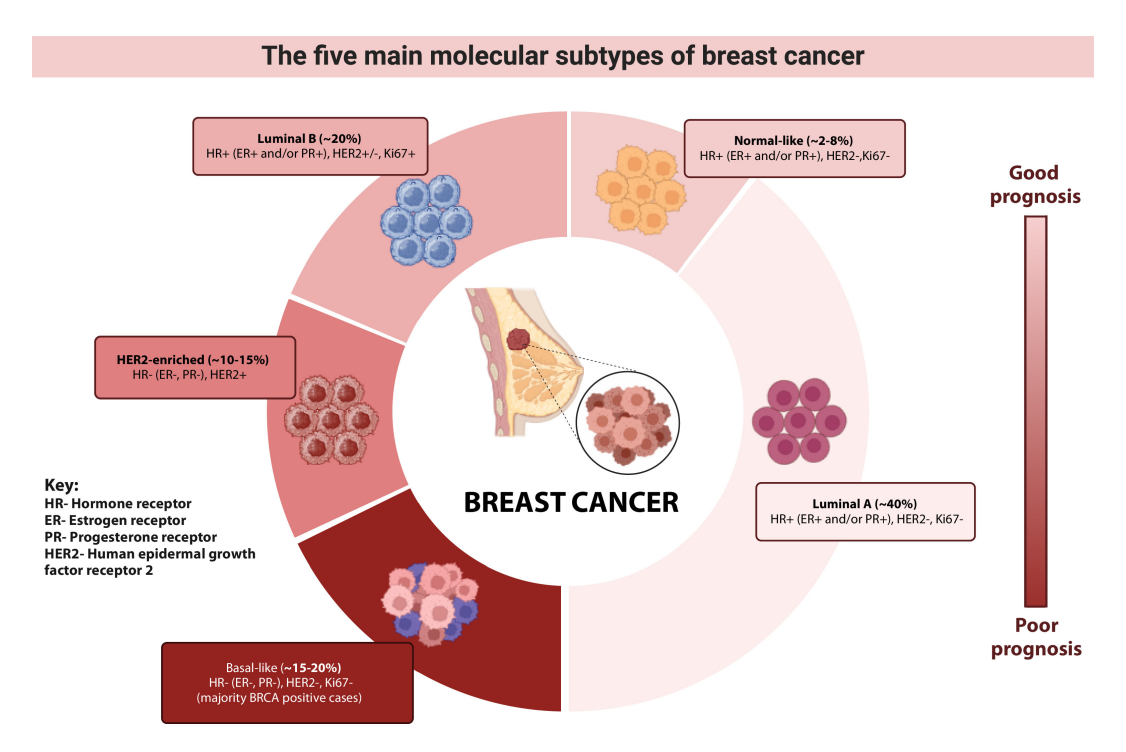


Figure 3: The five main molecular subtypes of breast cancer. Breast cancer tumors are clinically characterized based on the presence/absence of various marker combinations. These markers include estrogen receptor, progesterone receptor, human epidermal growth factor receptor 2, and the proliferative marker Ki-67. Varying marker combinations constitute the breast cancer subtype as being either luminal A, luminal B, basal-like, human epidermal growth factor receptor 2-enriched, or normal-like. This clinicopathologic classification allows for the use of optimal treatment regimens as well as prediction of the risk of recurrence in a clinical setting [13].

1.3 Melanoma cancer

Melanoma is a malignant neoplastic tumor that arises from melanocytes, a cell type specialized in the synthesis of melanin and that is predominantly located in the epidermis.

Melanocytes exposure to different environmental, genetic, and biological factors, such as ultraviolet (UV) radiation from the sun or genetic mutations in key genes, exhibits a high mutational burden, with numerous genetic alterations driving its development and progression. From a biological point of view, melanoma is a key model of phenotypic plasticity, since the cells can oscillate between "proliferative" states and "invasive" states, with state transitions assisted by biochemical signals coming from the TME [21] [22].

This mechanism of adaptation can lead to drug resistance to standard treatments and the consequent progression of the tumour and metastasis. From a clinical point of view, the evolution of melanoma most often follows a phase of radial and superficial growth, followed by a "vertical" phase characterized by invasion of the dermis [21] (Figure 4). Melanoma is a tumour in which the interactions of the microenvironment play a crucial role [23].

The expression of EGFR receptor plays a function-dependent role on the phenotypic state of the melanoma and on environmental/therapeutic stimuli [24] [25]. Indeed, conditions of hypoxia and acidosis modulate the set of receptors (including EGFR), the extracellular matrix and metalloproteases facilitate invasion, and myeloid cells and tumour-associated macrophages establish an immunosuppressive and pro-angiogenic condition [26].

In such a dynamic system, EGFR is integrated and although it is not always the main cause of the onset of the tumour, it is most often considered as a trigger that the tumour itself uses to grow, migrate, or survive therapy.

Stages of Melanoma

Stage II Localized to epidermis - <1 mm thick Stage II Disease spread to lymph nodes or nearby skin Stage IV Metastasis to other internal organs - Lymph node involvement Normal lymph node Blood vessel

Figure 4: Schematic overview of the four stages of melanoma and its metastatic mechanism (www.biorender.com template)

1.4 Cancer traditional therapies

In oncology, standard therapies aim to eliminate neoplastic malignancies by implementing a single treatment or a combination of multiple treatments such as surgery, radiotherapy, and chemotherapy, which represent the three pillars [27].

Surgery provides localized control of the tumour and it consists in removing as much neoplastic material as possible from the patient's body. It includes different modalities of physical removal such as cryotherapy, laser therapy, hyperthermia, and photodynamic therapy. The major limitation related to choosing classic surgery lies in the inability to eliminate microscopic disease that may be found around the main tumour mass and that cannot be precisely removed with conventional surgical instruments. Another important limitation is the inability to remove any metastases of the primary tumour.

Regarding radiotherapy, it uses high-energy radiation (mainly X-rays) in order to eliminate as many malignant cells as possible by damaging them at the DNA level. A first concern linked to this treatment is the possible damage to the surrounding tissues and the inability to eliminate and detect cells that are not visible with imaging techniques (e.g., near the lymph nodes or metastatic cells that are located in areas distant from the treatment area).

Finally, chemotherapy uses antineoplastic drugs (interfering with cell division) that are administered systemically. An important limitation linked to the modality of administration is the high toxicity and low selectivity toward healthy cells and the inability of most drugs to overcome the body's physiological barriers (e.g., the blood-brain barrier) and therefore the inability to reach certain areas of the body.

The main limitations of standard therapies in oncology is the poor selectivity. In addition, this picture fits into an even more complex biological context. Tumor heterogeneity and plasticity can cause the survival of the most fit tumor cells after any therapeutic treatment, leading to differentiation and clonal multiplicity. In addition, the TME itself, characterized by hypoxic zones and acidic environments, makes drug penetration more difficult (in chemotherapy) and compromises their activity, most often inactivating them. While remaining fundamental, it is therefore not surprising that standard therapies are most often insufficient towards more aggressive tumor forms or those characterized by high multiplicity and that turn out not to be targetable by conventional drugs [28].

1.5 Nanocarriers

In the context of precision therapy, nanocarriers are transport systems at the nanoscale level designed to selectively deliver active agents, small-molecule drugs, therapeutic agents, or nucleic acids to the pathological site, modulating their absorption, distribution, release, and interaction with target cells. Nanovectors are the key system for targeted delivery and share three fundamental features: circulating systemically without interacting with non-target organs or the immune system, overcoming tissue barriers, and finally releasing the cargo into the correct intracellular compartment, overcoming endosomal entrapment. Depending on the target and on the specific characteristics of the tumor site of interest, a different type of nanocarrier is chosen not only in terms of the modality of encapsulating the therapy but especially considering the materials constituting the particle itself, which must interface directly with the TME. Thus, nanocarriers can be divided in two main groups based on the materials composition, organic and inorganic (Figure 5).

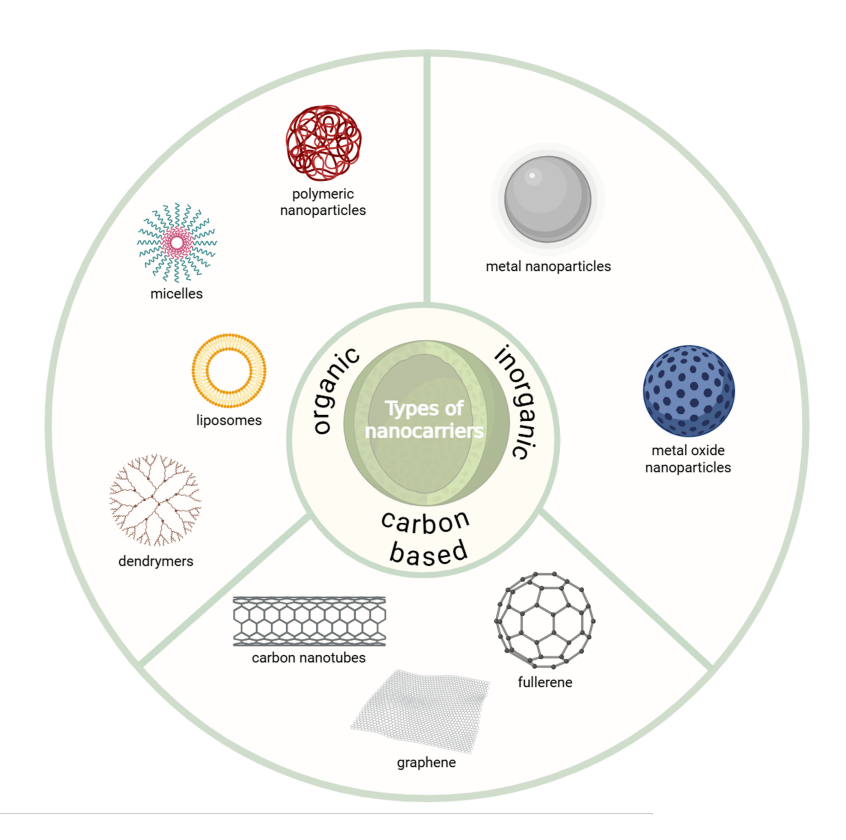


Figure 5: Classification of nanocarriers based on their composition. Organic nanocarriers include micelles, liposomes, dendrimers, and polymeric nanoparticles. Inorganic nanocarriers comprise metallic and metal oxide nanoparticles. Carbon-based nanocarriers include carbon nanotubes, fullerenes, and graphene. (figure made with www.biorender.com)

Organic nanocarriers include lipid systems and polymeric systems. These two types of vectors share features such as protecting the therapeutic cargo, prolonging its residence time in circulation, and ensuring an effective release in a selective way toward the target. Inside polymeric nanoparticles there are the poly(β -amino ester)s (pBAEs), which are synthetic cationic polymers typically obtained by Michael addition between amines (primary or secondary) and diacrylates. The ester linkage along the main chain renders these polymers hydrolytically degradable under physiological conditions, whereas the amino groups confer a cationic character and buffering capacity over a range useful for exploiting endosomal escape once they are internalized into the target cell.

From this initial overview, they emerge as a class of non-viral carriers engineered to balance transfection efficiency with a biocompatibility profile (higher than other classes of polymers used for nanocarrier formulation, such as PEI, previously mentioned). In addition, they are highly modular from a chemical standpoint, leaving room for engineering adaptations to meet different needs in the field of nanomedicine [29] [30].

The key advance, developed and consolidated by the host group, consists in adding oligopeptides to the polymer chain ends (OM-pBAE, oligopeptide-modified pBAE). End groups with peptides such as arginine/lysine enhance electrostatic interaction and membrane adhesion, whereas histidine increases complex stability and endosomal buffering. By modulating different peptides in controlled proportions, a fine-tuning of the mechanical, physical, and biological properties of OM-pBAE-based systems is obtained. Recent studies have also shown that the stoichiometry and combination of such peptide terminations have a significant impact on adhesion, stability, cargo internalization, and cargo release, allowing the carrier to be tailored to the biological context of interest and opening a wide spectrum of applications [31]. pBAEs can electrostatically interact with nucleic acids such as plasmids, mRNA, siRNA or miRNA to form polyplexes. With regard to the biodegradability profile of the main backbone, it facilitates a more favorable cytotoxicity profile compared with non-degradable polymers, and the N/P ratio (amines/phosphate groups) governs properties such as size, PDI, zeta potential, and stability [30].

In addition, the structure of pBAEs lends itself to the insertion of additional moieties at the chain ends or alongside chains (e.g., maleimide, azides, alkynes), enabling conjugations based on the concept of click chemistry; these reactions are rapid, selective, and carried out under mild conditions (without requiring reaction catalysts or high temperatures). By exploiting click chemistry to anchor maleimide onto the pBAE backbone, it

is then possible to attach a range of ligands useful for specific targeting in nanomedicine. Thiol—maleimide coupling represents the standard for site-specific attachment of thiolated ligands (e.g., nanobodies with engineered cysteines or peptides) to the surface of nanocarriers. This allows the formation of thioether bonds that are stable under physiological conditions. This approach is well established for polymeric nanocarriers and has been shown to preserve binding affinity and increase receptor-mediated uptake [32].

Meanwhile, inorganic nanocarriers are composed on metals, metal oxides, silica, semi-conductor materials (e.g., quantum dots), and, at times, carbon allotropes. Most of the time, inorganic carriers, unlike those of organic nature, do not encapsulate a cargo inside but instead operate through surface adsorption and covalent conjugation. The reason why they can prove to be crucial tools in the field of oncology is that they exhibit unique features not obtainable with organic carriers. Indeed, there are optical, magnetic, and electronic properties that enable therapeutic and diagnostic functions such as photothermal therapy, radio sensitization, magnetic hyperthermia, imaging, and, finally, theranostics. In particular, gold nanoparticles (AuNPs) are colloidal systems characterized by unique opto-plasmonic properties. The collective oscillation of conduction electrons at the metal surface (localized surface plasmon resonance, LSPR) amplifies light absorption and scattering, making gold a material that enables optical diagnostics, imaging, and photoactivated therapies. This versatility, combined with a highly tunable surface chemistry, makes AuNPs a promising and useful tool for therapy and theranostics in oncology.

To prepare colloidal spheres with diameters ranging from 10 to 50 nm, normally it is used the Turkevich reduction, where the citrate reduces Au3+. It is an economical, scalable, and highly reproducible method [33]. Regarding the functionalization, the gold—thiol bond allows the anchoring of thiolated PEG conjugates and other molecules to increase colloidal stability and reduce opsonization, thereby enhancing stealth properties to evade clearance processes. This bond also makes it possible to introduce terminal functions with specific ligands (e.g., nanobodies) in order to confer specific targeting properties to gold nanoformulations.

The main therapeutic applications are phototherapy, radio sensitization, and combined approaches. In phototherapy, AuNPs irradiated at their LSPR dissipate light energy as heat, raising the local temperature of the target tissue to cytotoxic levels and inducing cell death by necrosis or apoptosis. Radio sensitization, by contrast, consists in exploit-

ing the optical properties of gold particles which, as metals, intensify photoelectric and scattering interactions with X-rays, increasing the therapeutic effect and the local dose absorbed in the tumor area. In this sense, AuNPs can reduce the required doses or enhance the effectiveness of radiotherapy [34].

Finally, AuNPs biodistribution in mice strongly depends on hydrodynamic diameter, shape, surface charge, and coating. Spherical particles of 20–80 nm tend to be captured by the reticuloendothelial system or undergo renal clearance. In this context, PEGylation, a solution adopted in the present work, reduces opsonization and prolongs half-life [35] [36]. Moreover, metallic gold is considered relatively biocompatible, but toxicity depends strongly on surface chemistry and on the dosage of the formulation.

1.6 Shift to novel therapies

Considering the principal limitations that characterize standard therapies, research has moved toward new targeted therapies characterized by a complete change of paradigm. In particular, interventions are undertaken with the objective of maximizing selective efficacy, while minimizing systemic effects. Thus, we speak of drugs or other substances designed to block tumor growth and spread by interfering with specific molecules that are involved in the growth, progression, and expansion of the tumor itself. In this sense, two conceptual components must be kept distinct: the targeted mechanism of action (e.g., inhibiting a driver kinase or blocking a receptor) and the targeted delivery, which consists in bringing the therapeutic agent to the cells that express the target of interest. In most cases, the most promising results are obtained when these two features operate in parallel. Speaking of the mechanism of action, the following fall within targeted therapies: small-molecule inhibitors of tyrosine kinases or intracellular pathways, monoclonal antibodies against receptors or ligands (EGFR, HER2, VEGF, VEGFR), antibody-drug conjugates [37], and, more recently discovered and used, targeted protein degradation systems and therapeutic oligonucleotides directed at oncogenes or specific pathways. This type of intervention is a form of medicine that uses information related to the patient's specific genes and proteome to prevent, diagnose, and treat the problems of interest at the level of the organism and in an extremely targeted manner. Reliance has been placed on the so-called enhanced permeability and retention effect (EPR), which exploits the abnormal revascularization of blood vessels in the TME with the passive accumulation of nanocarriers and with lymphatic drainage (inefficient in the tumor environment most of the time) that prevents the ejection. The

problem is that the EPR is highly heterogeneous between tumors and patients: it depends on the type of tumor, on the stage of growth, on the TME, and on the individual patient [38]. Due to these issues, research has turned to active targeting that exploits the functionalization of carriers' surface with ligands (antibodies, nanobodies, peptides) that specifically recognize receptors overexpressed on neoplastic cells [39]. Depending on the nature of the vector, the binding activates the consequent receptor-mediated endocytosis and promotes the accumulation of the therapy inside the target cell.

Targeted therapies are based on the interplay between a molecular target, typically a receptor or antigen (aberrantly expressed in cancer) and a targeting agent which can be a ligand designed to direct therapeutic systems specifically toward that target. The target provides the biological rationale, representing the molecular alteration whose modulation can alter the course of the disease. On the other hand, the targeting agents ensures that therapeutic molecules or nanosystems selectively reach the diseased cells, improving efficacy while limiting off-target effects. This dual relationship defines the foundation of precision medicine: identifying the right molecular abnormality and pairing it with a selective ligand capable of addressing it effectively.

Within this framework, nanobodies are employed as targeting ligands: their role is to confer selectivity to nanosystems by guiding them to tumor-associated receptors, while the therapeutic effect is provided by the payload delivered rather than by the nanobody itself (Figure 6). In particular, nanobodies derive from the variable domain of "heavy-chain-only" antibodies of the camelid family, in which the variable domain (VHH) is autonomous [40]. They occupy a technological niche of great interest since they combine high affinity/specificity with small size (12–15 kDa), thermal and chemical stability, good solubility, and, above all, a high degree of engineerability that has no equivalent within the class of conventional antibodies. In general, compared with IgG, Fab, or scFv, VHHs often display a longer and more flexible CDR3 that allows access to epitopes that are difficult to reach for bulkier molecules. Moreover, high solubility and ability to avoid aggregation, are features that explain why nanobodies can prove to be versatile tools both as drugs and as targeting moieties for nanovectors [41] [42].

Theoretically, any surface antigen is targetable, but the most useful candidates combine tumor overexpression with favourable accessibility. Beyond the ErbB family (EGFR/HER1, HER2, HER3), epithelial antigens (for example EpCAM, MUC1, TROP-2) or microen-

vironment markers such as VEGFR2 are frequent. The choice therefore depends on the stage of disease and, above all, on the stability of the target during therapy. In the present work, the choice of the EGFR receptor proves to be the right target for multiple reasons. Specifically, in TNBC EGFR is most often overexpressed and present on the surface, with rapid endocytosis after binding. In melanoma, by contrast, EGFR is variable but likewise is most often expressed in configurations accessible to a highly specific ligand such as an anti-EGFR nanobody.

From a pharmacokinetic point of view, the reduced dimensions favour rapid penetration into tissues but entail accelerated renal clearance. For systemic use in free form (not linked to any carrier), the half-life can be extended with albumin-binding strategies or PEGylation. It is for this reason that the choice of the nanobody specific to the target of interest is followed by the choice of an appropriate nanovector. In the context of vectors (which can be inorganic or organic nanoparticles), this pharmacokinetic limitation is mitigated since the nanobody is not circulating in free form but is functionalized onto the nanocarrier. Consequently, the half-life of the complex is dominated by the pharmacokinetic profile of the vector, while the nanobody simply confers the crucial properties of molecular recognition and triggers receptor-mediated endocytosis.

Although nanobodies can also be developed as independent therapeutic agents, in this thesis they are employed exclusively as targeting moieties, with the aim of enhancing the specificity of nanosystems toward defined molecular targets. The distinction between the therapeutic cargo and the targeting ligand is fundamental and provides the rationale for their integration within the nanosystems designed in this work. It is precisely to address the need for greater selectivity that anti-EGFR nanobodies are employed and subsequently conjugated with nanocarriers.

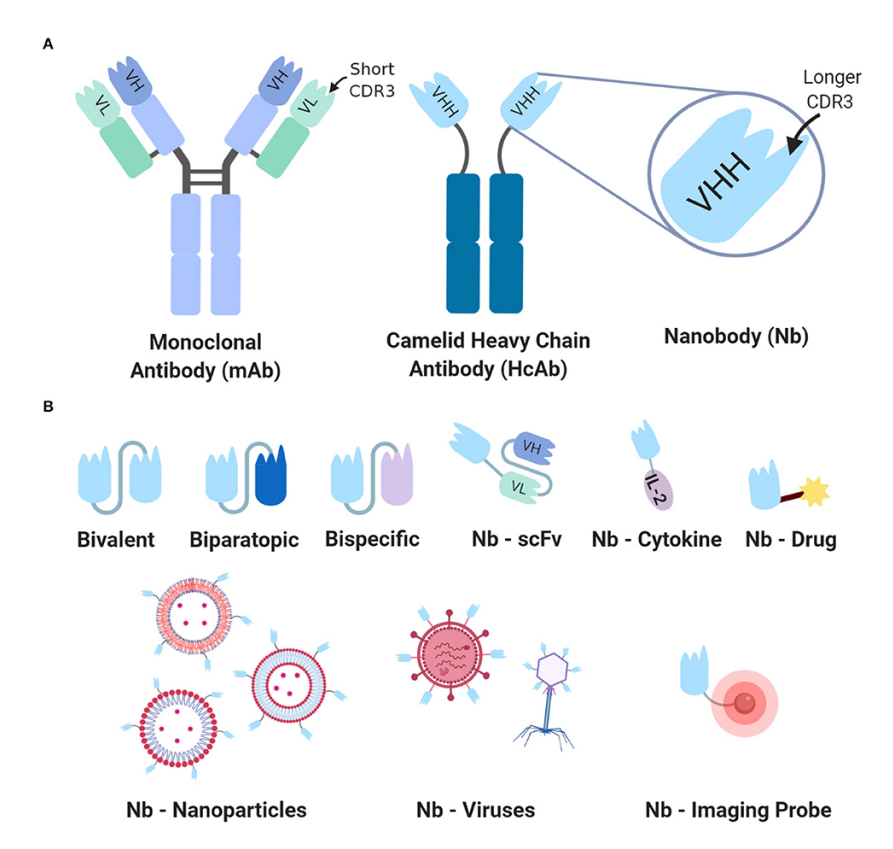


Figure 6: General nanobody structure and types of nanobodies. (A) Comparison of the monoclonal antibody (mAb) vs. heavy chain antibody (HcAb) to highlight the structural differences of their respective antigen binding regions. The VHH/Nanobody has a much longer CDR3 loop compared to that of the VH-VL domains in mAbs, providing antigen affinity and access to hidden epitopes. (B) A generalized overview of the types of engineered nanobodies to demonstrate how their high modularity enables various modifications. For enhanced antigen avidity, bivalent nanobodies can be created by connecting two identical nanobodies with a linker peptide. Biparatopic nanobodies are a fusion of two nanobodies targeting unique epitopes for the same antigen, with decreased dissociation from the target antigen. Bispecific nanobodies are composed of two nanobodies targeting different antigens and are often utilized as T cell engagers. Nanobodies can also be conjugated to other cancer therapies, nanoparticles, viral vectors, or to imaging agents for targeted tumor visualization. CDR3, complementarity-determining region 3; scFv, short-chain variable fragment; IL-2, Interleukin-2 [40].

2 Aim of the study and objectives

Given this background, in the current work it is proposed two delivery systems using two types of nanomaterials: soft nanomaterials and hard nanomaterials. Related to soft nanomaterials, pBAEs have been chosen for their tunability in terms of functionalization, allowing them to bind different type of molecules. Also, pBAEs enable endosomal escape by undergoing protonation at the lower pH of the endosomal compartment, leading to osmotic pressure buildup due to buffering, which causes endosomal disruption [43]. With deeper insight, their natural cationic charge can be tuned and used as a crucial tool to control electrostatic interaction for high efficiency complexation of anionic cargo, such as nucleic acids [44].

The first aim is to functionalize the pBAE polymers with maleimide molecules via a Steglich esterification to perform click chemistry with thiol-ending nanobodies. Therefore, the combination of pBAE, carrying genetic material, and nanobodies for selective binding can be a useful strategy to build a promising system for targeted gene delivery. Thereafter, in vitro validation assays were performed in order to test the behaviour towards target cells, as well as assessing the cytotoxicity of the nanoformulations.

In parallel, metallic nanoparticles have been used as an effective tool in terms of therapeutic effects due to their several chemo-physical properties. In particular, gold nanoparticles (AuNPs) have been selected as the model of this study thanks to their optical properties and their affinity towards thiol-containing molecules.

The second aim is to functionalize the AuNPs directly with the anti-EGFR nanobodies for selective targeting towards cancer cells overexpressing this receptor.

Finally, in vitro validation tests were carried in order to assess cytotoxicity of the nanoformulations.

In general, several chemical modifications were introduced to optimize nanoparticle formation and genetic cargo complexation. The rationale of this work resides in the functionalization of both nanosystems with anti-EGFR nanobodies. This step is crucial, as it confers tumor-specific recognition to the formulations, turning them from generic nanocarriers into targeted therapeutic tools. In this way, nanobody conjugation represents the unifying element of both delivery strategies, enabling a direct comparison of their potential in the selective treatment of cancer.

In light of this, two main objectives were defined:

- Synthesis, physicochemical characterization and in vitro validation of a new polymer platform to perform click chemistry aiming at the anti-EGFR nanobodies' conjugation.
- Synthesis and physicochemical characterization of gold nanoparticles and their functionalization with anti-EGFR nanobodies.

3 Materials and Methods

3.1 Materials

Chemicals and reagents

5-Amino-1-pentanol (>92%), 1-Hexylamine (>99%), 1,4-butanediol diacrylate (>90%), maleimide-COOH (Sigma-Aldrich, USA); furan anhydrous, toluene, dichloromethane anhydrous (CH₂Cl₂), dimethyl sulfoxide (DMSO), acetonitrile (HPLC grade), ethyl acetate (ACS grade), hydrochloric acid (HCl, 0.1 M), 2-mercaptoethylamine hydrochloride (2-MEA, \geq 97%), agarose, tris-acetate-EDTA buffer (1× TAE), GelRed nucleic acid stain, tetrachloroauric(III) acid trihydrate (HAuCl₄·3H₂O, 99.9% trace metals basis), and trisodium citrate dihydrate were purchased from Sigma-Aldrich. PEG-SH (M.W. \approx 5 kDa) was purchased from Biopharma. Dulbecco's Modified Eagle Medium (DMEM), RPMI-1640 without L-glutamine, fetal bovine serum (FBS), phosphate-buffered saline (PBS, pH 7.2), penicillin-streptomycin and glutamine were purchased from Gibco. Trypsin-EDTA solution, RIPA buffer, Protease inhibitor cocktail (PIC), TBST components (Tris-buffered saline, Tween-20), thiazolyl Blue Tetrazolium Bromide (MTT) and paraformaldehyde (PFA, 4%) were purchased from Sigma-Aldrich. PVDF membrane (Immobilon-P) was purchased from Merck Millipore. Lipofectamine[®] 2000 was purchased from Thermo Fisher Scientific. The antibody anti-EGFR (sc-120) was purchased from Santa Cruz Biotechnology.

Arginine- and histidine-end-modified poly(β -amino ester) (pBAE) polymers used in this thesis (referred to as R and H, respectively), were synthesized by the Group of Materials Engineering (GEMAT) at the Institut Químic de Sarrià (Barcelona, Spain), following a two-step procedure.

Laboratory Equipment

96-well flat-bottom transparent polystyrene plates (Greiner Bio-One, Germany); 15 mL and 50 mL Falcon tubes (Corning, USA); Disposable plastic cuvettes (Malvern Instruments, UK).

Instrumentation

Bruker Avance 400 MHz NMR spectrometer (Bruker, Germany); Malvern Zetasizer Nano ZS (Malvern Panalytical, UK); Malvern NanoSight NS300 (Malvern Panalytical, UK); Tecan Infinite 200 Pro microplate reader (Tecan, Switzerland); AmershamTM ImageQuantTM 800 biomolecular imager (Cytiva, USA); Flow cytometer (Novocyte, ACEA Bioscience).

3.2 Cell lines

Four different human cancer cell lines were employed in this study:

- MDA-MB-231 (human breast adenocarcinoma, triple-negative; ATCC[®] HTB-26[™], USA).
- BT-549 (human breast ductal carcinoma, triple-negative; ATCC® HTB-122 $^{\text{\tiny TM}}$, USA).
- A375 (human malignant melanoma; ATCC[®] CRL-1619[™], USA).
- SK-MEL-28 (human malignant melanoma; ATCC® HTB- $72^{\text{\tiny TM}}$, USA).

3.3 Methods

3.3.1 pBAE Nanoparticles

3.3.1.1 Synthesis of pBAE Polymers

Poly (beta-amino ester) polymers C6 and C32 have been synthesized via Michael-type addition reactions [45].

C6 polymer synthesis

5-amino-1-pentanol (0.1964 g, 1.00 equiv) and 1-hexylamine (0.1964 g, 1.00 equiv) were mixed in a 25 mL round-bottom flask under magnetic stirring. Subsequently, 1,4-butanediol diacrylate (0.9025 g, 2.40 equiv) was added to the mixture of 5-amino-1-pentanol and 1-hexylamine. The mixture was maintained under agitation at 90 °C for 20 hours. Finally, the flask was removed from heating and cooled down at room temperature. The polymer was stored at 20 °C for further steps.

C32 polymer synthesis

For the synthesis of C32, 5-amino-1-pentanol (4.2734 g, 1.00 equiv) was put into a 25 mL round-bottom flask and stirred. This step is followed by the addition of 1,4-butanediol diacrylate (9.8584 g, 1.20 equiv). The mixture was maintained at 90 °C for 20 hours. After cooling down to room temperature, the polymer was stored at -20 °C for further use.

3.3.1.2 Protection of Maleimide with Furan

The following reaction was made to prevent the undesired attachment of the peptide to the maleimide. Thus, the maleimide-COOH was protected via a Diels-Alder cycloaddition with furan [46]. The aim was to protect the maleimide from undesired reactions until it binds the nanobody.

Maleimide COOH (500 mg) was dissolved in 15 mL of anhydrous toluene in a round-bottom flask, maintaining the reaction under anhydrous conditions. Furan (0.644 mL, 0.603 g, 3.00 equivalents) was added dropwise using a syringe while stirring. The solution was maintained at 60 °C for 6 hours.

3.3.1.3 Conjugation of Protected Maleimide to pBAE (C6 and C32)

The attachment of the protected maleimide COOH to the side chains of pBAE polymers (C6 or C32) terminating with a hydroxyl group was performed via Steglich esterification using DCC/DMAP coupling chemistry under anhydrous conditions.

Starting with C6 polymer, C6 (100 mg) was weighed and dissolved in 2 mL of anhydrous dichloromethane (CH₂Cl₂) in a 20 mL round-bottom flask. Furan-protected maleimide COOH (23.7 mg) was added to the mixture under continuous stirring. The mixture was cooled down in ice for 15 minutes.

In parallel, dicyclohexylcarbodiimide (DCC, 10.3 mg) and 4-dimethylaminopyridine (DMAP, 7.3 mg) were weighed and dissolved in 2 mL of anhydrous CH₂Cl₂ in a 20 mL vial. Then, the DCC/DMAP solution was added dropwise to the cooled C6/maleimide mixture under agitation and at room temperature for 18 hours.

Then, the mixture was filtered using a 0.45 μ m filter into a vial to remove DCC salts

and excess DMAP. The solvent was evaporated under reduced pressure using a rotary evaporator. Then, the product was dissolved in an acetonitrile:ethyl acetate solution (ACN:EtOAc, 1:2, v/v).

In order to completely remove DCC salts and DMAP residues, the solution was frozen at -20 °C for 4 hours, then filtered through a 0.45 μ m filter. These steps were repeated at least twice, or until no visible precipitate remained. Finally, maleimide-functionalized polymer was stored at -20 °C until further use.

3.3.1.4 Peptide attachment to pBAE chain

First, it was needed to exchange the TFA groups presented on the amino groups of the CRRR peptide with HCl (0.1M). CRRR peptide (105.2 mg) was weighed in a 50 mL falcon. Subsequently 20 mL of HCl (0.1M) were added to dissolve the peptide completely. Finally, the mixture was allowed to freeze-dry overnight.

For the attachment of the peptide after salt change to the C6, CRRR (54.7 mg) was dissolved in 1.3 mL of anhydrous DMSO while C6 (105.7 mg) was dissolved separately in 1 mL of anhydrous DMSO. After putting the polymer into a round-bottom flask, the CRRR solution was added dropwise into the C6 solution. For the attachment of the peptide to C32 chain, the procedure is identical to C6 with the only difference that 54.5 mg of CRRR peptide were weighed.

3.3.1.5 Deprotection of maleimide

In order to have the maleimide deprotected and ready to bind the nanobody, it was needed to perform the deprotection of the maleimide. The compounds were dissolved in DMSO in a round-bottom flask and heated at 110 °C for 4 hours.

3.3.1.6 Nanoparticles formation

According to the standard pBAE particle synthesis, which employs a 60% R and 40% H composition, R was replaced by the previously synthesized C6 and C32 polymers that had been functionalized with maleimide and cationic peptides. Two distinct nanoparticle formulations were engineered, based on the C32 and C6 pBAE backbones, respectively; both were assembled by electrostatic complexation with pGFP plasmid DNA.

On the basis of the polymer employed (C6-H or C32-H) and the selected genetic cargo, a series of formulations was prepared in which the ratio of pBAE to genetic material was increased in a controlled sequence: 1:25, 1:50, 1:75, and 1:100. Each formulation was then characterized for hydrodynamic diameter, polydispersity index, and zeta potential, and the conditions showing the most favourable profiles were selected for subsequent optimization and biological evaluation.

3.3.1.7 Nanobodies functionalization

First, the anti-EGFR nanobodies (1.7 mg/mL) required to be reduced. Thus, disulfide bonds were cleaved to generate free thiol groups suitable for subsequent functionalization. A solution of 2-mercaptoethanol (2-MEA, 100 mM) was prepared by dissolving 2-MEA (0.0078 g) in 1.0 mL of Milli-Q water. Then, 2.27 μ L of this solution were added to 20 μ L of the anti-EGFR nanobody solution, which was then incubated on ice.

After the reduction, for 60 μ L of pBAE nanoparticle suspension, three volumes of the reduced nanobody solution were evaluated: 1.0 μ L, 2.6 μ L, and 5.0 μ L. The formulations were subsequently incubated on ice.

3.3.2 Gold nanoparticles synthesis and functionalization

3.3.2.1 Synthesis

For the following protocol, the Turkevich method was employed to properly synthesize gold nanoparticles (AuNPs) [33]. Trisodium citrate (0.01 g) was weighed in a glass vial and dissolved in 1 mL of Milli-Q water. In parallel, HAuCl₄ (0.0052 g) was weighed in a glass vial and dissolved in 2 mL of Milli-Q water. After boiling 48 mL of Milli-Q water in a round-bottom flask under agitation (at least 900 rpm), the trisodium citrate solution was added and, after 20 seconds, 1 mL of gold solution was added.

Close the flask with a cap and let it heat up for 15 minutes increasing the agitation up to 1000 rpm. Stop heating and cool down under agitation (1000 rpm) for 20-30 minutes. Put the mixture in a 50 mL falcon and cover it with aluminium film.

3.3.2.2 AuNPs functionalization with PEG-SH and nanobodies

Regarding the functionalization of the gold nanoparticle formulation, different gold nanoparticle-to-nanobody ratios were evaluated. Specifically, the anti-EGFR nanobodies (1.7 mg/mL) were employed and first reduced following the same procedure previously applied for the functionalization of the polymeric nanoparticles.

Once reduced, the anti-EGFR nanobodies were added to six separate vials, each containing 1 mL of the gold nanoparticle formulation, and kept under stirring. Decreasing nanobody-to-nanoparticle ratios were assessed (1:10, 1:5, 1:2, 1:1, 1:0.5, 1:0.25), while not only maintaining constant agitation of the suspension but also monitoring that the solution preserved its characteristic pinkish-red colour. In particular, the corresponding volumes of reduced nanobodies added for each ratio were: $32.4~\mu$ L, $16.2~\mu$ L, $6.5~\mu$ L, $3.2~\mu$ L, $1.6~\mu$ L, and $0.8~\mu$ L. To further ensure the stability of the formulation, PEG-SH 5k (55 μ L, $12~\mu$ M) was subsequently added to each vial.

To verify the correct size and confirm that the surface charge was preserved, the resulting nano formulation was characterized by Dynamic Light Scattering (DLS) and Nanoparticle Tracking Analysis (NTA).

3.3.3 Physicochemical characterization

3.3.3.1 Nuclear Magnetic Resonance (NMR) for Chemical Structure Verification

The chemical structure of the synthesized pBAE polymers and their functionalized derivatives was verified by 1 H and 13 C Nuclear Magnetic Resonance (NMR). For the verification of specific synthetic steps, additional 2D NMR analyses (HSQC and HMBC) were performed to provide a more in-depth confirmation of the reactions that had taken place. Spectra were recorded using a Bruker Avance 400 MHz NMR spectrometer. Samples were dissolved in either deuterated chloroform (CDCl₃) or deuterated dimethyl sulfoxide (DMSO-d₆), depending on their solubility. Chemical shifts (δ) are reported in parts per million (ppm), and spectra were processed and analyzed using MestReNova software.

3.3.3.2 Dynamic Light Scattering (DLS) for Size Distribution and Zeta Potential

The hydrodynamic diameter, polydispersity index (PDI), and zeta potential of both pBAE and gold nanoparticles, before and after functionalization, were measured using a Malvern Zetasizer Nano ZS. Measurements were carried out at 25 °C, and each sample was loaded into a standard disposable plastic cuvette prior to analysis. All measurements were performed in triplicate, and results are reported as mean values \pm standard deviation.

3.3.3.3 Nanoparticle Tracking Analysis (NTA) for Size and Concentration

The hydrodynamic diameter, size distribution, and particle concentration of both pBAE and gold nanoparticles were further evaluated using Nanoparticle Tracking Analysis (NTA, Malvern NanoSight). Samples were prepared by diluting the nanoparticle suspensions 1:100 in Milli-Q water and introduced into the instrument using a 1 mL syringe. Measurements were performed in triplicate, and the resulting data were compared with those obtained by DLS to strengthen the reliability of the results.

3.3.3.4 UV-Vis Spectroscopy for Optical Properties

To evaluate the optical properties and stability of the different gold nanoparticle formulations, both functionalized and non-functionalized with nanobodies and PEG, UV–Vis absorption analyses were performed using a Tecan Infinite 200 Pro microplate reader. Spectra were recorded over the wavelength range of 400-700 nm with a step size of 1 nm. Measurements were carried out in Greiner 96-well flat-bottom transparent polystyrene plates, with 100 μ L of each formulation loaded per well. The characteristic surface plasmon resonance (SPR) band of gold nanoparticles was checked to assess nanoparticle stability before and after functionalization, and to determine which ratio most closely resembled the optical properties of the pristine, non-functionalized formulation.

3.3.3.5 Agarose Gel Electrophoresis for Nucleic Acid Complexation

An agarose solution (1.5% (w/v)) in 65 mL of 1× TAE buffer was prepared and microwaved for 30 seconds. Then, 1 μ L of GelRed was incorporated as a fluorescent nucleic acid dye, and the gel was allowed to solidify in the casting frame for 30 minutes.

To evaluate whether pGFP was efficiently complexed by the polymeric nanoparticles, formulations were prepared using both C6-H and C32-H polymers at increasing polymer-to-genetic material ratios (1:25, 1:50, 1:75, and 1:100). These conditions were chosen to systematically assess the effect of polymer proportion on nucleic acid complexation and stability.

Samples were then loaded into the wells of the agarose gel in the following order: substrate control, 5 μ L of free pGFP, followed by the different nanoparticle formulations prepared at the indicated ratios. Electrophoresis was carried out at 100 V for 30 minutes, and genetic material migration was visualized under UV illumination to confirm the extent of nanoparticle complexation with the genetic cargo.

3.3.4 In Vitro studies

3.3.4.1 Cell Viability

The MTT assay was performed to evaluate cell viability following exposure to the different nanoparticle formulations.

A stock solution of MTT (5 mg/mL) was firstly prepared as a result of 75 mg of MTT powder dissolved in 15 mL of PBS. Before being used, the solution was diluted with a dilution factor of 1:10 in DMEM with +FBS to obtain the working solution.

After 24 h and 48 h incubation with the treatments, the medium in each well was aspirated, and the cells were washed with 100 μ L of PBS per well. Subsequently, 100 μ L of the diluted MTT solution were added to each well, and the plates were incubated for 1 h at 37 °C. Following incubation, the MTT solution was carefully aspirated avoiding touching the crystals and a 100 μ L of DMSO were added to each well to solubilize the crystals.

Absorbance was measured at 565 nm using a Tecan Infinite 200 Pro microplate reader. The results were evaluated by normalizing the absorbance values of treated wells to those of the negative control and expressed as relative cell viability (%).

3.3.4.2 Cell transfection

For in vitro studies, the breast cancer cell line MDA-MB-231 was selected among the four cell lines as the main model system. Each treatment was performed in triplicates. After 24 h from seeding, the culture medium was removed and replaced with 100 μ L of each treatment solution. The first three wells of each plate were instead treated with fresh culture medium alone, serving as negative controls.

The following treatments were tested:

- Lipofectamine particles encapsulating pGFP (positive control),
- Standard RH nanoparticles,
- C6-H nanoparticles (polymer-to-genetic material ratio 1:50),
- C32-H nanoparticles (polymer-to-genetic material ratio 1:25, standard condition),
- C6-H-nanobody nanoparticles (polymer-to-genetic material ratio 1:50),
- C32-H-nanobody nanoparticles (polymer-to-genetic material ratio 1:25, standard condition),
- Non-coated gold nanoparticles (AuNPs),
- Gold nanoparticles functionalized with anti-EGFR nanobodies at different nanobodyto-nanoparticle ratios.

All nanoparticle formulations were tested in triplicates. The transfection was only tested in polymeric nanoparticles, as a positive control lipofectamine encapsulating pGFP was used. Gold nanoparticle formulations were not included in the transfection assay since they did not encapsulate any genetic material.

Lipofectamine Nanoparticles preparation

Lipofectamine nanoparticles were prepared under a biosafety cabinet at once before use, to serve as the positive control in cell transfection experiments.

For the treatment of nine wells, two distinct solutions were prepared:

- Solution A: 2.1 μ L of pGFP were mixed with 72.9 μ L of DMEM without FBS.
- Solution B: 4.2 μ L of Lipofectamine were added to 70.2 μ L of DMEM without FBS.

Solution A was then added to Solution B, and the mixture was incubated at room temperature for 10 minutes to allow the complexation between the two solutions. After incubation, the resulting formulation was diluted in 900 μ L of complete DMEM (+FBS) in order to be ready to use.

3.3.4.3 Flow Cytometry

To assess the transfection potency of the different nanoparticle formulations encapsulating pGFP, a flow cytometry protocol was performed.

After 48 h of incubation with the formulations, the culture medium was aspirated from each well, and the cells were washed with 100 μ L of PBS. Subsequently, 25 μ L of trypsin were added to each well and incubated for 5 minutes to promote cell detachment. Then, 50 μ L of DMEM supplemented with FBS were added to neutralize the trypsin, followed by the addition of 25 μ L of paraformaldehyde (PFA) for cell fixation.

The plate was then analyzed using the flow cytometer, and the percentage of GFP-positive cells was quantified as a measure of transfection efficiency.

3.3.4.4 Western blot

Prior to Western blot analysis, protein concentrations from the four selected cell lines (MDA-MB-231, BT549, A375, and SKmel28) were determined using the bicinchoninic acid (BCA) assay. A standard curve was prepared using serial dilutions of bovine serum albumin (BSA) ranging from 0 to 2000 μ g/mL, and absorbance was measured at 562 nm with a Tecan Infinite 200 Pro microplate reader. Based on the standard curve, the protein content of each sample was determined: MDA \approx 1176 μ g/mL, BT549 \approx 298 μ g/mL, A375 \approx 1915 μ g/mL, and SKmel28 \approx 1922 μ g/mL.

Western blotting was performed to evaluate EGFR expression across the four selected cell lines. Thus, 18 μ g of total protein from each sample were used. Volumes were

adjusted with Milli-Q water to reach 20 μ L, and 5 μ L of bromophenol blue (0.04%) were added before denaturation at 95 °C for 10 minutes.

Proteins were separated using SDS–PAGE by using a 12% polyacrylamide gel and subsequently transferred onto a polyvinylidene difluoride (PVDF) membrane. The membrane was then blocked in 5% (w/v) non-fat dry milk prepared in TBST buffer to minimize non-specific antibody binding.

For immunodetection, the membrane was incubated with a primary anti-EGFR antibody (dilution 1:500 in blocking buffer), followed by incubation with a secondary antibody (dilution 1:2000 in blocking buffer).

Finally, protein bands were visualized using the AmershamTM ImageQuantTM 800 biomolecular imager (Cytiva Life Sciences, USA).

4 Results and Discussion

4.1 pBAE Nanoparticles: synthesis and characterization

In this section, the synthetic steps and characterization of the ¹H NMR related to the pBAE polymers will be analysed and further explained.

For each step during the chemical reactions, the ¹H NMR spectra was analysed, which served as a guide to demonstrate and verify the correct formation of the polymer during the different reactions and its functionalization. These spectra show signals corresponding to protons present in the chains of the analysed compounds which, depending on their chemical environment and how many other protons are within their range, show a certain shift that is quantified in parts per million (ppm). On the ordinates of each spectrum, the intensity quantifies the abundance of the functional group to which a certain proton belongs [47].

During the functionalization of the polymers with the maleimide structure using an esterification reaction (Steglich esterification) between the side chains of the two polymers and maleimide [48], more in-depth analyses were carried out through the study of ¹³C NMR, HMBC NMR and HSQC NMR spectra. It was done not only to confirm the presence of the polymer and the maleimide bound together, but also to verify the correct position and reaction between them. In particular, ¹³C NMR is an additional 1D analysis that shows the carbons corresponding to a certain chemical environment. Then 2D analyses were performed, including the HMBC NMR and HSQC NMR spectra. In the HMBC NMR spectrum, a correlation is made between protons in a certain chemical environment and the carbons corresponding to 2-3 bonds away, while in the HSQC NMR the protons are correlated with the carbons one bond away [49].

The different analyses will proceed with the identification of the characteristic peaks for each reaction, followed by an explanation that will serve as the starting point for each subsequent step.

The starting reagents for the synthesis of C6 and C32 polymers were verified by 1H NMR in order to confirm their suitability for the Michael addition reaction.

5-amino-1-pentanol (¹H NMR, DMSO-d₆)

- δ 3.4 ppm (t, 2H) CH₂ adjacent to OH \rightarrow primary alcohol
- + δ 2.5 ppm (t, 2H) CH₂ adjacent to NH₂ \rightarrow primary amine
- δ 1.2–1.6 ppm (m, 6H) central methylenes \rightarrow aliphatic chain

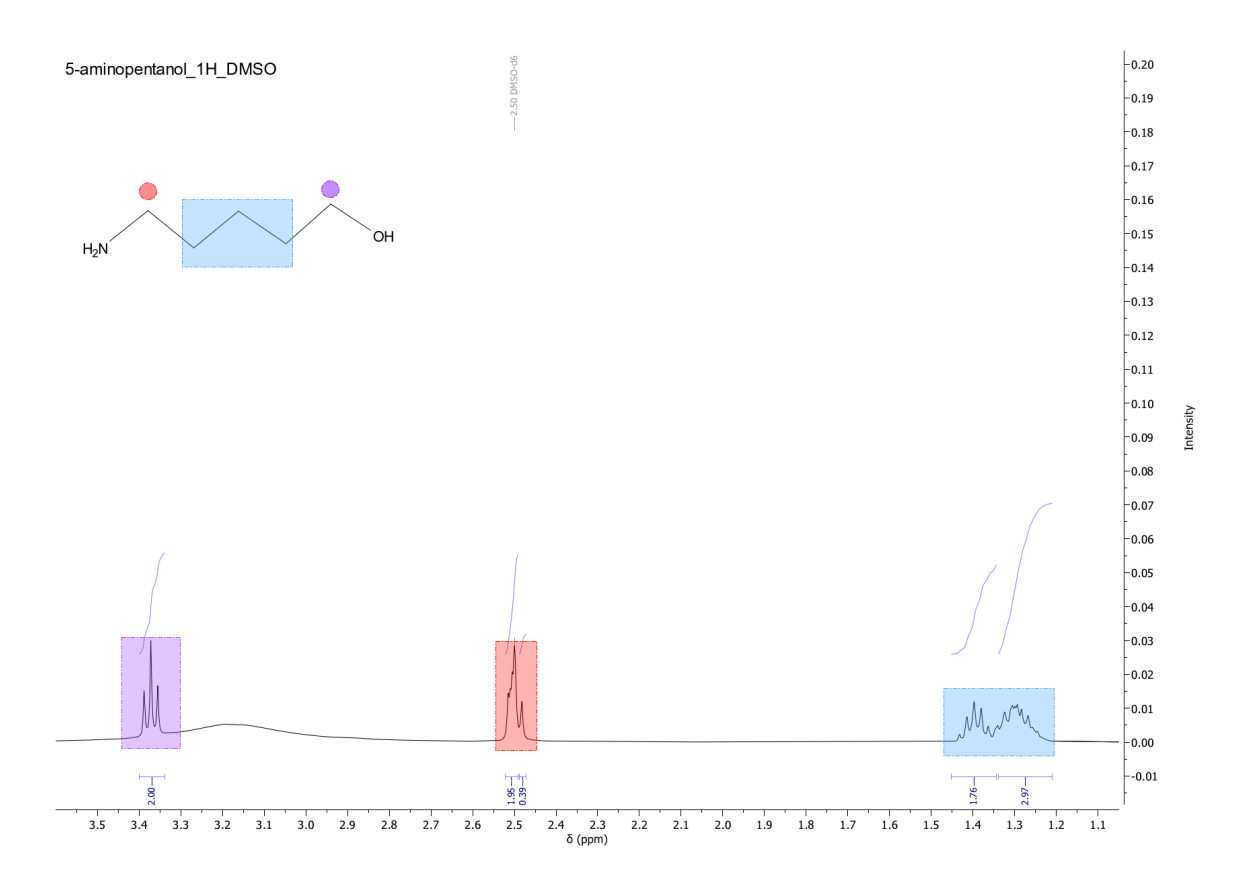


Figure 7: 5-amino-1-pentanol ($^1\mathrm{H}$ NMR, DMSO-d $_6$)

1,4-butanediol diacrylate (¹H NMR, DMSO-d₆)

- δ 5.5–5.0 ppm (m, 4H) vinyl protons (CH=CH₂) \rightarrow acrylate group
- 3.5–3.0 ppm (t, 4H) O-CH₂ adjacent to ester carbonyl \rightarrow ester group
- δ 1.0–0.5 ppm (m, 4H) central $\mathrm{CH_2} \to \mathrm{butylene}$ backbone

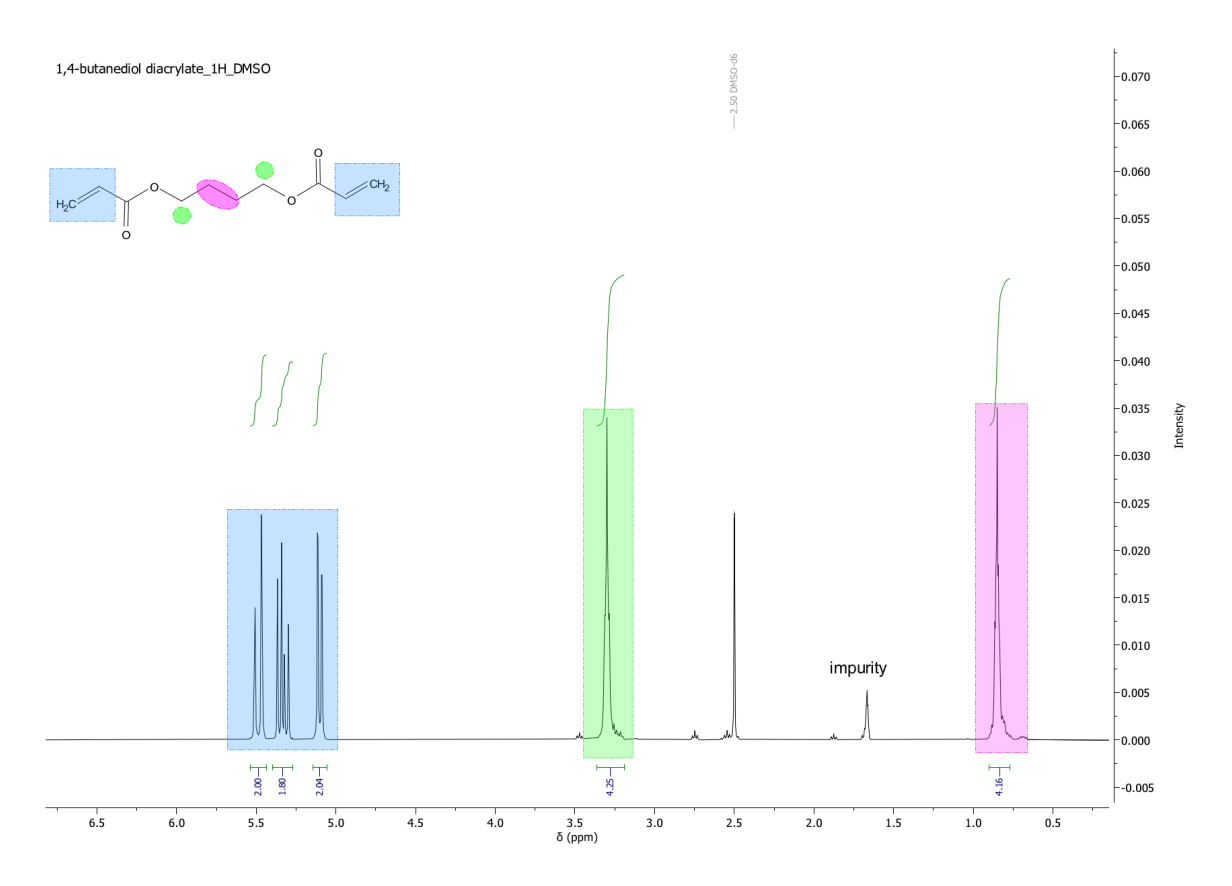


Figure 8: 1,4-butanediol diacrylate ($^1\mathrm{H}$ NMR, DMSO-d₆)

1-hexylamine (¹H NMR, DMSO-d₆)

- δ 2.6 ppm (t, 2H) CH₂ adjacent to NH₂ \rightarrow primary amine
- δ 1.2–1.6 ppm (m, 8H) methylenes \rightarrow aliphatic chain
- δ 0.9 ppm (t, 3H) terminal $\mathrm{CH_3} \to \mathrm{alkyl}$ chain end

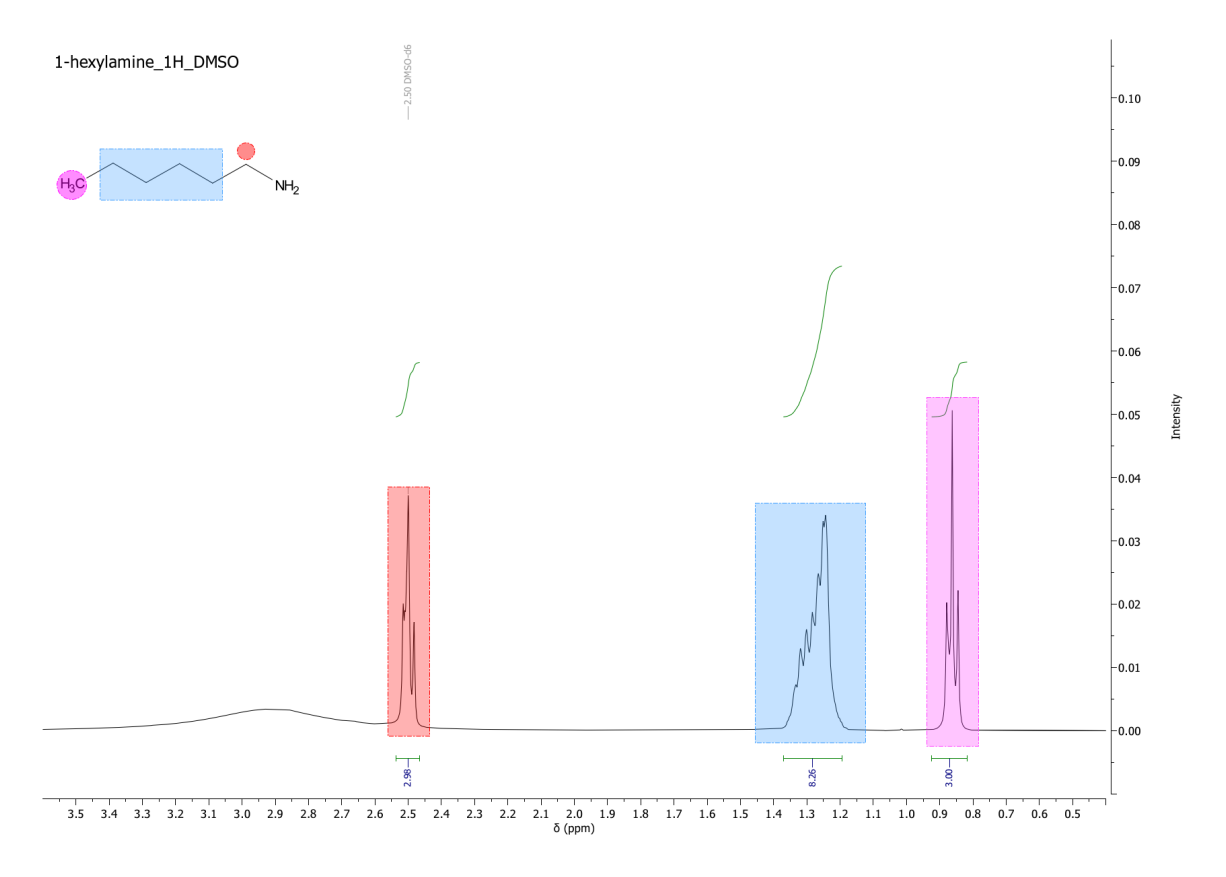


Figure 9: 1-hexylamine (¹H NMR, DMSO-d₆)

In Figure 7, Figure 8 and Figure 9, the three compounds presented their characteristic peaks, which verified their purity for further use in the next steps.

4.1.1 Synthesis and characterization of C6 and C32 by $^1\mathrm{H}$ NMR

First, it was important to assess the results from the three initial reactants in order to be aware of the subsequent outcomes from several reactions and to precisely identify the different peaks along the spectra.

¹H-NMR of C6 polymer after Michael addition

Figure 10: C6 polymer molecular structure

In Figure 11 the ¹H NMR spectrum of C6 (Figure 10) shows the characteristic signals that confirm the Michael addition reaction between 5-amino-1-pentanol, 1-hexylamine, and 1,4-butanediol diacrylate. The analysis reveals that, within the 6.5–5.5 ppm range, the vinyl double bonds of 1,4-butanediol diacrylate are present, which underwent a slight shift upon reaction. In the 4.3–4.1 ppm range, signals are attributed to the methylene protons adjacent to the ester oxygen atoms (–O–CH₂–), while in the 3.6–3.4 ppm range, signals correspond to the methylene groups adjacent to the terminal hydroxyl (–CH₂–OH). In the 2.7–2.4 ppm range, signals correspond to the methylene protons adjacent to the amine group (–CH₂–NH–). Finally, the 1.9–1.2 ppm region corresponds to the aliphatic backbone of the polymer, confirming its structural integrity, while the 1.0–0.9 ppm region shows the characteristic triplet of the terminal methyl group (–CH₃) of the hexyl chain that distinguishes C6 polymer from C32 polymer.

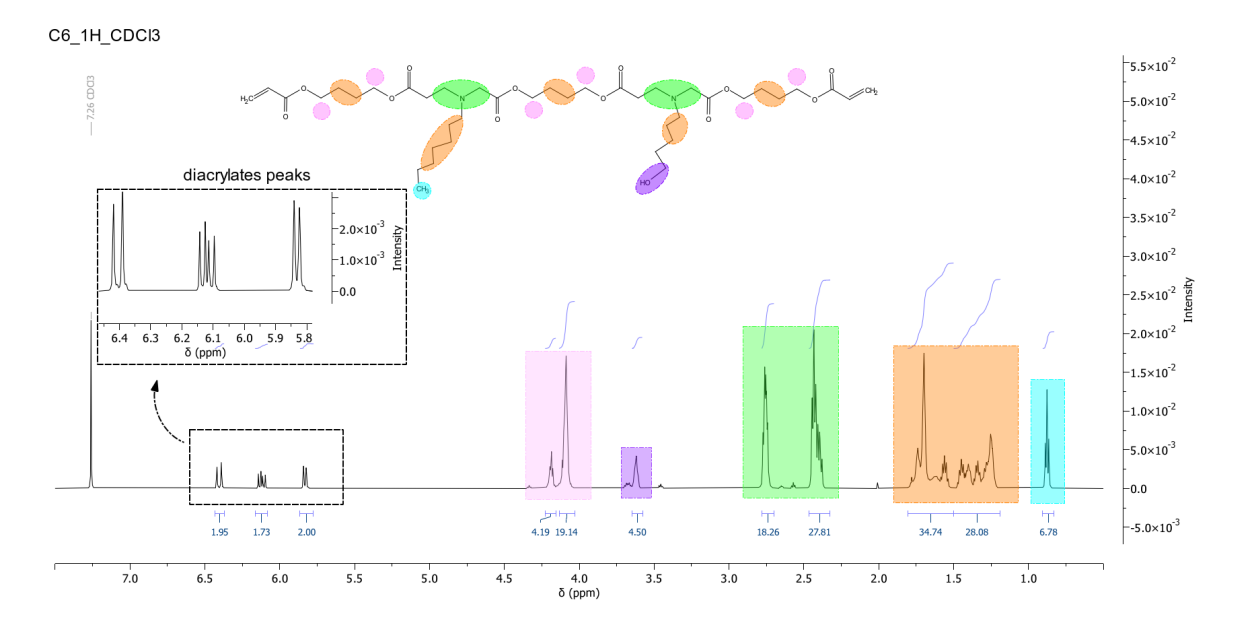


Figure 11: $^1\mathrm{H}$ NMR spectrum of C6 polymer; solvent used: DMSO

¹H-NMR of C32 polymer after Michael addition

Figure 12: C32 polymer molecular structure

In Figure 13, the ¹H NMR spectrum of polymer C32 (Figure 12) displays the character-

istic signals resulting from the Michael addition reaction between 5-amino-1-pentanol and 1,4-butanediol diacrylate. In the region between 6.5–5.5 ppm, as observed for C6, signals corresponding to the vinyl double bonds are detected, showing a slight shift due to the reaction process. In the 4.3–4.0 ppm region, the protons of the methylene groups adjacent to the ester oxygens ($-O-CH_2-$) are observed. Of particular importance, as highlighted in the previous spectrum, is the confirmation of the signal corresponding to the methylene groups adjacent to the terminal hydroxyl group ($-CH_2-OH$). In the 2.7–2.4 ppm region, the signals of the methylene protons adjacent to the amine groups ($-CH_2-NH-$) are present, while the main aliphatic backbone of the polymer is confirmed by the signals in the 1.9–1.3 ppm region. Finally, around 1.0 ppm, no terminal methyl ($-CH_3$) signal from hexyl chains is detected, confirming the difference between the monomers used for the synthesis of the two polymers.

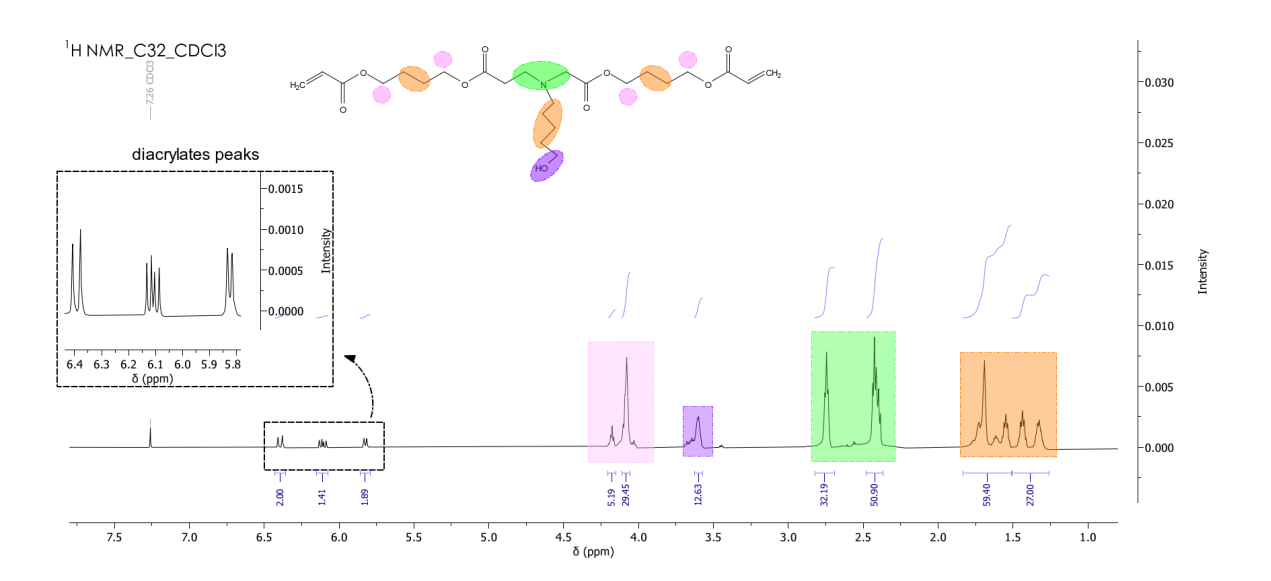


Figure 13: ¹H NMR spectrum of C32 polymer; solvent used: DMSO

From these results the expected outcomes from next reactions' spectra are about maintaining the integrity of the main backbone for both polymers. In particular, the peaks in 2.7-1.0 pp, range should remain slightly the same (variations can occur due to chemical shifts during reactions). Indeed, the presence of peaks in that range will confirm the structure integrity.

4.1.2 Verification of maleimide protection by ¹H NMR spectrum analysis

As the maleimide (Figure 14) can react with the free acrylates of the polymers, we had to protect the maleimide by using furan and avoid secondary reactions [50]. If left unprotected, this reactivity would compromise its primary function, which is to serve as a specific reactive site for nanobody conjugation via click chemistry once the nanoparticle is formed. This subsection is dedicated to the analysis of the ¹H NMR spectra of maleimide-COOH before and after furan protection.

Figure 14: maleimide-COOH molecular structure

In Figure 15, the 1 H NMR spectrum of the unprotected maleimide-COOH is reported. A characteristic singlet at \sim 6.7 ppm corresponds to the vinyl protons of the maleimide double bond (-CH=CH-), confirming the presence of the unsaturated maleimidic ring. At 4.2 ppm, a triplet is observed, corresponding to the methylene protons adjacent to the oxygen atom of the lateral carboxyl group (-O-CH₂-). Finally, at 2.3 ppm, a signal is assigned to the methylene protons adjacent to the carbonyl group (-CH₂-COOH).

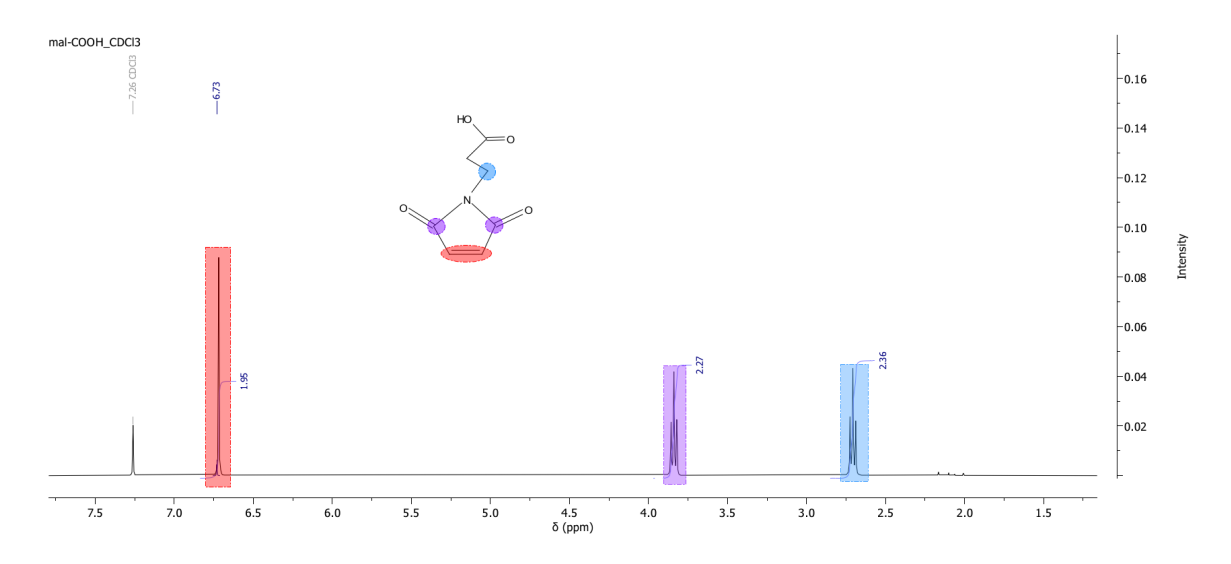


Figure 15: ¹H NMR spectrum of the unprotected maleimide-COOH; solvent used: CDCl3

This spectrum will serve as a reference for monitoring the structural modifications introduced after the protection step. As previously mentioned, maleimide is a highly electrophilic group that tends to react non-specifically with nucleophiles present in the reaction environment (e.g., acrylates, amines or thiols).

In the context of the following syntheses, this would carry the risk of undesired reactions with free acrylates, thereby preventing the correct subsequent functionalization [51].

Furan was selected as a protecting group since it acts as a diene in a Diels-Alder cycloaddition with the electron-deficient double bond of the maleimide (Figure 16). The main advantage of this approach lies in its reversibility: deprotection occurs cleanly at moderate temperatures, without generating undesired reaction products.

Figure 16: maleimide protection reaction via Diels-Alder cycloaddition;

In Figure 17, the ¹H NMR spectrum of the furan-protected maleimide is shown. A signal at ~6.5 ppm corresponds to the characteristic protons of the furan double bond, while the resonance at ~5.0 ppm is assigned to the bridgehead proton of the Diels–Alder adduct. This latter signal is of particular importance, as it not only confirms the successful cycloaddition but also serves as a reference for the subsequent deprotection step, where its disappearance indicates the regeneration of the free maleimide [52]. Finally, in the region 3.6–3.5 ppm the methylene protons adjacent to the lateral carboxyl group are observed, while the signals at 2.6–2.45 ppm correspond to the methylene protons next to the carbonyl group.

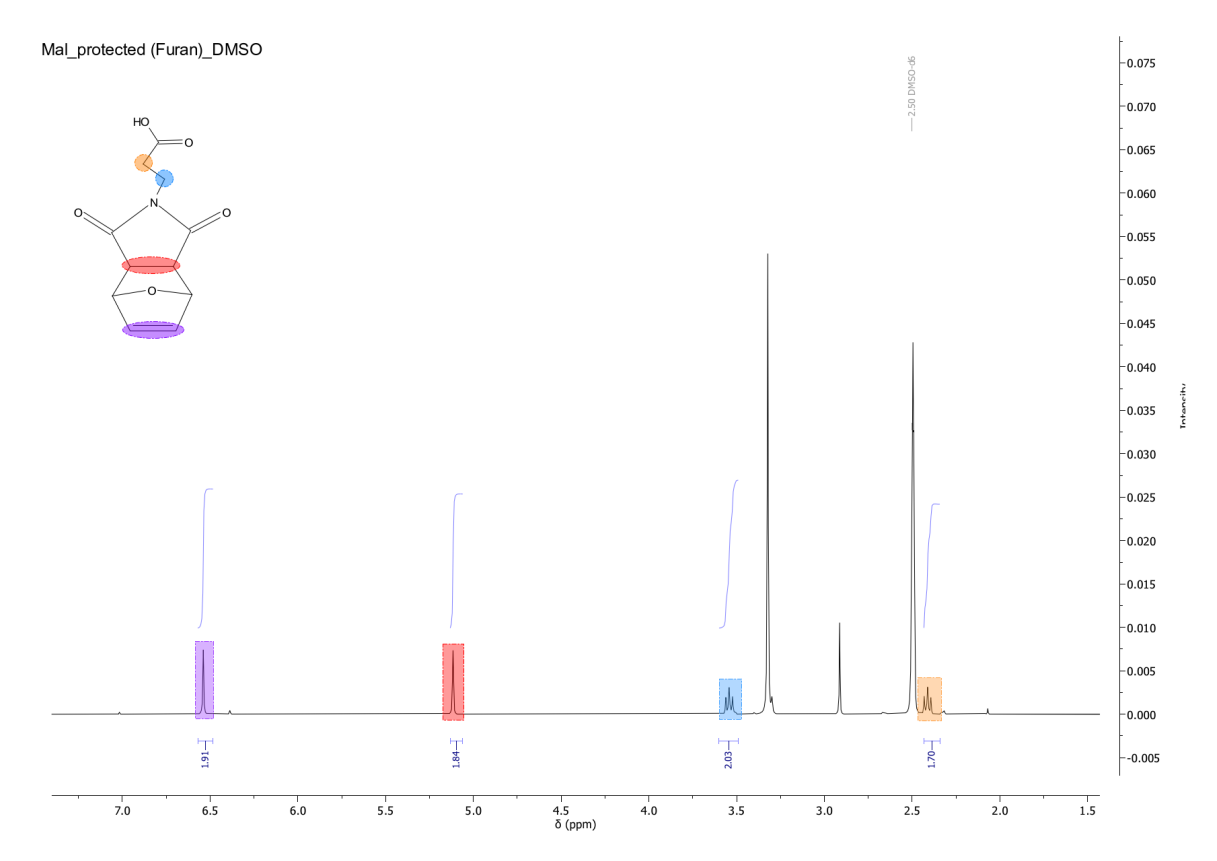


Figure 17: ¹H NMR spectrum of the furan-protected maleimide; solvent used: DMSO

4.1.3 Ester formation by maleimide attachment and characterization by ¹H, ¹³C, HSQC, and HMBC NMR

In this subsection, the ¹H, ¹³C, HSQC, and HMBC NMR spectra related to the conjugation of maleimide to the lateral hydroxyl groups of the C6 (Figure 18) and C32 (Figure 19) polymers will be analyzed.

The reaction was carried out via Steglich esterification, employing DCC/DMAP-mediated coupling chemistry under anhydrous conditions.

Figure 18: C6 polymer-protected maleimide complex molecular structure

Figure 19: C32 polymer-protected maleimide complex molecular structure

The HSQC and HMBC spectra were specifically used to confirm and further support the successful esterification between the carboxylic group of the protected maleimide-COOH and the terminal hydroxyl groups present on the polymer side chains.

The analysis will first focus on the spectra obtained for the C6 polymer, followed by those corresponding to the C32 polymer.

¹H NMR spectra of C6-protected maleimide

In Figure 20, the ¹H NMR spectrum corresponding to the reaction between C6 and the furan-protected maleimide is reported. A signal is observed at approximately 6.6 ppm, that corresponds to the vinyl protons of the furan-protected maleimide ring (–CH=CH–), while at 5.0 ppm the characteristic resonance of the protons of the Diels–Alder bridge is detected. These two signals provide an initial confirmation of the successful introduction of the protected maleimide.

Further evidence is given by the signal at 4.1 ppm, assigned to the methylene protons adjacent to the ester oxygen ($-O-CH_2-O-$), which confirms the formation of a new ester bond. This assignment is additionally supported by the disappearance of the 3.6 ppm resonance, originally associated with the methylene protons next to the terminal hydroxyl group.

The remaining signals of the spectrum, observed at 2.8–2.4 ppm, 2.3 ppm, 1.9–1.2 ppm, and 1.0 ppm, confirm the correct preservation of the polymer backbone after the reaction.

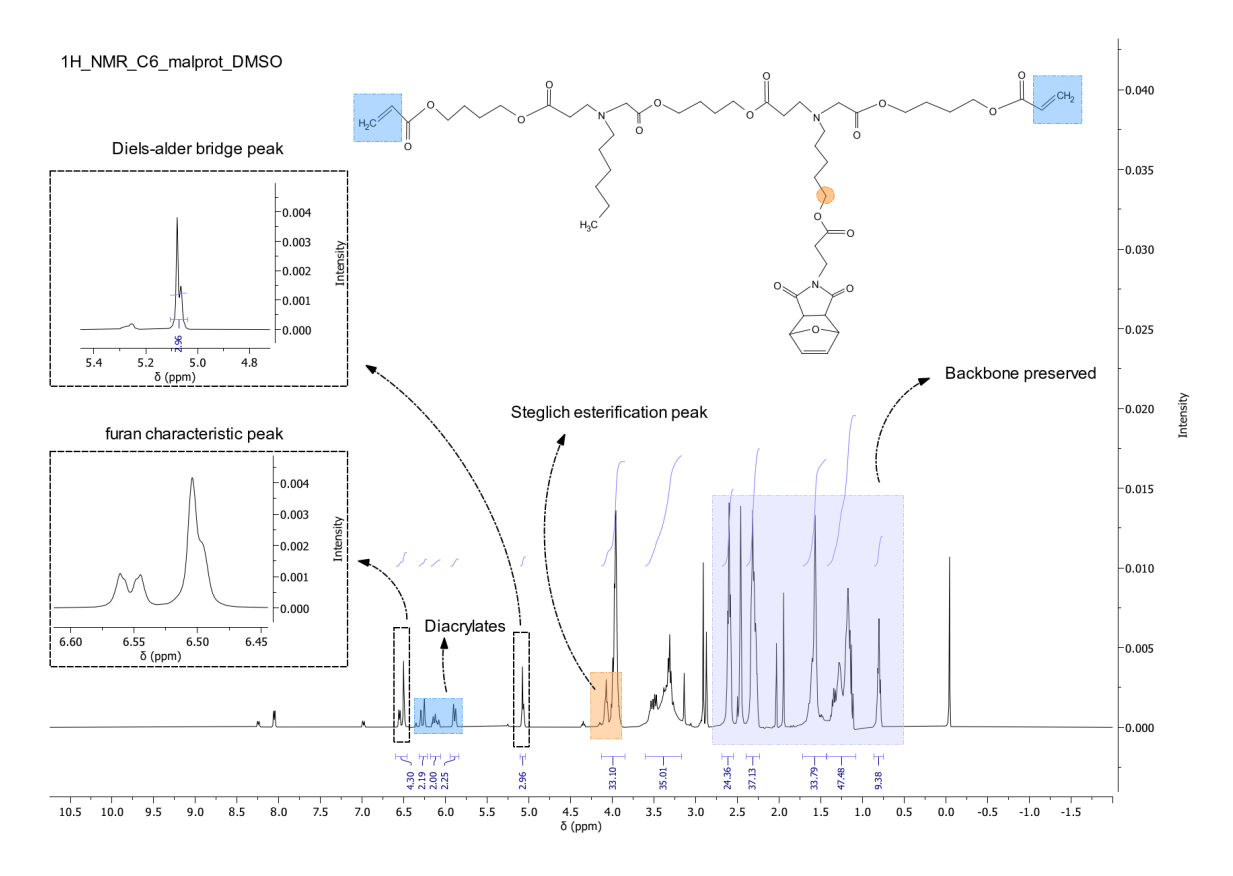


Figure 20: 1 H NMR spectrum of the reaction between C6 and the furan-protected male imide via Steglich esterification; solvent used: DMSO

¹³C NMR spectra C6-protected maleimide

In Figure 21, the ¹³C NMR spectrum is reported as confirmation of the successful esterification between C6 and the furan-protected maleimide. Specifically, the resonance observed in the region of 175–170 ppm corresponds to ester carbonyl carbons (–COO–), originating both from the polymer backbone (internal esters) and from the newly formed ester bond with the maleimide. In addition, signals in the 135–120 ppm range are attributed to the vinyl carbons of the unsaturated maleimide ring involved in the Diels–Alder reaction.

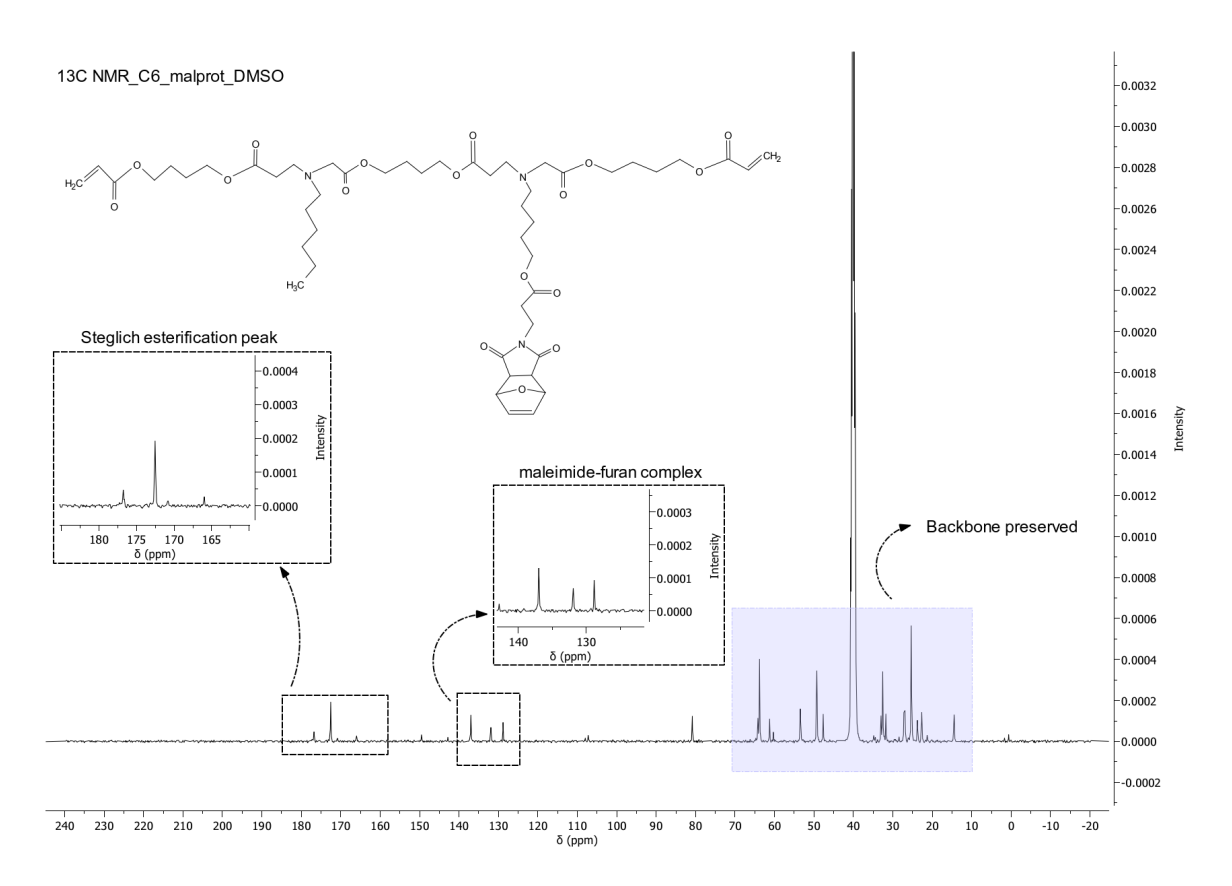


Figure 21: 13 C NMR spectrum of the reaction between C6 and the furan-protected male imide via Steglich esterification; solvent used: DMSO

HMBC NMR spectra of C6-protected maleimide

In Figure 22, the HMBC NMR spectrum of the C6-protected maleimide complex is shown between protons to 2-3 bonds away. The first key correlation is detected between the methylene protons at 4.3–4.1 ppm range and a carbonyl resonance at 173–170 ppm range; it confirms the formation of a new ester bond resulting from the reaction between the polymer and the protected maleimide. In addition, long-range correlations with sp² carbons in the 145–110 ppm range indicate that the furan–maleimide adduct remains intact after the reaction. Finally, at 3.6 ppm no signal is detected, confirming the disappearance of the methylene protons adjacent to the terminal hydroxyl group of the polymer due to the esterification reaction.

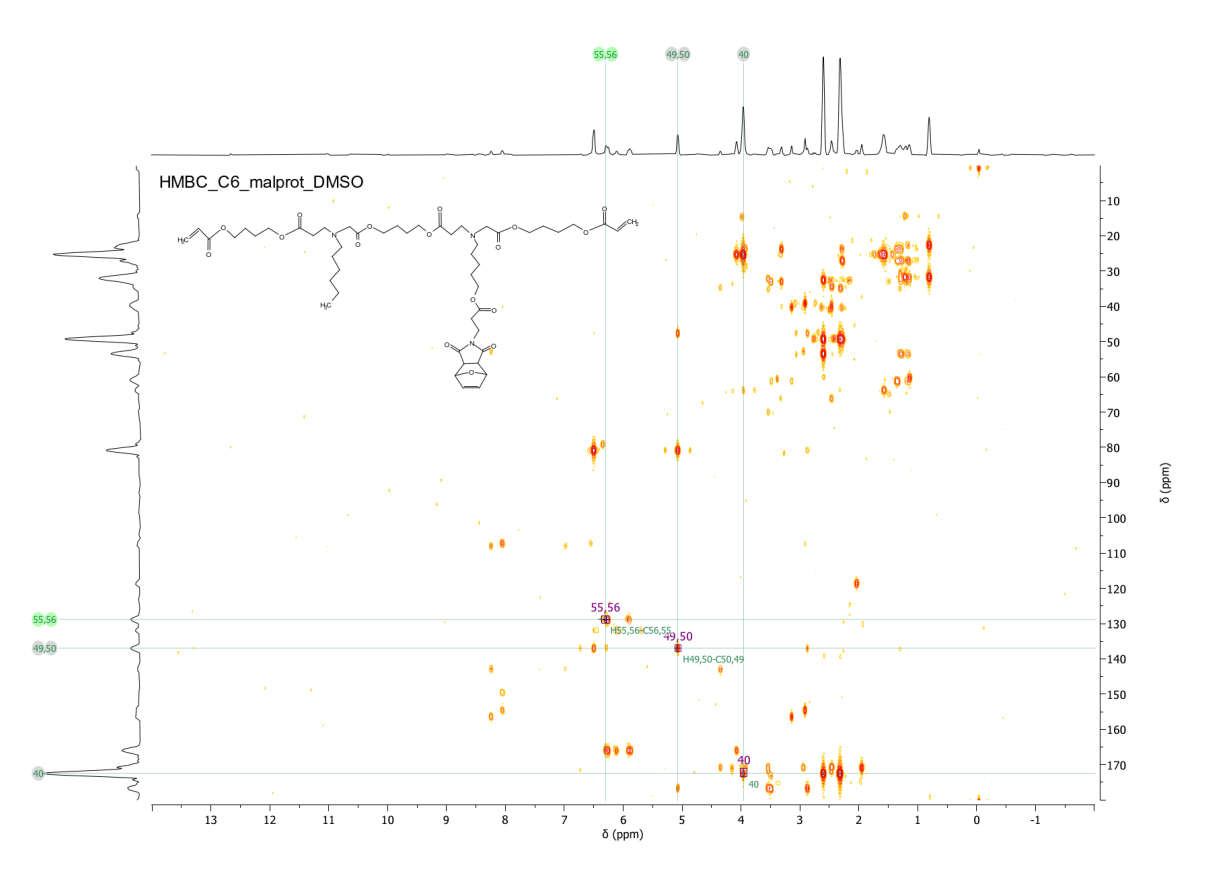


Figure 22: HMBC NMR spectrum of the C6-protected maleimide complex; solevnt used: DMSO

HQSC NMR spectra of C6-protected maleimide

Figure 23 shows the HSQC NMR spectrum of the C6-protected maleimide conjugate. The most relevant cross-peak is observed between the proton signal at 4.0 ppm and the carbon resonance at approximately 60 ppm. This correlation corresponds to the methylene protons adjacent to the newly formed ester bond. Another cross-peak is observed between the signal at 66 ppm and the region 140–120 ppm, which corresponds to the vinyl carbons of the furan–maleimide adduct, confirming their preservation. These two significant signals provide strong evidence for the successful attachment of the protected maleimide to the C6 polymer.

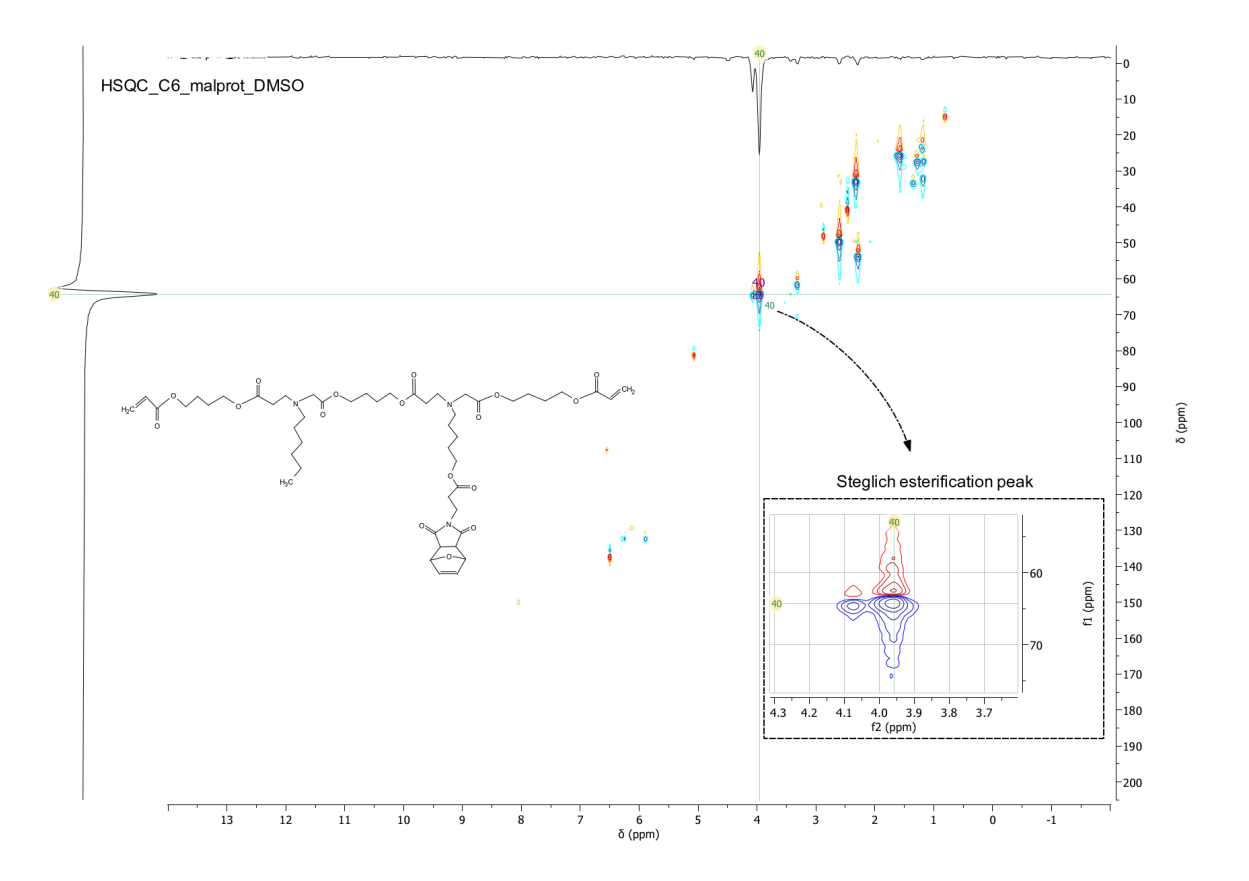


Figure 23: HSQC NMR spectrum of the C6-protected male imide complex; solvent used: DMSO $\,$

¹H NMR spectra C32-protected maleimide

In Figure 24, the ¹H NMR spectrum corresponding to the reaction between C32 and the furan-protected maleimide is shown. At around 6.6 ppm, a signal is detected that corresponds to the vinyl protons of the furan-protected maleimide ring (–CH=CH–), while at 5.0 ppm the resonance characteristic of the protons of the Diels–Alder bridge is observed. These two signals provide a solid primary confirmation of the successful incorporation of the protected maleimide. Additional validation is provided by the resonance at 4.2–4.0 ppm, attributed to the methylene protons adjacent to the ester oxygen (–O–CH₂–O–), confirming the formation of the ester group. This assignment is further strengthened by the disappearance of the signal at 3.6 ppm, originally associated with the methylene protons of the terminal hydroxyl group. The remaining peaks of the spectra, observed in the regions 2.8–2.4 ppm, 2.3 ppm, and 1.9–1.2 ppm, confirm the correct preservation of the aliphatic polymer backbone after the reaction.

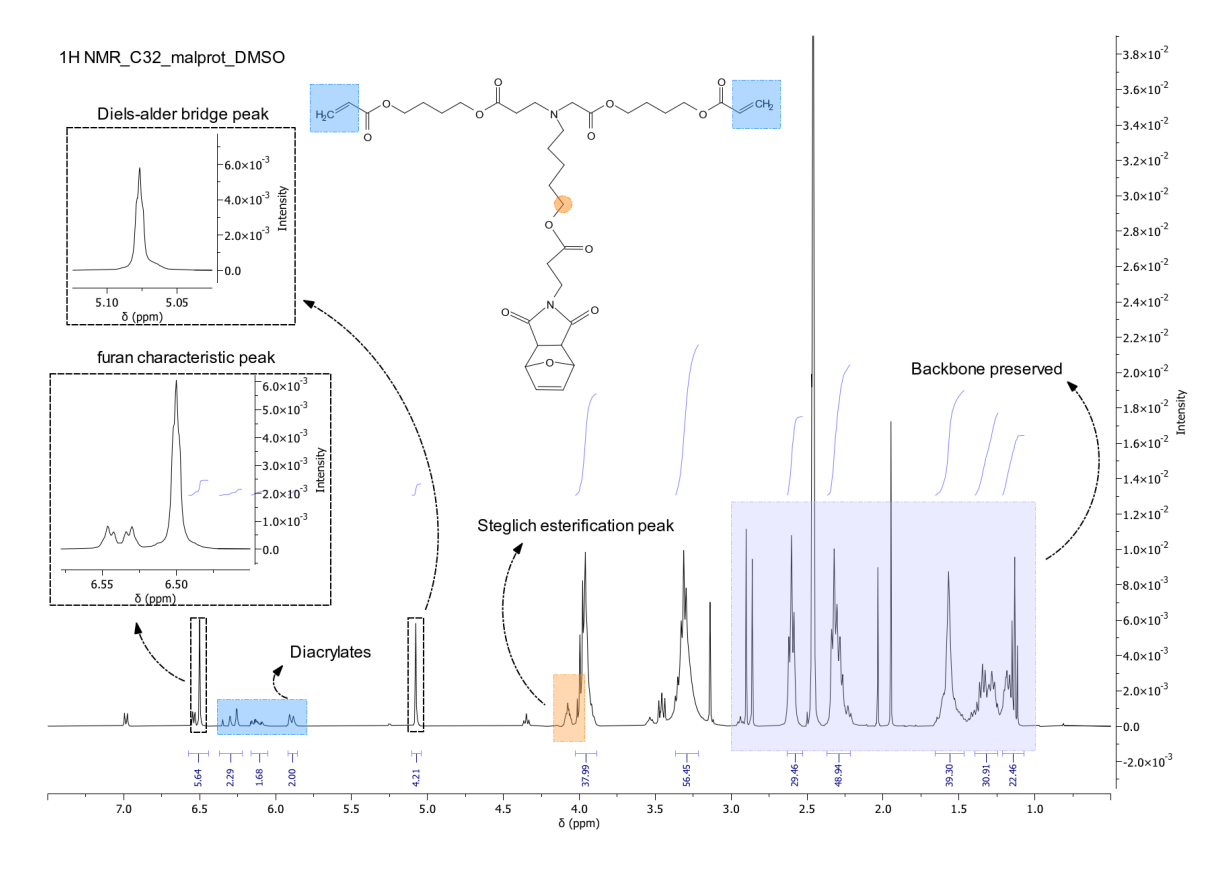


Figure 24: 1 H NMR spectrum the reaction between C32 and the furan-protected male imide via Steglich esterification; solvent used: DMSO

¹³C NMR spectra C32-protected maleimide

In Figure 25, the ¹³C NMR spectrum is reported as confirmation of the successful esterification between C32 and the furan-protected maleimide. Specifically, the resonance observed in the region of 175–170 ppm corresponds to ester carbonyl carbons (–COO–), originating both from the polymer backbone (internal esters) and from the newly formed ester bond with the maleimide. In addition, signals in the 145–135 ppm range are attributed to the vinyl carbons of the unsaturated maleimide ring involved in the Diels–Alder reaction.

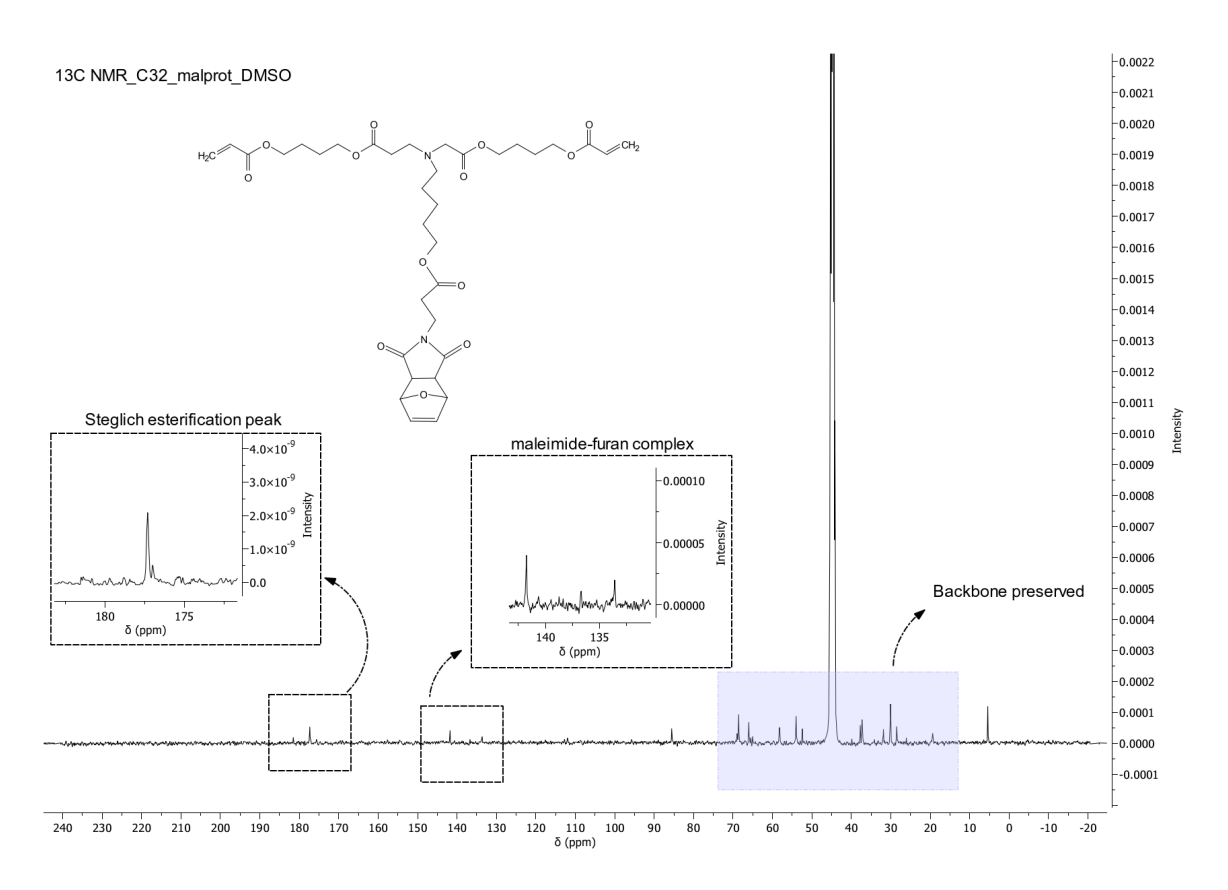
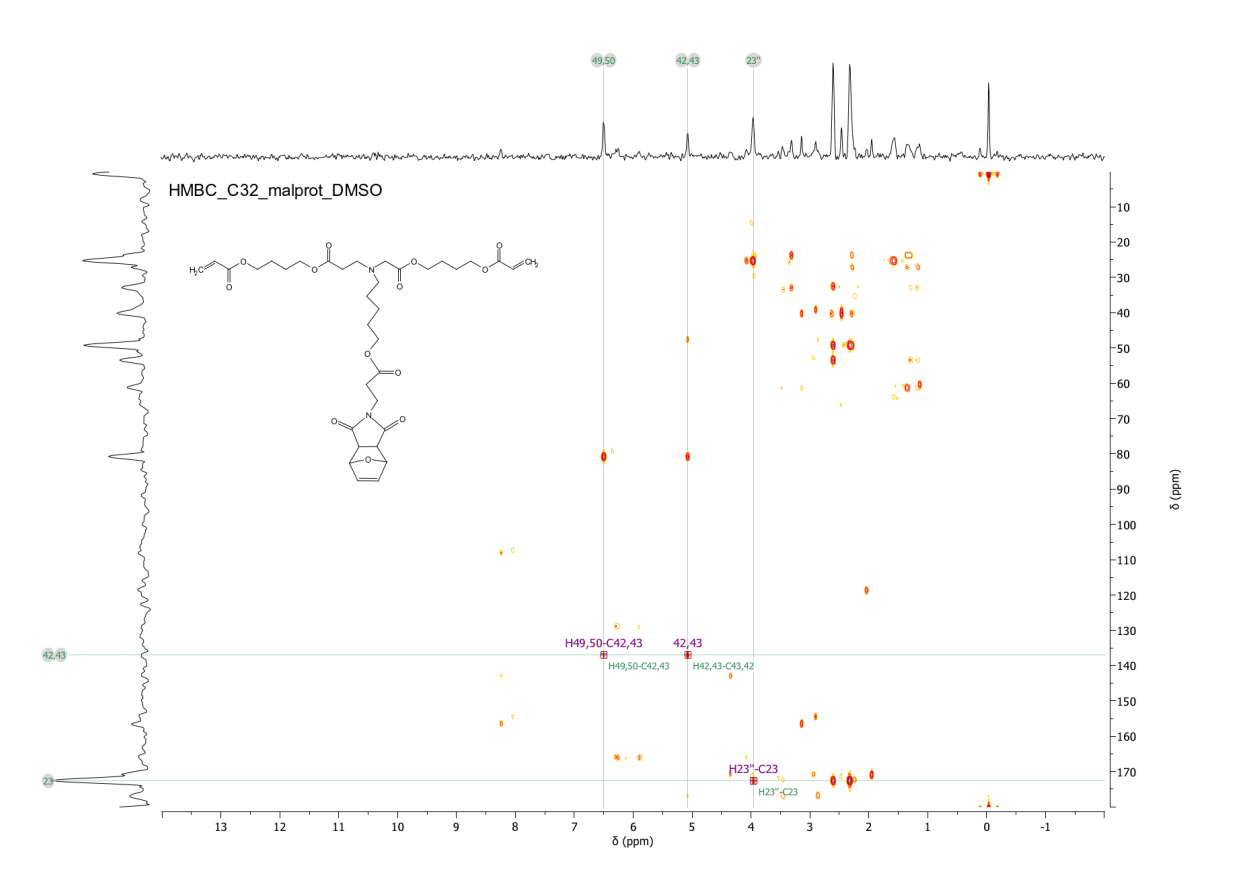


Figure 25: 13 C NMR spectrum of the reaction between C32 and the furan-protected male imide via Steglich esterification; solvent used: DMSO

HMBC NMR spectrum of C32-protected maleimide complex

In Figure 26, the HMBC NMR spectrum of the C32–protected maleimide complex is observed. The first key correlation is detected between the methylene protons at 4.0 ppm and a carbonyl resonance at 173–170 ppm range; it confirms the formation of a new ester bond resulting from the reaction between the polymer and the protected maleimide. In addition, long-range correlations with sp² carbons in the 145–110 ppm range with 5.0 ppm and 6.5 ppm regions' protons assessed that the furan–maleimide adduct remained intact after the reaction. Finally, it is noteworthy that the peak at 3.6 ppmdisappeared, confirming the esterification of the polymer.



 $Figure\ 26:\ HMBC\ NMR\ spectrum\ of\ the\ C32-protected\ male imide\ complex;\ solevnt\ used:\ DMSO$

HQSC NMR spectrum of C32-protected maleimide complex

In Figure 27 the HSQC NMR spectrum of the C6-protected maleimide conjugate is shown. The most significant cross-peak is observed between the proton signal at 4.0 ppm and the carbon resonance at approximately 60 ppm. This correlation corresponds to the methylene protons adjacent to the formed ester bond; it is the result of the esterification reaction between C32 polymer and maleimide. Another cross-peak is observed between the signal at 66 ppm and the region 140–120 ppm, which corresponds to the vinyl carbons of the furan-maleimide adduct, confirming their preservation. These two significant signals provide strong evidence for the successful attachment of the protected maleimide to the C32 polymer.

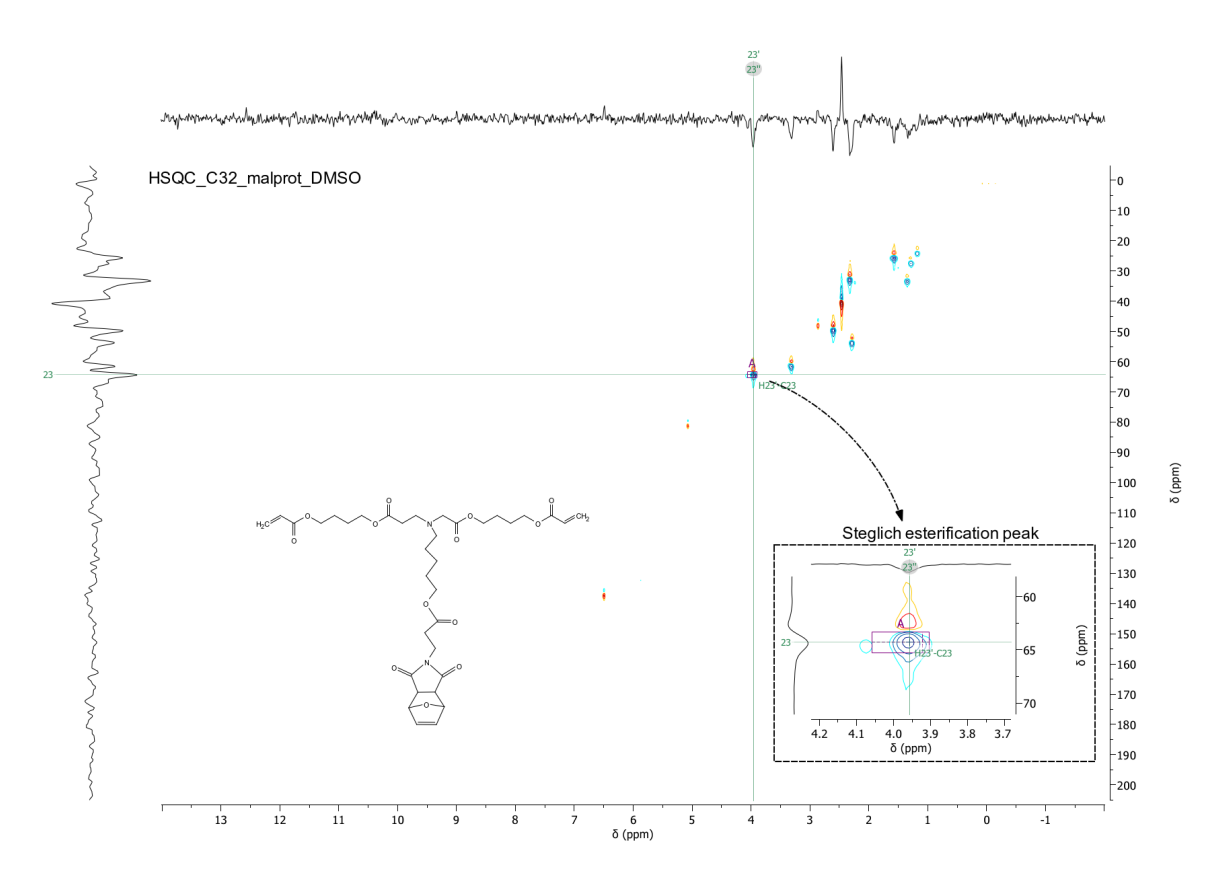


Figure 27: HSQC NMR spectrum of the C6-protected maleimide complex; solvent used: DMSO

4.1.4 Functionalization of the polymer with the arginine-ending peptide

In the following section, the results related to the two ¹H NMR spectra of the functionalization of the CRRR peptide with the two polymers C6 (Figure 28) and C32 (Figure 29) will be analyzed. Significant peaks are expected to be obtained in the range 9.0–7.0 ppm related to the presence of the peptide [53].

Figure 28: C6-protected maleimide complex functionalization with CRRR peptide

C6 - protected maleimide - CRRR peptide complex

C32 - protected maleimide complex

C32 - protected maleimide - CRRR peptide complex

Figure 29: C32-protected maleimide complex functionalization with CRRR peptide

¹H NMR spectra of C6 - protected maleimide - CRRR peptide

Figure 30 shows the result of the reaction of arginine peptide to the main C6 polymer chain. At 9.0-7.0 ppm range the presence of significant signals are detected, corresponding to the presence of arginine peptide. At 6.7 ppm the peaks associated with the terminal acrylates groups of the molecules disappeared, confirming the success of the reaction. The signal at 5.0 ppm, corresponding to the furan protection, is detected. The remaining signals are slightly similar as in the previous spectra (due to the chemical shifts caused by the reaction) and the backbone of the polymer is preserved.

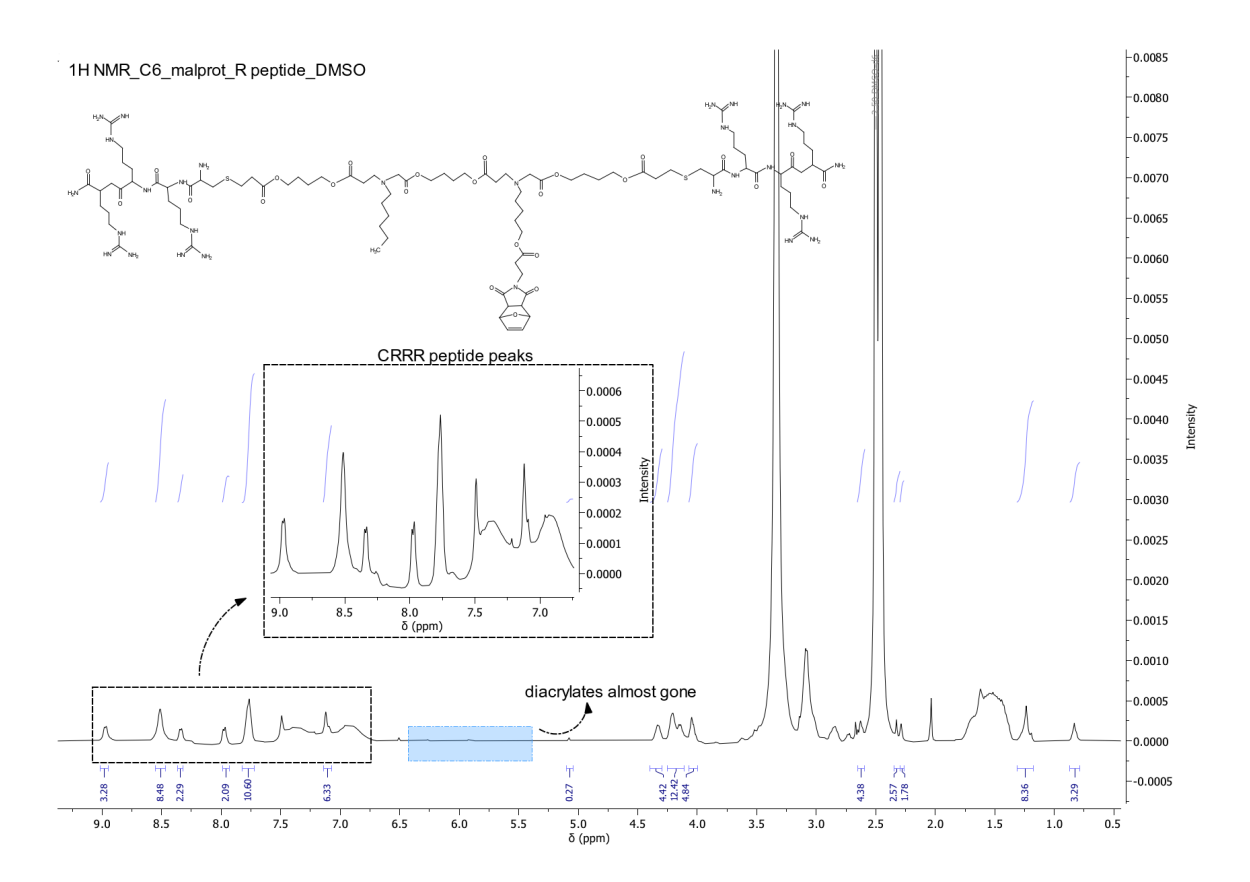


Figure 30: $^{1}\mathrm{H}$ NMR spectra of C6 - protected maleimide - CRRR peptide; solvent used: DMSO

¹H NMR spectra analysis of C32 - protected maleimide - CRRR peptide

As previously said for C6 polymer, even with C32 polymer the successful reaction with arginine peptide has been assessed and in Figure 31 the result of the reaction of arginine peptide to the main C6 polymer chain is shown. At 9.0-0-7.0 ppm range presence of significant signals are detected, corresponding to the presence of arginine peptide. At 6.7 ppm the peaks corresponding to the terminal acrylates disappeared, confirming the success of the reaction. Moreover, a signal at 5.0 ppm, corresponding to the furan protection, is detected. The remaining signals are slightly similar as in the previous spectra (due to the chemical shifts caused by the reaction) and the backbone of the polymer is preserved.

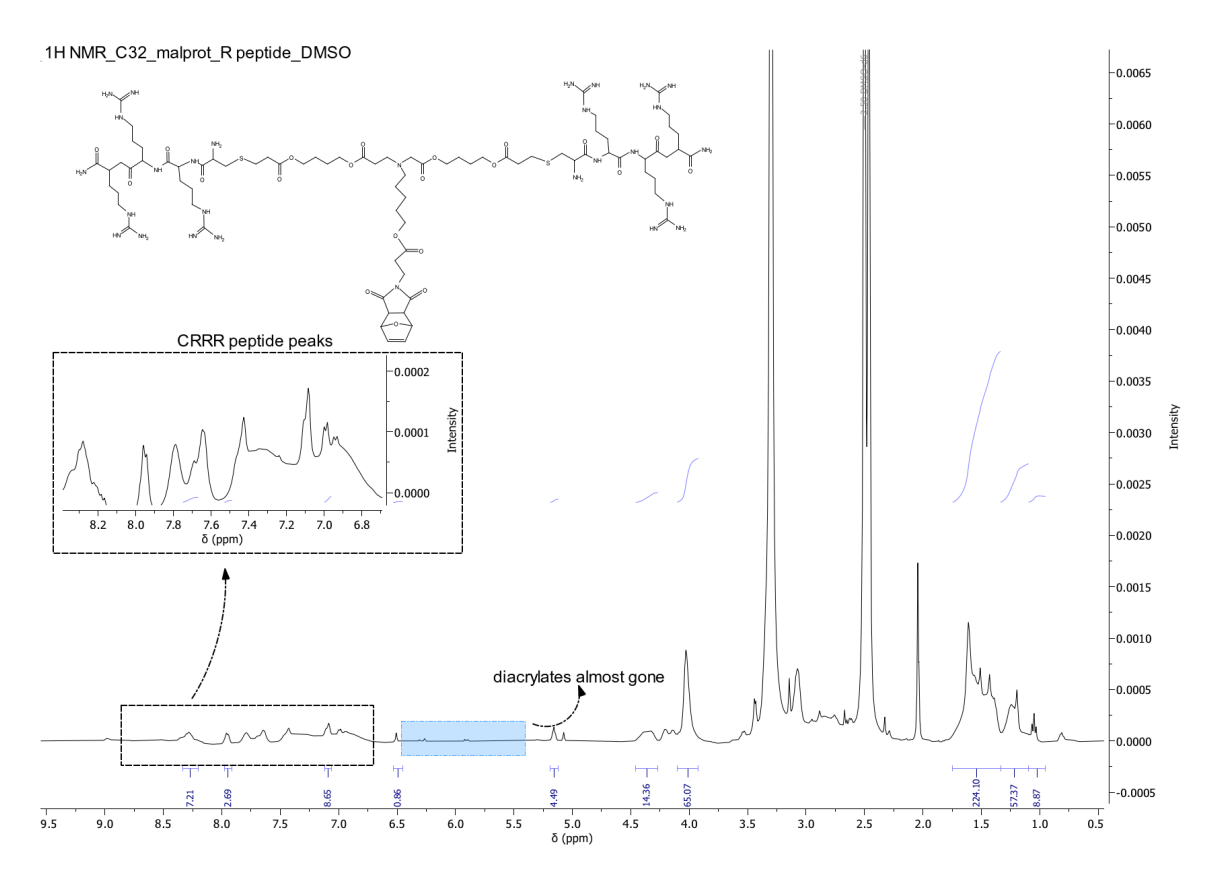


Figure 31: ¹H NMR spectra analysis of C32 - protected maleimide - CRRR peptide; solvent used: DMSO

4.1.5 Maleimide deprotection by ¹H NMR

The following section is dedicated to the assessment of the deprotection of the maleimide and the verification of the integrity of the final product (Figure 32) (Figure 33). The expected outcome is to obtain the two polymers functionalized at the side chain with maleimide and at the terminal ends of the main chain with the arginine-ending peptide. This will serve as the starting point for the preparation of polymeric nanoparticles through complexation with pGFP (17), followed by subsequent functionalization with anti-EGFR nanobodies.

Figure 32: Deprotection reaction of C6 polymer complex

C32 - protected maleimide - CRRR peptide complex

C32 - maleimide - CRRR peptide complex

Figure 33: Deprotection reaction of C32 polymer complex

$^1\mathrm{H}$ NMR spectra analysis of C6 - maleimide - CRRR peptide

In Figure 34, the result of the deprotection of the already linked maleimide is shown. At 9.0-7.0 ppm range the presence of the arginine peptide is detected. The signals at 6.5 ppm and 5 ppm, respectively related to diacrylates were not present. The latter result (absence of 5 ppm signal) is a strong evidence of the successful deprotection of the maleimide. The remaining signals remain unchanged, confirming the preservation of the integrity of the final product.

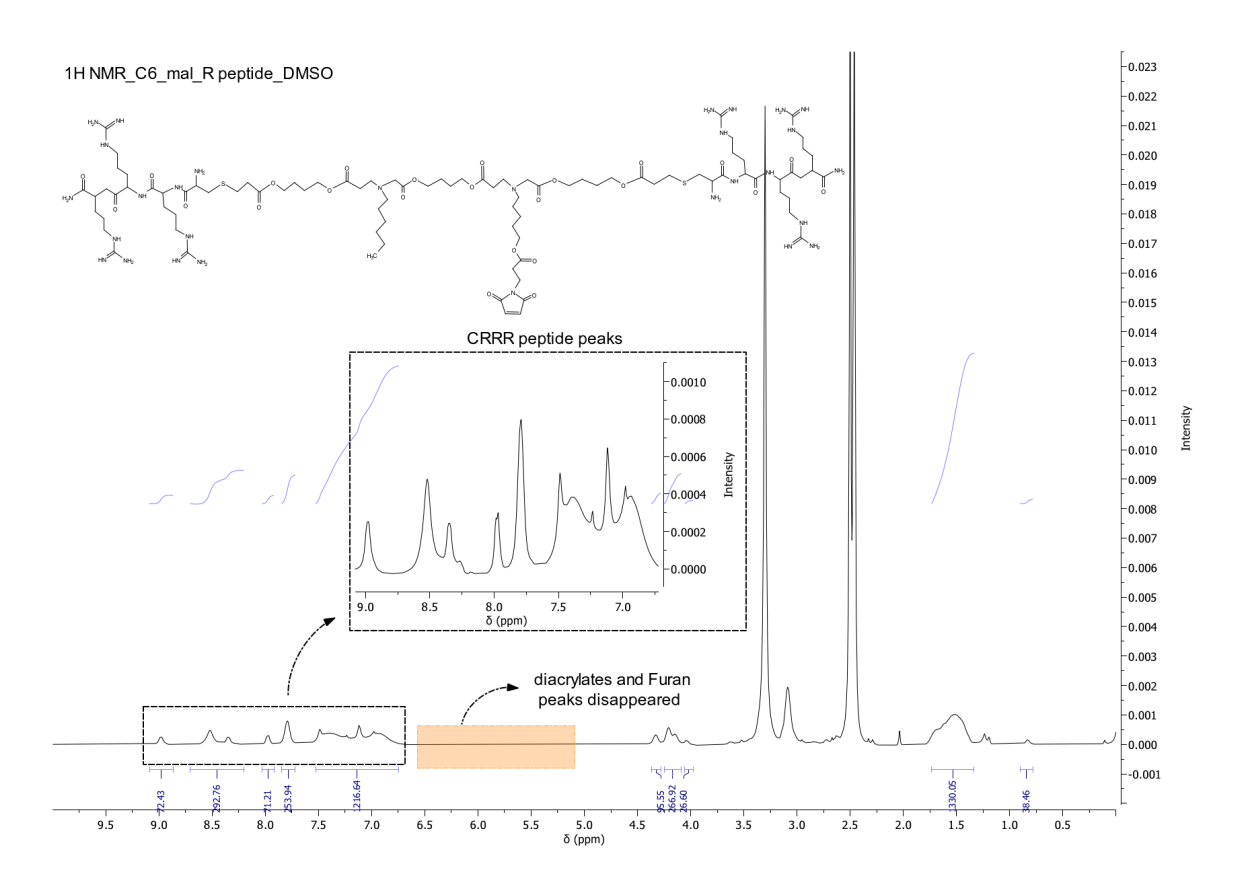


Figure 34: ¹H NMR spectra of C6 - maleimide - CRRR peptide; solvent used: DMSO

¹H NMR spectra analysis of C32 - maleimide - CRRR peptide

As for C6 polymer complex, In Figure 35, the result of the deprotection of the already linked maleimide is shown. At 9.0-7.0 ppm range the presence of the arginine peptide is detected. There are no signals at 6.5 ppm and 5 ppm, respectively related to diacrylates. Finally, the absence of the signal at 5 ppm proof the successful deprotection of the maleimide. The remaining signals remain unchanged, and it confirms the integrity of the final product.

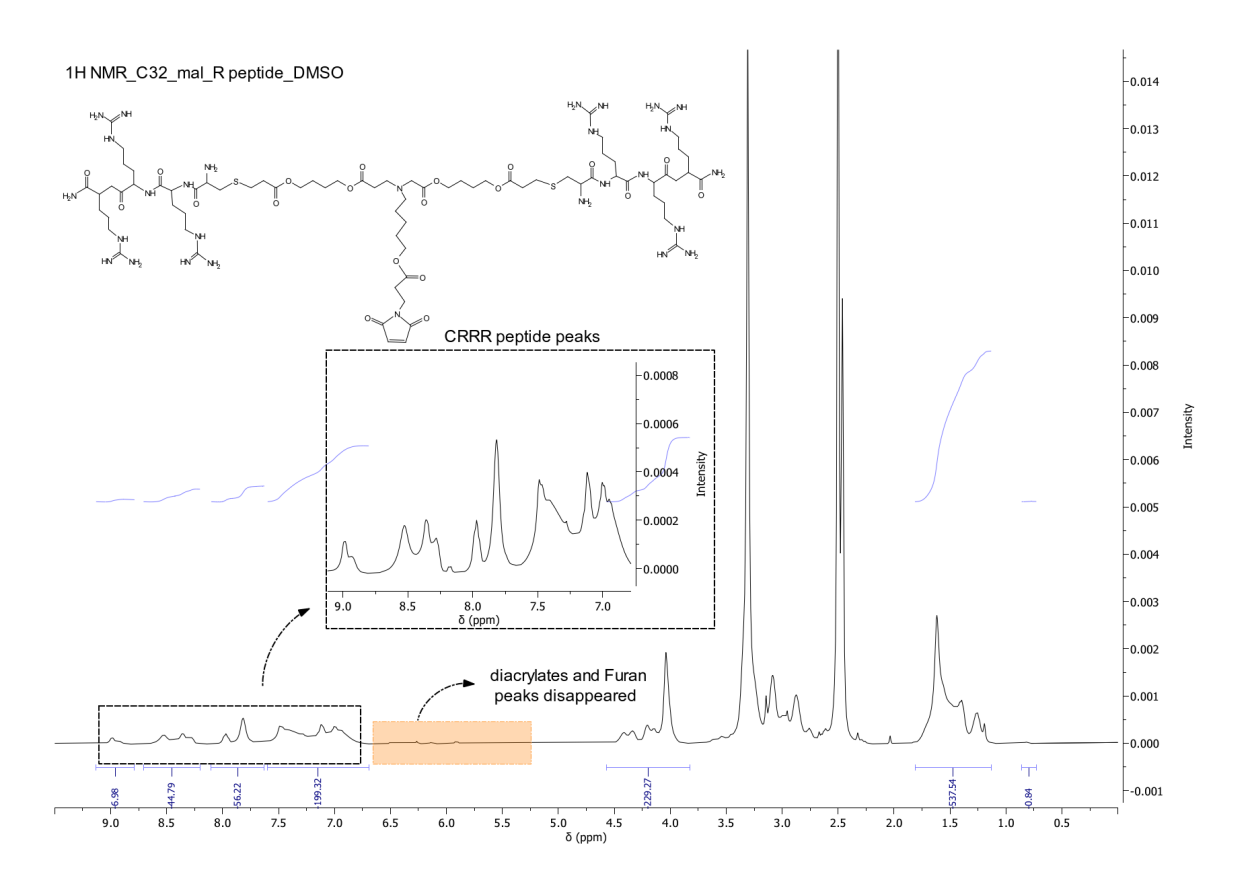


Figure 35: ¹H NMR spectra of C32 - maleimide - CRRR peptide; solvent used: DMSO

4.1.6 Characterization of pBAE NPs at different ratios

Using the polymers synthesized until here with he two starting polymers (Figure 36), pBAE NPs have been formulated by electrostatic interaction.

C6 - maleimide - CRRR peptide complex

C32 - maleimide - CRRR peptide complex

Figure 36: C6/c32 polymers complex as the results of functionalization with protected maleimide, attachment of CRRR peptide and the subsequent deprotection of maleimide; These two polymers will serve as the starting point for nanoparticles formation

In the following section, the different pBAE nanoparticle formulations will be characterized in order to assess and select the optimal formulation for both polymers, based on the different polymer-to-genetic material ratios.

The nanoparticles were prepared following the standard protocol adopted at the IQS laboratories for the fabrication of pBAE nanoparticles. In this work, as previously mentioned, one of the two polymers used in the standard method was replaced with the C6 and C32 polymers, previously synthesized and further modified through subsequent functionalizations. The rationale behind this choice lies not only in the preparation of

particles capable of optimally complexing with genetic material (due to the addition of cationic peptides to the polymer backbone), but also in the possibility of further functionalization with nanobodies via click chemistry [54]. This strategy aims to achieve greater specificity and selectivity of the nanoformulation towards tumor cells expressing the EGFR receptor, to which the nanobodies employed display affinity [55].

For both polymers, the nanoparticles were characterized by first evaluating the hydrodynamic diameter through DLS and the stability of the nanoformulation based on the zeta potential results [56]. To achieve a more robust characterization, an agarose gel electrophoresis protocol was performed to assess the encapsulation efficiency of pGFP by the different formulations and polymer-to-genetic material ratios [57]. The aim was to obtain stable nanoparticles with a size under (or close to) 200 nm.

In Figure 37, the results of the DLS characterization are reported. All the formulations were tested in the same conditions and the polymer – to- pGFP ratio was subsequently raised from 25:1 to 100:1. Regarding the size, for C6 polymer the most promising result were obtained with 50:1 and 75:1 ratios since the size was close to 200 nm of hydrodynamic diameter. Based on the zeta potential results, all C6 polymer formulations at the different ratios were consistent with the expected outcome, as they all exhibited a clear positive charge, indicating the stability of the formulation.

Regarding the particle sizes of the C32 polymer formulations, the 25:1, 50:1, and 100:1 ratios were consistent with the expected values, while the zeta potential results showed that all formulations exhibited a positive charge, in agreement with the expected outcomes.

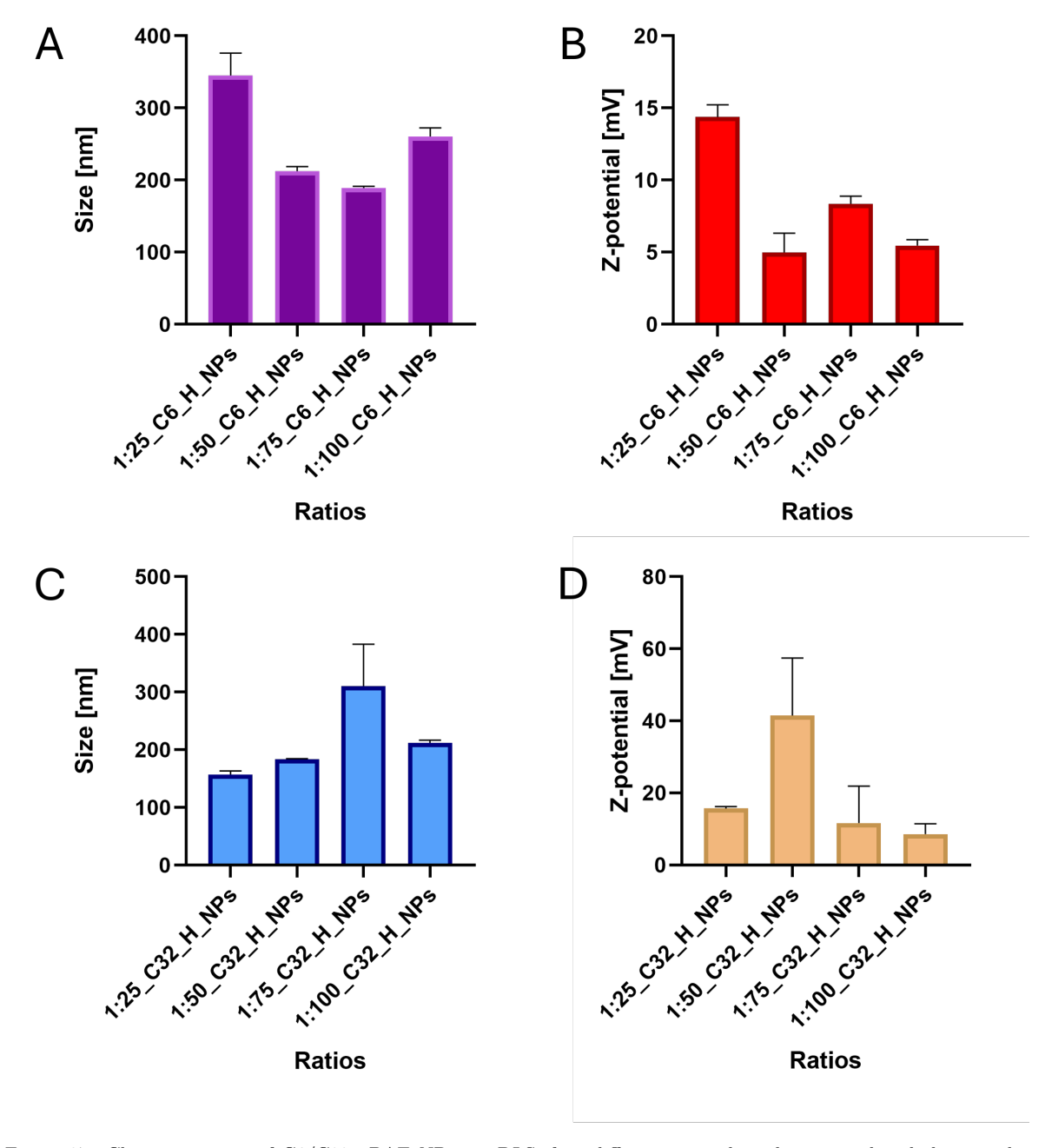


Figure 37: Characterization of C6/C32 pBAE NPs via DLS; four different ratios have been tested and their results have been reported. In A and C are respectively reported the results of C6 and C32-based formulations about the hydrodynamic diameter while in B and D are respectively reported the results of the surface charge of C6 and C32-based formulations

Figure 38 shows the result of the agarose gel electrophoresis. The gel wells were loaded, from left to right, with the substrate, a quantity of pGFP as control, and subsequently the different nanoformulations at various ratios (1:25, 1:50, 1:75, 1:100). The image clearly indicates that almost all nanoformulations exhibit good encapsulation, with the

exception of the C6 1:100 formulation. One possible explanation is that at the 1:100 ratio, the cationic polymer is present in large excess compared to the anionic nucleic acid (pGFP). Consequently, the not-optimal results observed at this ratio may be attributed to a charge imbalance.

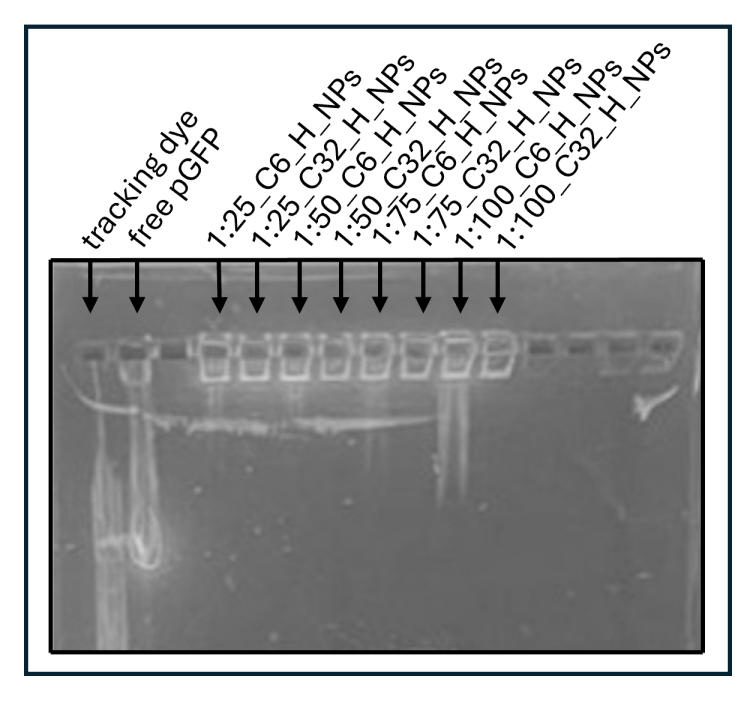


Figure 38: Agarose Gel electrophoresis of C6/C32 pBAE NPs at different ratios in order to assess the encapsulation efficiency

From this initial characterization, the optimal nano formulations to proceed with the subsequent functionalization steps and *in vitro* studies are those with ratios of 1:50 and 1:75 for the C6-based nanoparticles, while for the C32-based formulations the optimal ratios are 1:25 and 1:50.

4.1.7 pBAE NPs functionalization and subsequent characterization by NTA

This section reports the results related to the functionalization of the C6-based and C32-based nano formulations with anti-EGFR nanobodies. As described in the Materials and Methods section, the nanobodies need to be reduced before being able to bind to the nanoparticles. Specifically, the reduction step, achieved by adding 2-MEA in the reported amounts, aims to cleave the disulfide bonds in order to generate free terminal thiol groups. The nanobody-maleimide conjugation relies on click chemistry, which is characterized by: (1) the high specificity of thiol groups for maleimides; (2) the mild reaction conditions (aqueous buffer and physiological pH, without the need for metal catalysts); (3) the fast kinetics and high yield of the reaction. Moreover, the product of the reaction is a stable thioether bond, resistant to hydrolysis and physiological conditions, thereby ensuring that the functionalized nanoformulations remain stable and optimal under physiological environments [58].

The results before and after functionalization are reported for both nanoformulations. This choice was motivated by the aim of verifying how the addition of nanobodies on the nanoparticle surface could affect their size and stability. Specifically, prior to the actual analyses, the expected outcome was a slight shift in size toward values slightly higher than those obtained before functionalization [58].

Figure 39 shows the NTA results related to the characterization of the nanoformulations. For the C32-based formulations, the 1:25 ratio was selected, while for the C6-based formulations the 1:50 ratio was the chosen one. Focusing on the results, for C6-based formulations the size is closely maintained before and after the functionalization and it was around the range of 130 nm. For C32-based nanoparticles there is a slight shift in the functionalized nanoparticles, compared to the not-coated ones. In particular, from a size of 100 nm of non-functionalized nanoparticles, there is a shift towards values around 110 nm size.

A possible reason for the lack of size variation in the C6 polymer, unlike what is observed in the C32 polymer, could lie in the intrinsic structure of the polymer and its higher hydrophobic character. In particular, the side chains of the C6 polymer are more hydrophobic compared to those of C32 (which lacks the aliphatic side chain). Indeed, when nanobodies are introduced, the interface between the highly hydrophobic polymer and the aqueous environment can promote nonspecific interactions and particle aggregation. As a result, during NTA analysis, the particle size before and after

functionalization does not show significant variations, due to the limited stability of the nanoparticles, which may form clusters or exhibit low homogeneity.

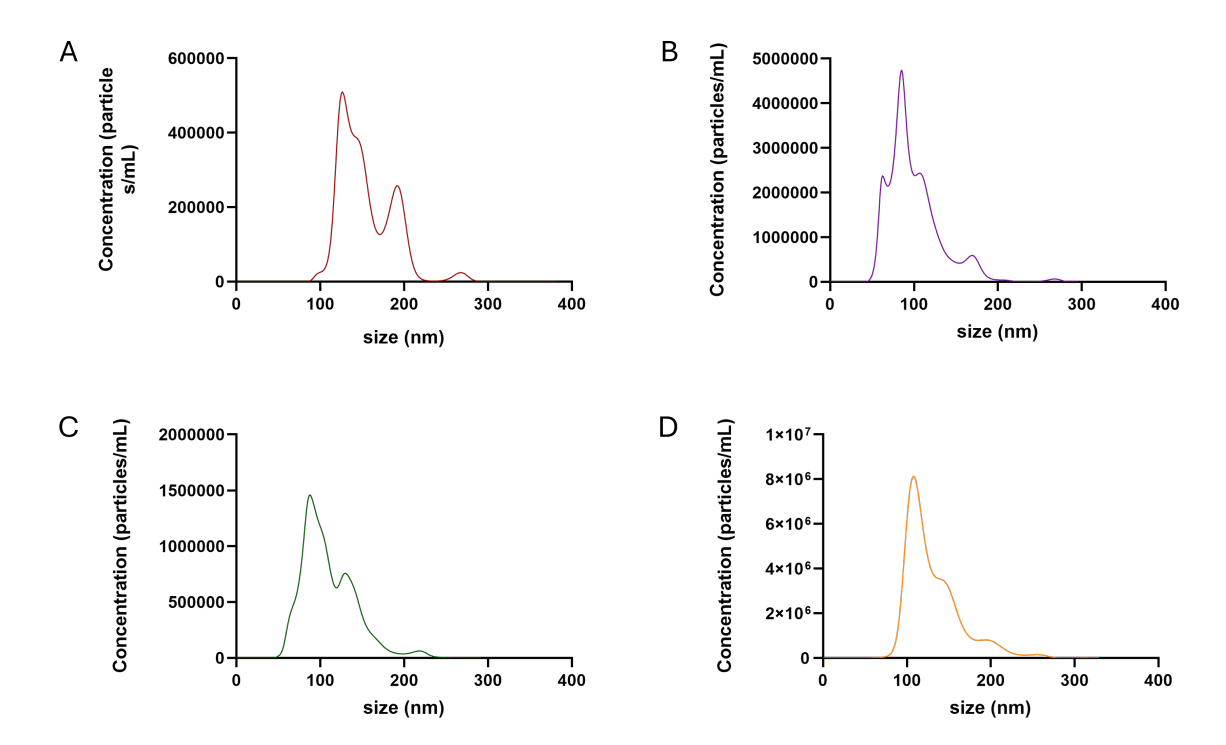


Figure 39: Results from pBAE functionalization with anti-EGFR nanobodies via NTA. In A and B are respectively reported the results from C6-based formulation before and after the functionalization with anti-EGFR nanobodies. In C and D are respectively reported the results from C32-based formulations before and after the nanobodies conjugation

4.2 Gold Nanoparticles: synthesis and characterization

In this section, it is presented the analysis of the results related to the gold nanoparticle formulations (AuNPs). As previously discussed, AuNPs are metallic particles that, when stimulated at specific frequencies of light (particularly through localized surface plasmon resonance, typically in the near-infrared region), undergo collective oscillation of their conduction electrons. This process leads to localized heating of tissues, making them suitable for photothermal therapy. Beyond their potential use in phototherapy, AuNPs can also serve as tools for tumor screening, as they exhibit characteristic absorbance and scattering/emission profiles at defined wavelengths [59]. These optical features allow them to be easily distinguished and detected, thereby enabling the identification of tumor sites.

In this work, as described in the Materials and Methods section, AuNPs were successfully functionalized with anti-EGFR nanobodies by exploiting the high affinity of terminal thiol groups for the gold surface [60] [61] (27). This functionalization rendered the nanoformulations highly specific toward cells overexpressing the receptor in the tumor microenvironment, thereby significantly enhancing their tumor screening capability.

The following subsections will first describe the characterization of the gold nanoparticle formulations after the synthesis protocol, in order to confirm the success of the reaction, enabling subsequent steps. The formulations will then be further characterized after functionalization with nanobodies at different ratios and the addition of PEG 5k. Finally, in the last section, the optical properties of the different formulations will be analyzed to provide a comprehensive overview and to identify the most promising formulation. From the characterization results, the hydrodynamic diameter of the non-functionalized AuNPs is expected to be around 30 nm or approximately 50 nm, with a negative surface charge [62]. Once functionalized, the formulations are expected to show slightly larger hydrodynamic diameters compared to 30 nm, while maintaining an overall negative surface charge [63] [64].

4.2.1 Hydrodynamic diameter via DLS and NTA and zeta potential

The synthesis protocol was carried out in triplicate in order to ensure greater reliability of the results and the success of the reaction. Characterization was performed using both DLS and NTA. The combination of two different techniques was intended to confirm that the properties of the nanoformulations were consistent with the expected outcomes.

In Figure 40 the results from the characterizations are reported. To prove consistency across the synthetic procedure, three independent samples from three independent synthesis were analyzed. Starting with the size, all three samples show values around 30 nm with a PDI below or close to 0.3, indicating the homogeneity of the solutions. The PDI values obtained and reported in the bar chart from DLS do not indicate a high level of heterogeneity, but rather a moderate size distribution, which is common in nanoparticle suspensions produced by chemical synthesis in solution. An explanation to this is related to the high sensitivity of DLS to a small number of aggregates or scattering variations, which can lead to an overestimation of the PDI.

On the other hand, the NTA results (Figure 41) graphically confirm that the nanoformulations remain homogeneous in the overall.

Regarding the zeta potential results (Figure X, right), all three samples exhibit a net negative charge, which is typical of gold-based nanoformulations. This latter result confirms the stability of the AuNP solutions. In particular, the most promising result is the one of sample 2, which will be further used in the functionalization steps.

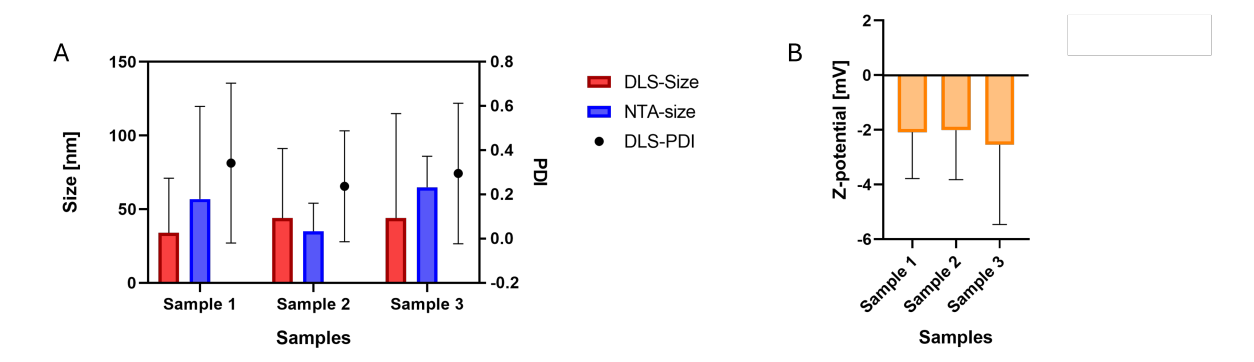


Figure 40: AuNPs characterization via DLS; hydrodynamic diameter results are reported (A) and surface charge results are reported (B)

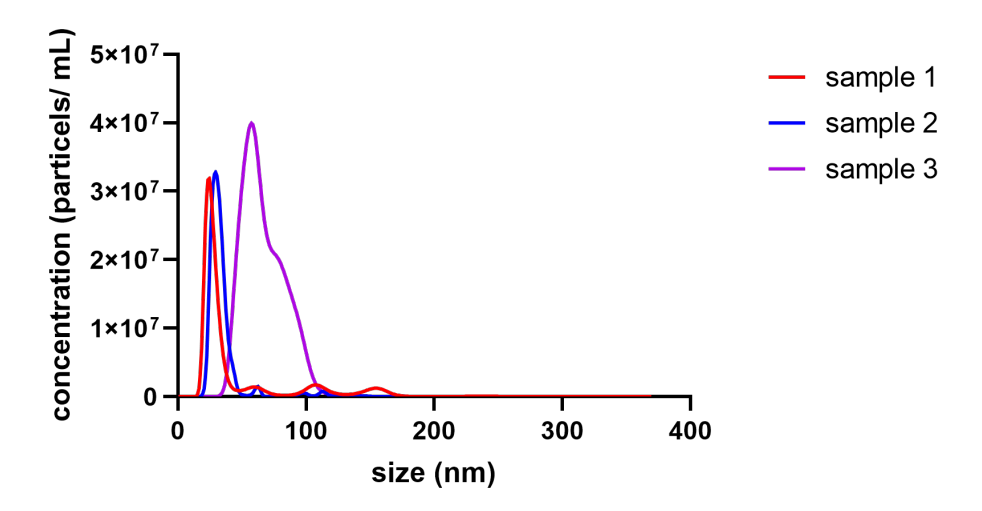


Figure 41: AuNPs characterization via NTA results; This analysis stands as a comparison to better characterize the results obtained via DLS and to strenghten the reproducibility of the synthesis technique via Turkevich method

Effect of nanobody functionalization at different ratio and PEG addition

As previously explained, gold nanoparticles need to be functionalized if the main aim is to target specific type of cells and to avoid the non-specificity of the binding. To do so, anti-EGFR nanobodies have been used to functionalize AuNPs too.

Talking about the preparation of nanobodies solution, it was first reduced by using 2MEA in the same concentration of pBAE NPs treatment and a different volume of the reduced solution was added to AuNPs solution. Subsequently, PEG 5k was added in the quantities reported below. The idea of adding the PEG in the coating was to prevent any aggregations from nanoparticles after the change of size and stability due to the functionalization with nanobodies. The selected volumes were determined based on a calculation involving the molar ratio between the initial concentration of the AuNP solution (50 μ g/mL) and the corresponding stock concentration of nanobody, previously reduced with 2-MEA, which was 1.52 mg/mL. The latter, in order to obtain pipettable volumes, was further diluted by a factor of 1:5, resulting in a final concentration of 0.305 mg/mL. The volumes of the reduced nanobody solution were then derived according to the ratios 1:10, 1:5, 1:2, 1:1, 1:0.5, and 1:0.25. Before performing any characterization using a specific instrument, the 6 vials (referred to 6 different ratios) were monitored in case there was a change of colour in the solution. The expected outcome was to obtain a solution with the same colour (pinkish red) of the not-coated solution of AuNPs: after the addition of nanobodies it was in fact notable a slight change of colour which returned the original when the PEG 5k was added.

Therefore, the characterization of the nanoformulations using DLS and NTA was carried out to obtain robust results that could verify whether the formulations exhibited properties as close as possible to the expected outcomes. The hydrodynamic diameter was recorded by using NTA for each solution while the z potential lcharacterization was carried out by using the DLS.

In Figure 42 the results from NTA have been reported. The functionalized formulations were compared with the non-functionalized formulation. On the left, the non-functionalized formulation shows a hydrodynamic diameter of approximately 30 nm. On the right, it can be observed that, after functionalization, the hydrodynamic diameter of the nanoparticles increases due to the coating with nanobodies and PEG 5k. However, this increase remains consistent with the expected results, according to which only a moderate size enlargement was predicted. In all formulations, the PDI remains low, as graphically shown, indicating good homogeneity of the solutions.

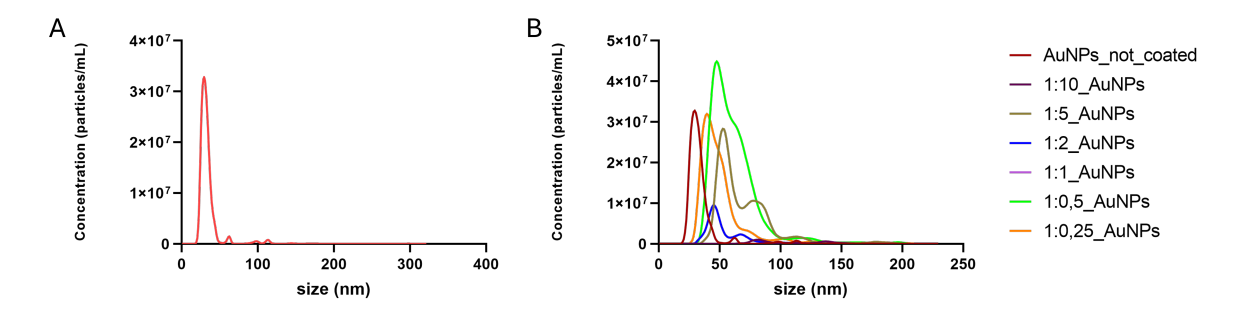


Figure 42: AuNPs characterization via NTA before and after functionalization with anti-EGFR nanobodies at different ratios. In A the results of the not-functionalized Au formulation are reported. In B, a comparison between the not-functionalized and different ratios AuNPs formulations is reported to better understand the optimal ratio AuNPs:nanobodies solution

In Figure 43, the DLS results regarding the zeta potential are reported. It can be observed that all formulations, both functionalized and non-functionalized, exhibit a pronounced negative charge, which is characteristic of gold-based nanoformulations.

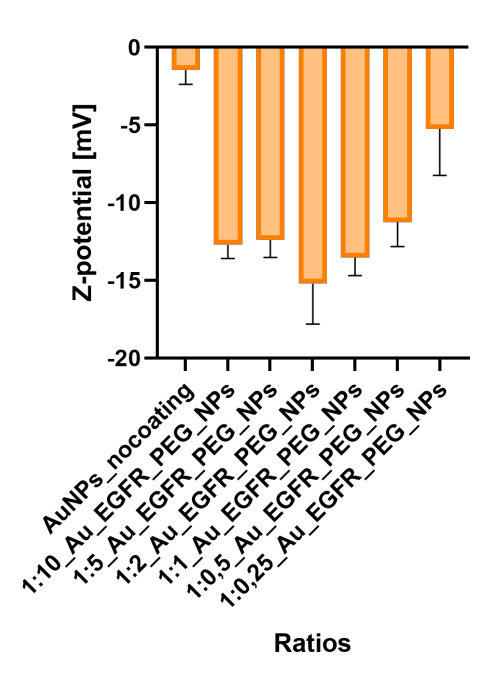


Figure 43: AUNPs surface charge characterization via DLS before and after the functionalization with anti-EGFR nanobodies

Considering the results from both the instruments used, the most promising nanoformulations are those using 1:0,5 and 1:0,25 ratio. These are the formulations that were the closest to expected outcomes of having negative charge and a slight increase in the

size (preserving the PDI). In Figure 44 a comparison between the not-coated solutions and two functionalized nanoformulation is reported.

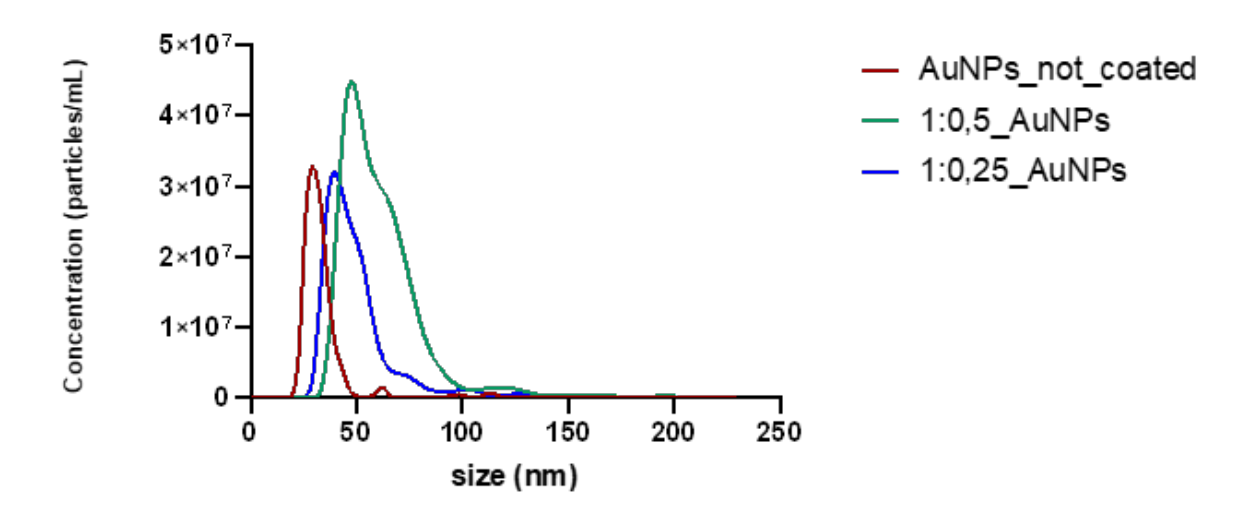


Figure 44: Optimal results from AuNPs functionalization; 1:0.5 and 1:0.25 ratios have been selected as the most promising among all the tested ratios

4.2.2 UV-Vis absorbance of AuNPs

In this section, the results of the UV-Vis spectroscopy analysis are presented, comparing the absorbance spectra of the non-functionalized formulation with those of the functionalized formulations at different ratios. In particular, it is expected that, once functionalized, the formulations will maintain the same or similar optical properties, allowing their potential use in phototherapy and tumor screening.

Normally, AuNPs display a peak at 525 nm, which is expected to be observed in the non-functionalized formulation. Once the coating is obatined, a shift of the absorbance band is expected, due to the aggregation of the AuNPs. In Figure 45, the results from UV-Vis spectroscopy are reported. The non-functionalized formulation exhibits a peak at 525 nm, and a slight shift of the absorbance values can be observed in the formulations at the different functionalization ratios [65].

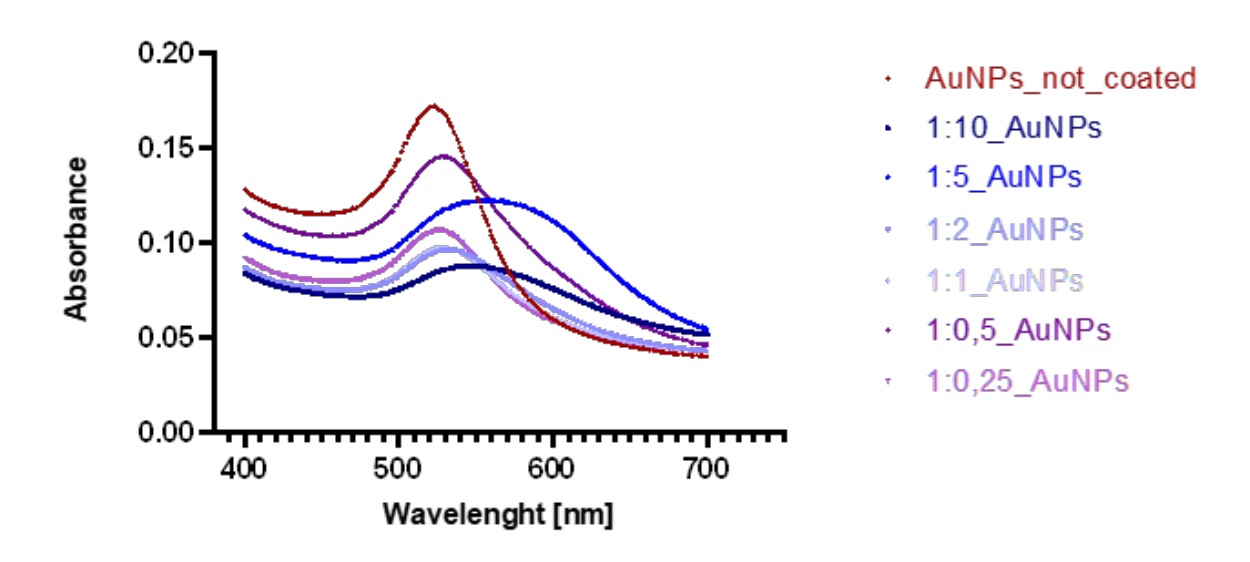


Figure 45: UV-Vis Results to assess the mainteinment of AuNPs optical properties after functionalization

4.3 In vitro evaluation

In the following section, the *in vitro* results have been carried out to assess the expression of the target receptor onto four different cell lines, previously mentioned in materials and methods section.

Flow cytometry analysis was first performed on the MDA-MB-231 and BT549 cell lines, followed by a Western blot assay on MDA-MB-231, BT549, A375, and SK-MEL-28, in order to confirm receptor expression in the first two cell lines and to include two additional lines as potential analysis models.

Subsequently, the biocompatibility of the nanoformulations and transfection will be tested in a breast cancer cell line.

4.3.1 EGFR expression profiling across four cell lines

Before testing nanoformulations' efficacy, it is needed to assess that target EGFR receptor is expressed in the four cell lines. The aim is to firstly verify EGFR presence in order to take advantage using a formulation engineered to reach that specific target. Secondly, this assessment is useful in order to select an appropriate model where the receptor is expressed to allow measurable differences between targeted and non-targeted formulations.

4.3.1.1 Quantification of surface EGFR by flow cytometry

MDAMB231 cell line

In Figure 46 the flow cytometry analysis on MDAMB231 is reported. The analysis highlighted a net positivity for EGFR receptor. In particular, compared to negative controls, the population marked with anti-EGFR displays a clear shift of the signal (99,5% of cells EGFR positive). On the other hand, the treatment with anti-HER2 receptor did not show any differences compared to the control sample, showing how this cell line does not express HER2 on the surface. These data are a first verification

about MDAMB231 as a proper model for testing targeting nanoformulation anti-EGFR.

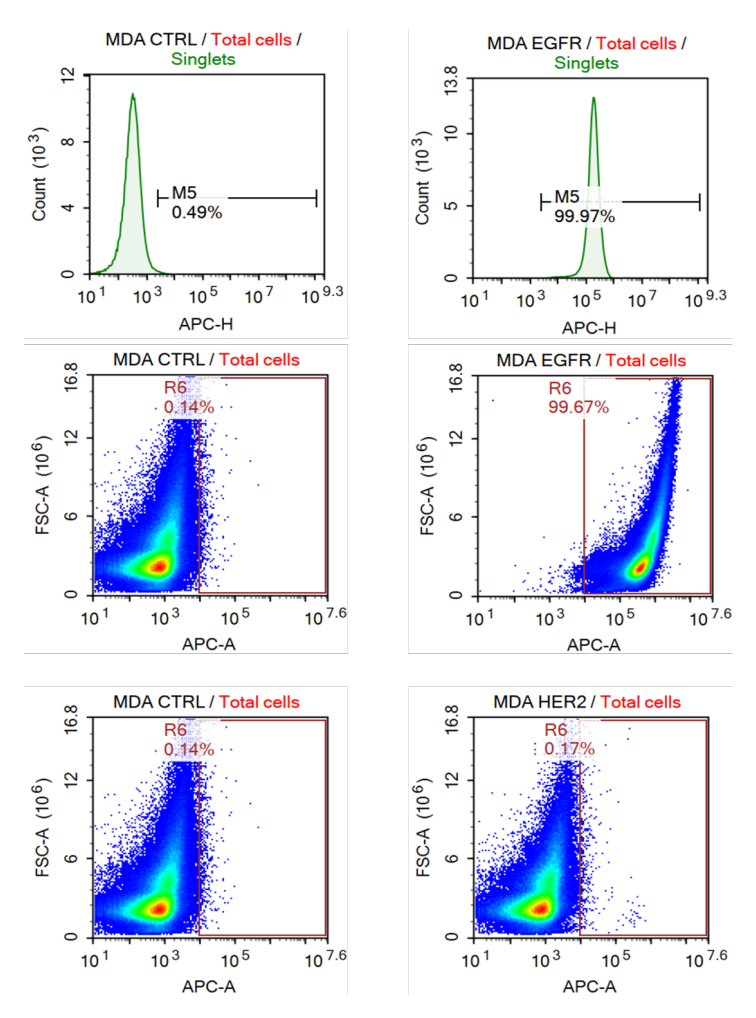


Figure 46: EGFR expression profiling of MDAMB231 cell line

BT549 cell line

In Figure 47 the flow cytometry analysis on BT549 cell line is reported. The analysis shows a high expression of EGFR receptor. Compared to negative controls, the population marked with anti-EGFR displays a clear shift of the signal ($\approx 99.9\%$ of EGFR-positive cells). By contrast, the treatment with anti-HER2 receptor did not present any differences compared to the control sample, showing how this cell line does not express HER2 on the surface. These data are a first verification about MDAMB231 as a proper model for testing targeting nanoformulation anti-EGFR.

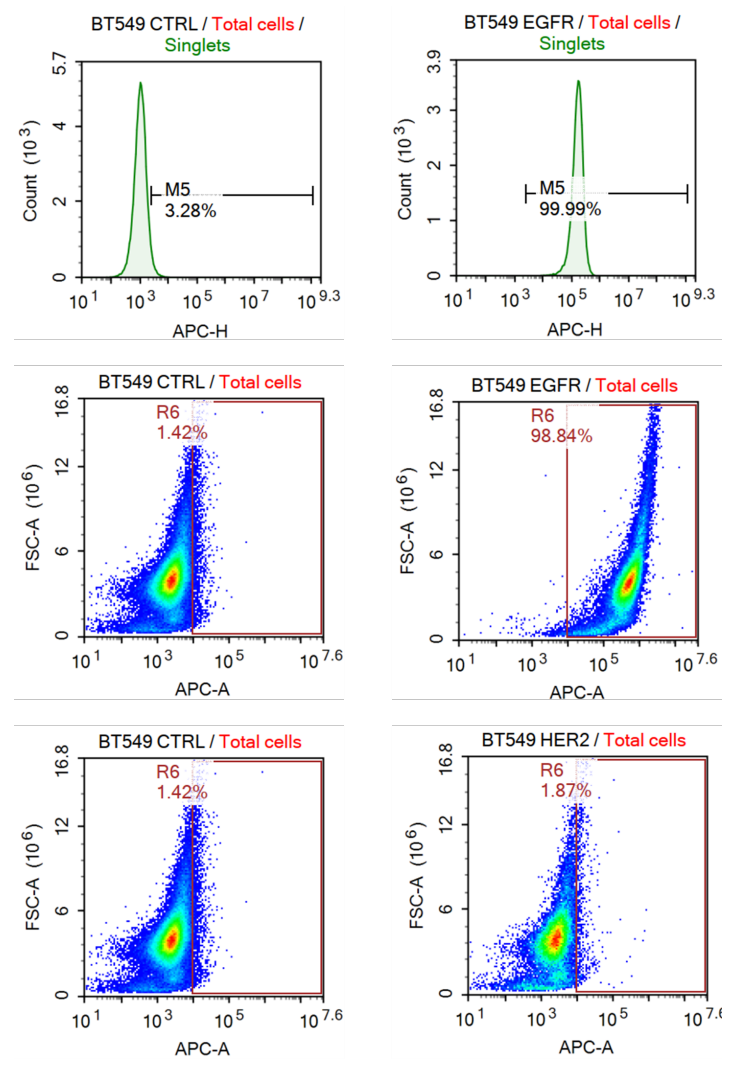


Figure 47: EGFR expression profiling of BT549 cell line

4.3.1.2 EGFR protein levels by Western blotting

In the following section, the results of the western blot analysis are presented. In addition to the two cell lines previously analyzed by flow cytometry, two further cell lines were included: BT474 and SK-MEL-28. The purpose of this analysis is to confirm the results obtained in the previous experiment and to visually verify the expression of the EGFR receptor.

In Figure 48, the results are reported. From left to right, the lanes correspond to MDA-MB-231, BT549, A375, and SK-MEL-28. In all four cell lines, the expression of the EGFR receptor is visible in the highlighted band.

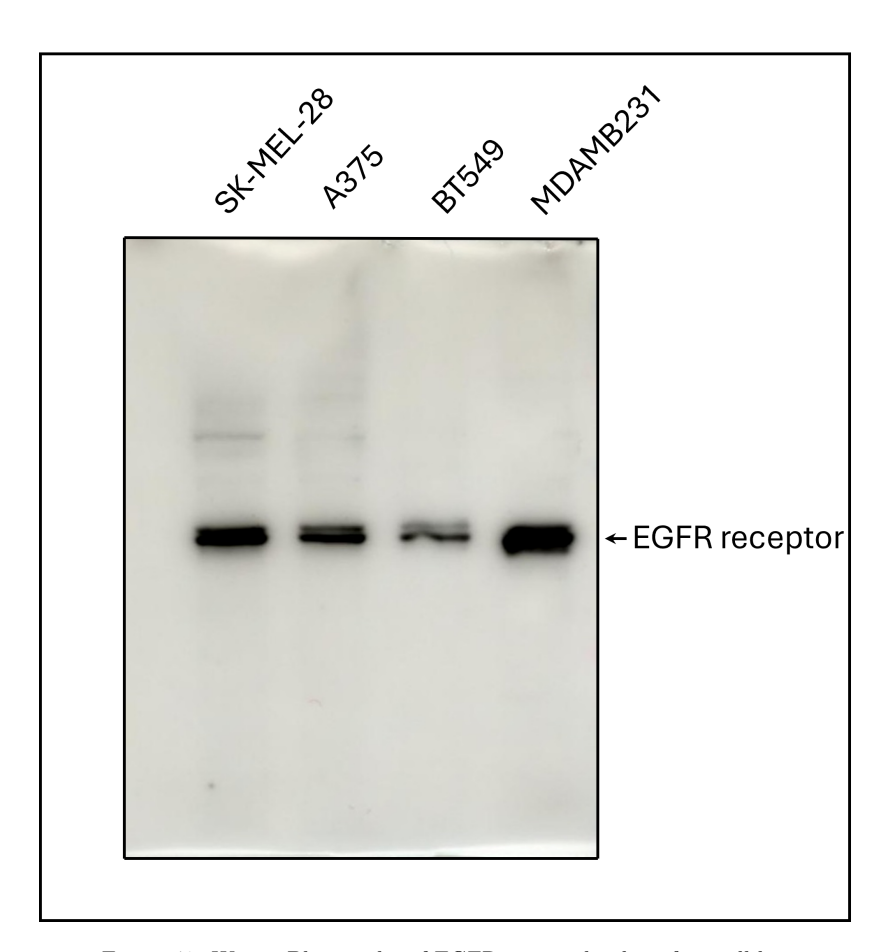


Figure 48: Wester Blot results of EGFR protein levels in four cell lines

4.3.2 Cytotoxicity by MTT Assay at 24 h and 48 h

In this section, the results of the MTT assay at 24 h and 48 h are presented with the aim of evaluating the cytotoxicity of the nanoformulations in one of the previously analyzed cell lines. In particular, the MDA-MB-231 cell line was selected, as it proved to be an optimal model for testing anti-EGFR targeted nanoformulations.

Regarding the formulations employed, for the AuNPs the functionalized systems were tested at different ratios. As for the pBAE nanoparticles, the C32-based formulations, both functionalized and non-functionalized, were tested at a ratio of 1:25; while for the C6-based formulations, a ratio of 1:50 was selected, as it was among the optimal results of the previous analysis the closest to the standard polymer-genetic material ratio.

In addition to a negative control, in which the cells were treated with culture medium only, Lipofectamine nanoparticles (Lipo NPs) encapsulating pGFP were selected as the positive control.

This choice was made because Lipo NPs exhibit both a high transfection efficiency and a marked cytotoxicity, thus serving as an appropriate reference model for comparison with the nanoformulations under testing.

MTT assay with AuNPs

The MTT assay performed at 24 h and 48 h showed that all gold nanoformulations (Figure 49) exhibited high cellular tolerability, with viability values exceeding those of the negative control. In particular, the 1:5 and 1:0.25 formulations displayed an apparent increase, which may reflect either an enhancement of mitochondrial metabolic activity induced by the nanoparticles or a possible optical interference with the MTT assay. The latter phenomenon has already been reported in the literature for models employing gold-based formulations and should not be interpreted as a genuine increase in cell proliferation. AuNPs may induce a transient rise in mitochondrial activity, leading to a faster reduction of the MTT salt into formazan, thereby resulting in an overestimation of the optical signal [66]. As for the second possible cause, AuNPs can interact with the test reagents or with the formazan product itself, interfering with the absorbance reading at a specific wavelength and generating artificially elevated values. In any case, no cytotoxicity was observed for any of the formulations tested, at either 24 h or 48 h [67].

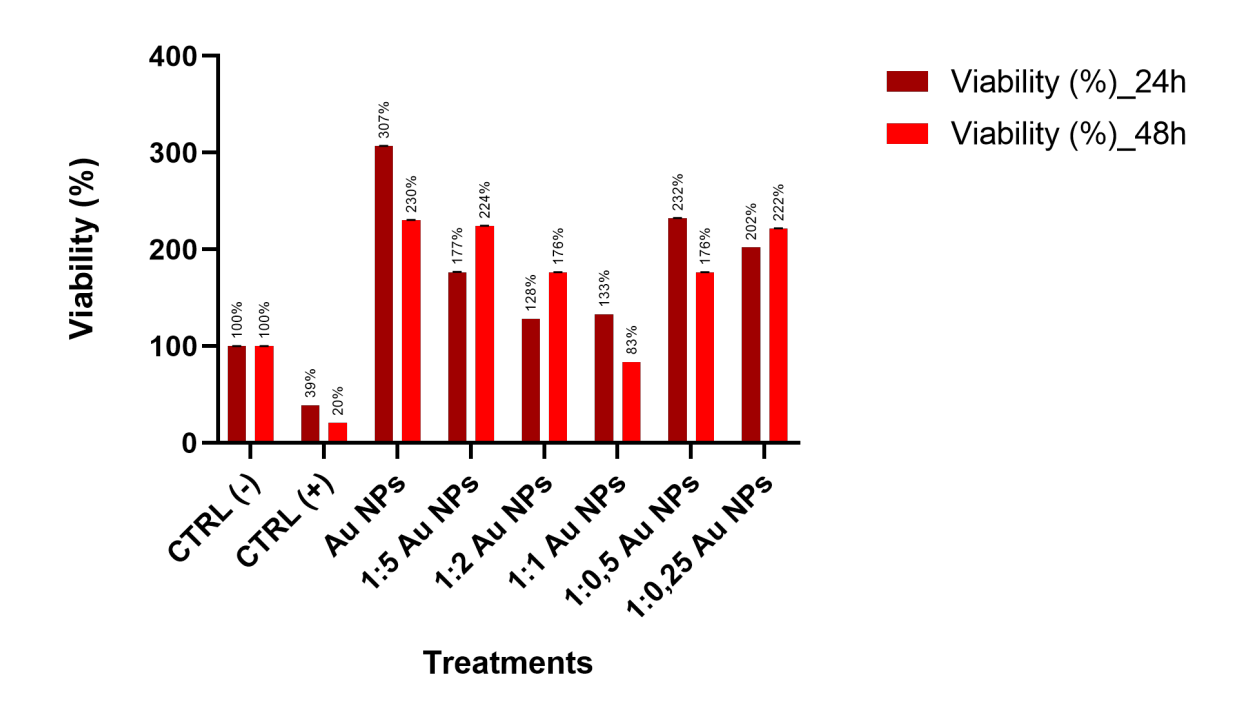


Figure 49: MTT assay results of AuNPs treatment; the comparison was made with only DMEM and Lipofectamine Nanoparticles

MTT assay with pBAE NPs

Regarding the MTT assay performed at 24 h and 48 h on the polymeric nanoparticles (Figure 50), the results showed that all pBAE nanoformulations exhibited good cellular tolerability. In particular, treatments with pBAEs, when compared to the negative and positive controls, maintained cell viability values above 90% even at 48 h. An apparent increase in viability was observed at 24 h, which can be attributed to enhanced metabolic activity induced by the nanoparticles rather than to a genuine increase in cell proliferation. Several reports have demonstrated that pBAE polymers exhibit markedly lower cytotoxicity compared to other polycations commonly employed for gene delivery, such as polyethyleneimine (PEI) [68] [43]. This favorable profile is mainly attributed to their biodegradability, which stems from the presence of hydrolyzable ester bonds [31]. When comparing free and functionalized formulations, the functionalization with anti-EGFR nanobodies did not result in any additional toxic effects. Finally, in comparison with the positive control, the pBAE NPs demonstrated superior cellular tolerability. This finding further confirms the applicability of the tested formulations for gene delivery purposes.

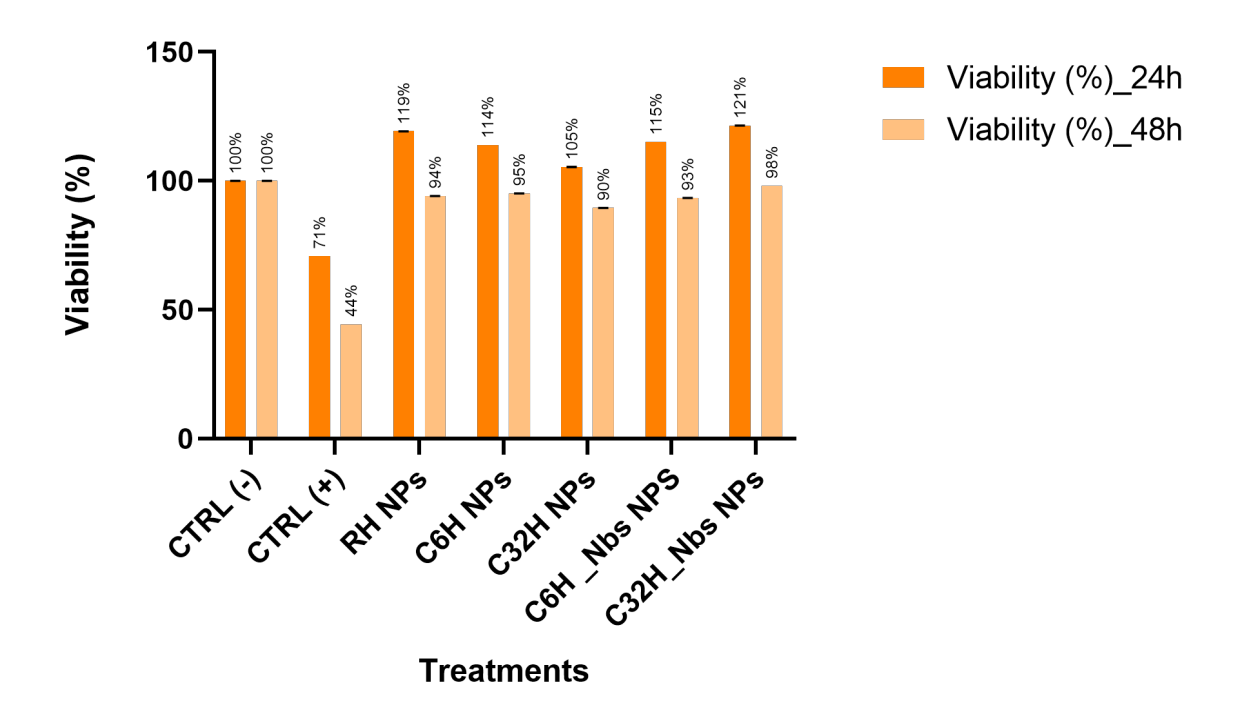


Figure 50: MTT assay results of pBAE NPs treatment; the comparison was made with only DMEM and Lipofectamine Nanoparticles

4.3.3 Transfection efficiency by flow cytometry

This section is dedicated to the results concerning the transfection of the MDA-MB-231 cell line with the different pBAE formulations encapsulating pGFP. Specifically, GFP is expressed in the cells once the plasmid is delivered. The use of pGFP allows for an immediate and, above all, quantitative readout of transfection efficiency by flow cytometry, without the need for additional substrates or multiple processing steps [69] We had two controls, a negative one that consisted in the cells without any treatment and a positive control, cells treated with lipofectamine NPs which is highly toxic but presents a high transfection efficiency. Being composed of cationic lipids, its strong affinity for the phospholipid membrane facilitates interaction and promotes internalization through endocytosis. Once inside the cell, the cationic lipids induce membrane destabilization and trigger the so-called 'endosomal escape' mechanism, which enables the release of the genetic cargo into the cytoplasm.

Figure 51 reports the results obtained for the negative and positive controls, as well as for the treatment with standard RH NPs. The negative control displayed a negligible fluorescence level, below 1%. The positive control, represented by Lipo NPs, resulted in a high percentage of GFP-positive cells, in line with the expected outcomes reported in the literature. Finally, RH NPs achieved lower values compared to the positive control, with approximately 18–20% of transfected cells. The results obtained so far, when combined with the MTT assay data, confirm the suitability of RH NPs as a biocompatible polymeric system for gene delivery. The following sections will analyze the remaining treatments to provide an overall perspective from which conclusions can be drawn. Moreover, Figure 51 shows the results related to the PBAE NP formulations based on C6 and C32 polymers. Functionalized formulations were compared with the nonfunctionalized NPs to assess the contribution of nanobody functionalization to the enhancement of transfection efficiency. The analysis conducted on the nanoformulations based on C6 and C32 polymers revealed significant differences between the nanobodyfunctionalized and the non-functionalized versions. For the C6H NPs, functionalization led to only a slight increase in the percentage of transfected cells compared to the free formulation (21.7% \rightarrow 22.6%). In contrast, the C32-based nanoformulations showed a pronounced improvement upon functionalization, with transfection rates rising from 24.1% to 34.8% GFP-positive cells. These results suggest that EGFR-targeting through nanobody conjugation can enhance transfection efficiency, although the degree of this effect depends on the specific polymer formulation.

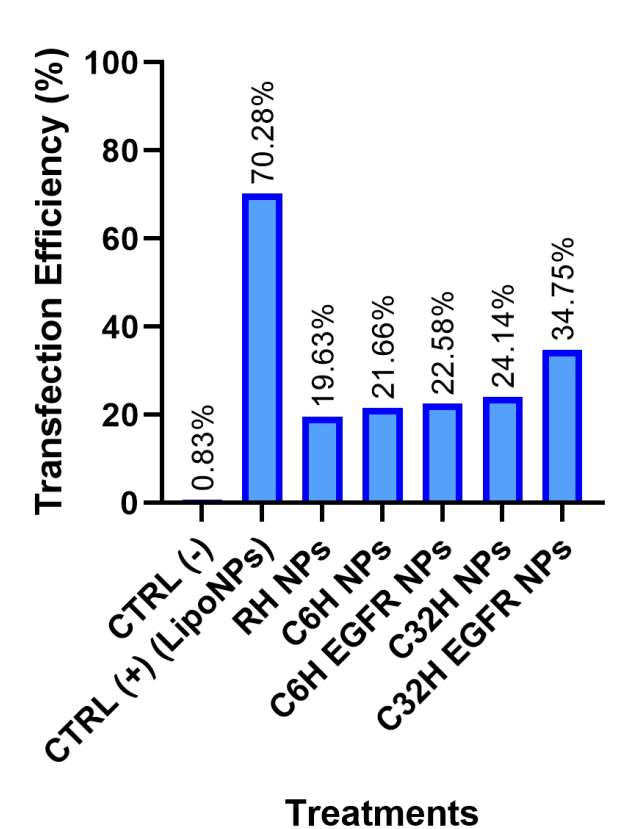


Figure 51: Transfection Efficiency results via flow cytometer of pBAE NPs before and after functionalization with anti-

EGFR nanobodies

5 Conclusions

The first objective of this thesis work was to investigate two different nanosystems: polymeric nanoparticles based on pBAE and AuNPs. The main objective was to enhance selectivity and effectivity of both nanosystems through the functionalization with anti-EGFR nanobodies.

As previously explained, this strategy aims to combine the efficiency of nucleic acids delivery with the ability to selectively recognize target cells, limiting undesired side effects.

About the preliminary chemical characterization, the synthesis of C6 and C32 polymer led to reproducible structures consistent with the most recent literature. Indeed, NMR spectra analysis confirmed the integrity of the polymeric backbone for each polymer and validated the functionalization with maleimide via esterification. In particular, maleimide functionalization has represented a key step since it allowed both polymers' structure to acquire an optimal conjugation site for the subsequent nanobody functionalization, thanks to click chemistry.

A screening phase in the pBAE NPs was carried out across different polymer:genetic material ratios (1:25, 1:50, 1:75, 1:100). This approach enabled the identification of proper conditions leading to more stable systems in terms of physiochemical properties. DLS and NTA analyses displayed that C6 optimal conditions in terms of hydrodynamic diameter (around 200 nm) were represented by 1:50 ratio, meanwhile for C32 the optimal ratio was 1:25.

For AuNPs, the synthesis via Turkevich method resulted in stable particles with a hydrodynamic diameter around 30 nm and a negative surface charge through the characterization by DLS and NTA. The successful formation of the gold nanosystems was confirmed, showing quite low PDI values and related homogeneity.

Moving on the functionalization with nanobodies, the results for pBAE NPs highlighted different behaviours between the two polymeric nanosystems. C32-based nanoformulations displayed good stability and consistent size variation after nanobody conjugation. For C6-based nanoformulations the results were less clear: the cause is attributable to the intrinsic hydrophobicity of C6, influencing aggregation of nanobodies on the surface. Further investigations need to be optimized for C6-based nanoformulations.

Taking into account the *in vitro* studies, flow cytometry analysis revealed strong EGFR receptor expression on the surface of MDA-MB-231 and BT549 cell lines. In particular, MDA-MB-231 was selected as the main model for subsequent transfection assays. In parallel, western blot assays confirmed EGFR expression across all the cell lines: MDA-MB-231, BT549, as well as A375 and SK-MEL-28. This dual approach enforced the evidence supporting the use of these cellular systems for nanobody-mediated targeting studies.

In terms of cytotoxicity, pBAE NPs presented viability values over 90% after 24h and 48h in all tested conditions, confirming the low toxicity of these polymers. For AuNPs, the results also demonstrated a good level of cellular tolerability. In some cases, an apparent increase in viability was observed, a phenomenon already reported in the literature and attributable not to a real increase in proliferation but rather to optical interferences of gold-based systems with the MTT assay or to transient increases in mitochondrial metabolic activity.

Finally, regarding the evaluation of transfection efficiency, the results showed that polymeric nanoparticles functionalized with anti-EGFR nanobodies displayed a slight but significant increase in the percentage of GFP-positive cells compared to the corresponding non-functionalized formulations. This effect was more evident in the C32-based formulations, in agreement with the findings from the physicochemical characterization. However, these results require further validation: both in terms of optimizing the amount of nanobody used for functionalization, and in terms of reproducibility and robustness of the *in vitro* outcomes. Additional experiments will therefore be necessary, in order to verify the actual conjugation efficiency and to confirm transfection data across more replicates and multiple cell lines.

To conclude, this thesis has achieved its initial objective not only in confirming the synthesis of two nanostructured systems but also in providing concrete results regarding the additional step represented by targeted functionalization, in line with the paradigm of targeted therapies. The analyses related to physicochemical characterization, together with subsequent *in vitro* evaluations, have suggested that both systems provide a promising basis for future development. Nevertheless, extensive optimization and validation in preclinical models remain essential in order to translate these systems into potential therapeutic and diagnostic tools in oncology.

6 Future Perspectives

The present study has laid the basis for the development of two distinct but complementary nanosystems: polymeric nanoparticles based on pBAEs and gold nanoparticles; both systems functionalized with anti-EGFR nanobodies. Although the preliminary results confirmed the feasibility of the synthesis and functionalization, numerous pathways of research remain that can be undertaken in order to consolidate and expand the applicative potential of the proposed approach.

A first field of development is related to the optimization of the polymeric formulations. In particular, further studies are needed on C6 polymer and how its greater intrinsic hydrophobicity which differentiates it from C32 polymer, is linked to the results obtained in the physicochemical characterization in terms of size and above all of the homogeneity of the nanoformulation.

A second development is represented by the systematic evaluation of the polymer:genetic material ratios. On this point, in the present work several ratios have been tested, but a more in-depth analysis is needed. Possibly, a coarse-grained computational simulation could clarify the dynamics of condensation and stabilization of the polymeric nanoparticles in terms of suggesting more robust and reproducible formulation conditions [70] [71].

Another crucial development concerns the comparison between two strategies of functionalization: functionalizing with nanobodies before or after nanoparticle analysis could reveal important differences in terms of stability of the formulation and above all transfection yield. Moreover, the proposed analysis could be useful to evaluate the accessibility of nanobodies bound to the polymer; the latter represents a crucial aspect to guarantee effective targeting towards tumour cells.

On the biological side, another development concerns a more extended *in vitro* validation. It will certainly be important to increase the number of cell lines to be tested, including other tumor subtypes characterized by EGFR overexpression as well.

Finally, as already mentioned, another line of research is represented by the use of

computational chemistry and molecular docking to analyse in detail the interaction between the conjugated nanobodies and the target receptors. By performing such simulations, it could be possible to predict the impact of chemical modifications (addition of linkers, the role of PEG in the nanobody-receptor interaction) on the orientation of the complementarity-determining region (CDR) loops. This approach could provide crucial information to improve the binding efficiency and reduce potential steric interferences with the receptors [72] [73] [74] [75].

These possible development approaches have the potential to transform the preliminary results of this work into an approach with concrete prospects of application in personalized medicine and in innovative therapies in oncology.

Bibliography

References

- [1] S. Zhang, X. Xiao, Y. Yi, X. Wang, L. Zhu, Y. Shen, D. Lin, and C. Wu. "Tumor initiation and early tumorigenesis: molecular mechanisms and interventional targets". en. Signal Transduction and Targeted Therapy 9.1 (June 2024), p. 149. DOI: 10.1038/s41392-024-01848-7.
- [2] D. Ostroverkhova, T. M. Przytycka, and A. R. Panchenko. "Cancer driver mutations: predictions and reality". en. *Trends in Molecular Medicine* 29.7 (July 2023), pp. 554–566. DOI: 10.1016/j.molmed.2023.03.007.
- [3] W. J. MacDonald, C. Purcell, M. Pinho-Schwermann, N. M. Stubbs, P. R. Srinivasan, and W. S. El-Deiry. "Heterogeneity in Cancer". en. Cancers 17.3 (Jan. 2025), p. 441. DOI: 10.3390/cancers17030441.
- [4] R. Stojchevski, E. A. Sutanto, R. Sutanto, N. Hadzi-Petrushev, M. Mladenov, S. R. Singh, J. K. Sinha, S. Ghosh, B. Yarlagadda, K. K. Singh, P. Verma, S. Sengupta, R. Bhaskar, and D. Avtanski. "Translational Advances in Oncogene and Tumor-Suppressor Gene Research". en. Cancers 17.6 (Mar. 2025), p. 1008. DOI: 10.3390/cancers17061008.
- [5] B. Tabanifar, H. Lau, and K. Sabapathy. "Tumor suppressor genes in the tumor microenvironment". en. *Disease Models & Mechanisms* 18.3 (Mar. 2025), p. dmm052049. DOI: 10.1242/dmm.052049.
- [6] T. C. Dakal, B. Dhabhai, A. Pant, K. Moar, K. Chaudhary, V. Yadav, V. Ranga, N. K. Sharma, A. Kumar, P. K. Maurya, J. Maciaczyk, I. G. H. Schmidt-Wolf, and A. Sharma. "Oncogenes and tumor suppressor genes: functions and roles in cancers". en. MedComm 5.6 (June 2024), e582. DOI: 10.1002/mco2.582.
- [7] S. R. Singh, R. Bhaskar, S. Ghosh, B. Yarlagadda, K. K. Singh, P. Verma, S. Sengupta, M. Mladenov, N. Hadzi-Petrushev, R. Stojchevski, J. K. Sinha, and D. Avtanski. "Exploring the Genetic Orchestra of Cancer: The Interplay Between Oncogenes and Tumor-Suppressor Genes". en. Cancers 17.7 (Mar. 2025), p. 1082. DOI: 10.3390/cancers17071082.

- [8] R. Huang and P.-K. Zhou. "DNA damage repair: historical perspectives, mechanistic pathways and clinical translation for targeted cancer therapy". en. Signal Transduction and Targeted Therapy 6.1 (July 2021), p. 254. DOI: 10.1038/s41392-021-00648-7.
- [9] H.-W. Chan, D.-Y. Kuo, P.-W. Shueng, and H.-Y. Chuang. "Visualizing the Tumor Microenvironment: Molecular Imaging Probes Target Extracellular Matrix, Vascular Networks, and Immunosuppressive Cells". en. *Pharmaceuticals* 17.12 (Dec. 2024), p. 1663. DOI: 10.3390/ph17121663.
- [10] K. E. De Visser and J. A. Joyce. "The evolving tumor microenvironment: From cancer initiation to metastatic outgrowth". en. *Cancer Cell* 41.3 (Mar. 2023), pp. 374–403. DOI: 10.1016/j.ccell.2023.02.016.
- [11] G. R. Bhat, I. Sethi, H. Q. Sadida, B. Rah, R. Mir, N. Algehainy, I. A. Albalawi, T. Masoodi, G. K. Subbaraj, F. Jamal, M. Singh, R. Kumar, M. A. Macha, S. Uddin, A. S. A.-S. Akil, M. Haris, and A. A. Bhat. "Cancer cell plasticity: from cellular, molecular, and genetic mechanisms to tumor heterogeneity and drug resistance". en. *Cancer and Metastasis Reviews* 43.1 (Mar. 2024), pp. 197–228. DOI: 10.1007/s10555-024-10172-z.
- [12] M. Sinkala. "Mutational landscape of cancer-driver genes across human cancers". en. Scientific Reports 13.1 (Aug. 2023), p. 12742. DOI: 10.1038/s41598-023-39608-2.
- [13] K. Sheva, S. Roy Chowdhury, N. Kravchenko-Balasha, and A. Meirovitz. "Molecular Changes in Breast Cancer Induced by Radiation Therapy". en. *International Journal of Radiation Oncology*Biology*Physics* 120.2 (Oct. 2024), pp. 465–481. DOI: 10.1016/j.ijrobp.2024.03.019.
- [14] F. Bray, M. Laversanne, H. Sung, J. Ferlay, R. L. Siegel, I. Soerjomataram, and A. Jemal. "Global cancer statistics 2022: GLOBOCAN estimates of incidence and mortality worldwide for 36 cancers in 185 countries". en. *CA: A Cancer Journal for Clinicians* 74.3 (May 2024), pp. 229–263. DOI: 10.3322/caac.21834.
- [15] E. Orrantia-Borunda, P. Anchondo-Nuñez, L. E. Acuña-Aguilar, F. O. Gómez-Valles, and C. A. Ramírez-Valdespino. "Subtypes of Breast Cancer". Breast Cancer. Ed. by Department of Medical Education, Dr. Kiran C. Patel College of Allopathic Medicine, Nova Southeastern University, FL, USA and H. N. Mayrovitz. Exon Publications, Aug. 2022, pp. 31–42. DOI: 10.36255/exon-publications-breast-cancer-subtypes.

- [16] P. Zagami and L. A. Carey. "Triple negative breast cancer: Pitfalls and progress".
 en. npj Breast Cancer 8.1 (Aug. 2022), p. 95. DOI: 10.1038/s41523-022-00468-0.
- [17] H. Rosado-Galindo and M. Domenech. "Surface roughness modulates EGFR signaling and stemness of triple-negative breast cancer cells". en. Frontiers in Cell and Developmental Biology 11 (Mar. 2023), p. 1124250. DOI: 10.3389/fcell. 2023.1124250.
- [18] E. Topalan, A. Büyükgüngör, M. Çiğdem, S. Güra, B. Sever, M. Otsuka, M. Fujita, H. Demirci, and H. Ciftci. "A Structural Insight Into Two Important ErbB Receptors (EGFR and HER2) and Their Relevance to Non-Small Cell Lung Cancer". en. Archiv der Pharmazie 358.4 (Apr. 2025), e2400992. DOI: 10.1002/ardp.202400992.
- [19] M. E. Bahar, H. J. Kim, and D. R. Kim. "Targeting the RAS/RAF/MAPK pathway for cancer therapy: from mechanism to clinical studies". en. Signal Transduction and Targeted Therapy 8.1 (Dec. 2023), p. 455. DOI: 10.1038/s41392-023-01705-z.
- [20] A. Paye, A. Truong, C. Yip, J. Cimino, S. Blacher, C. Munaut, D. Cataldo, J. M. Foidart, E. Maquoi, J. Collignon, P. Delvenne, G. Jerusalem, A. Noel, and N. E. Sounni. "EGFR Activation and Signaling in Cancer Cells Are Enhanced by the Membrane-Bound Metalloprotease MT4-MMP". en. Cancer Research 74.23 (Dec. 2014), pp. 6758–6770. DOI: 10.1158/0008-5472.CAN-13-2994.
- [21] F. Huang, F. Santinon, R. E. Flores González, and S. V. Del Rincón. "Melanoma Plasticity: Promoter of Metastasis and Resistance to Therapy". en. *Frontiers in Oncology* 11 (Sept. 2021), p. 756001. DOI: 10.3389/fonc.2021.756001.
- [22] S. Diazzi, S. Tartare-Deckert, and M. Deckert. "The mechanical phenotypic plasticity of melanoma cell: an emerging driver of therapy cross-resistance". en. *Onco-genesis* 12.1 (Feb. 2023), p. 7. DOI: 10.1038/s41389-023-00452-8.
- [23] J. B. Heistein, U. Acharya, and S. K. R. Mukkamalla. "Malignant Melanoma". eng. *StatPearls*. Treasure Island (FL): StatPearls Publishing, 2025.
- [24] K. H. Lee, H. Y. Suh, M. W. Lee, W. J. Lee, and S. E. Chang. "Prognostic Significance of Epidermal Growth Factor Receptor Expression in Distant Metastatic Melanoma from Primary Cutaneous Melanoma". en. Annals of Dermatology 33.5 (2021), p. 432. DOI: 10.5021/ad.2021.33.5.432.

- [25] S. D'Aguanno, F. Mallone, M. Marenco, D. Del Bufalo, and A. Moramarco. "Hypoxia-dependent drivers of melanoma progression". en. *Journal of Experimental & Clinical Cancer Research* 40.1 (May 2021), p. 159. DOI: 10.1186/s13046-021-01926-6.
- [26] J. Pastwińska, K. Karaś, I. Karwaciak, and M. Ratajewski. "Targeting EGFR in melanoma The sea of possibilities to overcome drug resistance". en. *Biochimica et Biophysica Acta (BBA) Reviews on Cancer* 1877.4 (July 2022), p. 188754. DOI: 10.1016/j.bbcan.2022.188754.
- [27] A. Zafar, S. Khatoon, M. J. Khan, J. Abu, and A. Naeem. "Advancements and limitations in traditional anti-cancer therapies: a comprehensive review of surgery, chemotherapy, radiation therapy, and hormonal therapy". en. *Discover Oncology* 16.1 (Apr. 2025), p. 607. DOI: 10.1007/s12672-025-02198-8.
- [28] S. U. Khan, K. Fatima, S. Aisha, and F. Malik. "Unveiling the mechanisms and challenges of cancer drug resistance". en. *Cell Communication and Signaling* 22.1 (Feb. 2024), p. 109. DOI: 10.1186/s12964-023-01302-1.
- [29] R. Riera, J. Tauler, N. Feiner-Gracia, S. Borrós, C. Fornaguera, and L. Albertazzi. "Complex pBAE Nanoparticle Cell Trafficking: Tracking Both Position and Composition Using Super Resolution Microscopy". en. *ChemMedChem* 17.13 (July 2022), e202100633. DOI: 10.1002/cmdc.202100633.
- [30] N. Segovia, P. Dosta, A. Cascante, V. Ramos, and S. Borrós. "Oligopeptide-terminated poly(-amino ester)s for highly efficient gene delivery and intracellular localization". en. *Acta Biomaterialia* 10.5 (May 2014), pp. 2147–2158. DOI: 10.1016/j.actbio.2013.12.054.
- [31] M. Navalón-López, A. Dols-Perez, S. Grijalvo, C. Fornaguera, and S. Borrós. "Unravelling the role of individual components in pBAE/polynucleotide polyplexes in the synthesis of tailored carriers for specific applications: on the road to rational formulations". en. *Nanoscale Advances* 5.6 (2023), pp. 1611–1623. DOI: 10.1039/D2NA00800A.
- [32] L. Martínez-Jothar, S. Doulkeridou, R. M. Schiffelers, J. Sastre Torano, S. Oliveira, C. F. Van Nostrum, and W. E. Hennink. "Insights into maleimide-thiol conjugation chemistry: Conditions for efficient surface functionalization of nanoparticles for receptor targeting". en. *Journal of Controlled Release* 282 (July 2018), pp. 101–109. DOI: 10.1016/j.jconrel.2018.03.002.

- [33] J. Dong, P. L. Carpinone, G. Pyrgiotakis, P. Demokritou, and B. M. Moudgil. "Synthesis of Precision Gold Nanoparticles Using Turkevich Method". en. *KONA Powder and Particle Journal* 37.0 (Jan. 2020), pp. 224–232. DOI: 10.14356/kona.2020011.
- [34] A. R. Rastinehad, H. Anastos, E. Wajswol, J. S. Winoker, J. P. Sfakianos, S. K. Doppalapudi, M. R. Carrick, C. J. Knauer, B. Taouli, S. C. Lewis, A. K. Tewari, J. A. Schwartz, S. E. Canfield, A. K. George, J. L. West, and N. J. Halas. "Gold nanoshell-localized photothermal ablation of prostate tumors in a clinical pilot device study". en. *Proceedings of the National Academy of Sciences* 116.37 (Sept. 2019), pp. 18590–18596. DOI: 10.1073/pnas.1906929116.
- [35] K. Kozics, M. Sramkova, K. Kopecka, P. Begerova, A. Manova, Z. Krivosikova, Z. Sevcikova, A. Liskova, E. Rollerova, T. Dubaj, V. Puntes, L. Wsolova, P. Simon, J. Tulinska, and A. Gabelova. "Pharmacokinetics, Biodistribution, and Biosafety of PEGylated Gold Nanoparticles In Vivo". en. Nanomaterials 11.7 (June 2021), p. 1702. DOI: 10.3390/nano11071702.
- [36] X. Li, B. Wang, S. Zhou, W. Chen, H. Chen, S. Liang, L. Zheng, H. Yu, R. Chu, M. Wang, Z. Chai, and W. Feng. "Surface chemistry governs the sub-organ transfer, clearance and toxicity of functional gold nanoparticles in the liver and kidney". en. Journal of Nanobiotechnology 18.1 (Dec. 2020), p. 45. DOI: 10.1186/s12951-020-00599-1.
- [37] R. Wang, B. Hu, Z. Pan, C. Mo, X. Zhao, G. Liu, P. Hou, Q. Cui, Z. Xu, W. Wang, Z. Yu, L. Zhao, M. He, Y. Wang, C. Fu, M. Wei, and L. Yu. "Antibody–Drug Conjugates (ADCs): current and future biopharmaceuticals". en. *Journal of Hematology & Oncology* 18.1 (Apr. 2025), p. 51. DOI: 10.1186/s13045-025-01704-3.
- [38] M. Sharifi, W. C. Cho, A. Ansariesfahani, R. Tarharoudi, H. Malekisarvar, S. Sari, S. H. Bloukh, Z. Edis, M. Amin, J. P. Gleghorn, T. L. M. T. Hagen, and M. Falahati. "An Updated Review on EPR-Based Solid Tumor Targeting Nanocarriers for Cancer Treatment". en. Cancers 14.12 (June 2022), p. 2868. DOI: 10.3390/cancers14122868.
- [39] H. Cheng, J. Liao, Y. Ma, M. T. Sarwar, and H. Yang. "Advances in targeted therapy for tumor with nanocarriers: A review". en. *Materials Today Bio* 31 (Apr. 2025), p. 101583. DOI: 10.1016/j.mtbio.2025.101583.

- [40] E. Y. Yang and K. Shah. "Nanobodies: Next Generation of Cancer Diagnostics and Therapeutics". en. *Frontiers in Oncology* 10 (July 2020), p. 1182. DOI: 10. 3389/fonc.2020.01182.
- [41] M. Blueggel, D. Gül, R. H. Stauber, and S. K. Knauer. "Small but mighty: the versatility of nanobodies in modern medicine". en. *Nanoscale Horizons* 10.10 (2025), pp. 2158–2171. DOI: 10.1039/D5NH00283D.
- [42] M. H. Abdolvahab, P. Karimi, N. Mohajeri, M. Abedini, and H. Zare. "Targeted drug delivery using nanobodies to deliver effective molecules to breast cancer cells: the most attractive application of nanobodies". en. *Cancer Cell International* 24.1 (Feb. 2024), p. 67. DOI: 10.1186/s12935-024-03259-8.
- [43] J. Karlsson, K. R. Rhodes, J. J. Green, and S. Y. Tzeng. "Poly(beta-amino ester)s as gene delivery vehicles: challenges and opportunities". en. Expert Opinion on Drug Delivery 17.10 (Oct. 2020), pp. 1395–1410. DOI: 10.1080/17425247.2020. 1796628.
- [44] P. Dosta, N. Segovia, A. Cascante, V. Ramos, and S. Borrós. "Surface charge tunability as a powerful strategy to control electrostatic interaction for high efficiency silencing, using tailored oligopeptide-modified poly(beta-amino ester)s (PBAEs)". en. *Acta Biomaterialia* 20 (July 2015), pp. 82–93. DOI: 10.1016/j.actbio.2015.03.029.
- [45] J. R. Magaña Rodriguez, M. Guerra-Rebollo, S. Borrós, and C. Fornaguera. "Nucleic acid-loaded poly(beta-aminoester) nanoparticles for cancer nano-immuno therapeutics: the good, the bad, and the future". en. *Drug Delivery and Translational Research* 14.12 (Dec. 2024), pp. 3477–3493. DOI: 10.1007/s13346-024-01585-y.
- [46] A. Gandini. "The furan/maleimide Diels-Alder reaction: A versatile click-unclick tool in macromolecular synthesis". en. *Progress in Polymer Science* 38.1 (Jan. 2013), pp. 1–29. DOI: 10.1016/j.progpolymsci.2012.04.002.
- [47] J. Keeler. "Understanding NMR Spectroscopy". en ().
- [48] S. Munawar, A. F. Zahoor, S. M. Hussain, S. Ahmad, A. Mansha, B. Parveen, K. G. Ali, and A. Irfan. "Steglich esterification: A versatile synthetic approach toward the synthesis of natural products, their analogues/derivatives". en. *Heliyon* 10.1 (Jan. 2024), e23416. DOI: 10.1016/j.heliyon.2023.e23416.

- [49] A. Morinval and L. Avérous. "Responsive sustainable and biodegradable systems based on Diels-Alder reaction from amylomaize starch". en. *European Polymer Journal* 198 (Oct. 2023), p. 112391. DOI: 10.1016/j.eurpolymj.2023.112391.
- [50] T. Dispinar, R. Sanyal, and A. Sanyal. "A Diels-Alder/retro Diels-Alder strategy to synthesize polymers bearing maleimide side chains". en. *Journal of Polymer Science Part A: Polymer Chemistry* 45.20 (Oct. 2007), pp. 4545–4551. DOI: 10. 1002/pola.22299.
- [51] B. E. Kirkpatrick, K. S. Anseth, and T. S. Hebner. "Diverse reactivity of maleimides in polymer science and beyond". en. *Polymer International* 74.4 (Apr. 2025), pp. 296–306. DOI: 10.1002/pi.6715.
- [52] R. Gheneim, C. Perez-Berumen, and A. Gandini. "DielsAlder Reactions with Novel Polymeric Dienes and Dienophiles: Synthesis of Reversibly Cross-Linked Elastomers". en. *Macromolecules* 35.19 (Sept. 2002), pp. 7246–7253. DOI: 10. 1021/ma020343c.
- [53] V. Tsikaris, M. Sakarellos-Daitśiotis, E. Panou-Pomonis, E. Detsikas, C. Sakarellos, M. T. Cung, and M. Marraud. "1H-NMR studies on arginine tripeptides: evidence for guanidinium-C-terminal carboxylate interactions". eng. *Peptide Research* 5.2 (1992), pp. 110–114.
- [54] Y. Liu, L. Scrivano, J. D. Peterson, M. H. A. M. Fens, I. B. Hernández, B. Mesquita, J. S. Toraño, W. E. Hennink, C. F. Van Nostrum, and S. Oliveira. "EGFR-Targeted Nanobody Functionalized Polymeric Micelles Loaded with mTHPC for Selective Photodynamic Therapy". en. *Molecular Pharmaceutics* 17.4 (Apr. 2020), pp. 1276–1292. DOI: 10.1021/acs.molpharmaceut.9b01280.
- [55] W. Kang, C. Ding, D. Zheng, X. Ma, L. Yi, X. Tong, C. Wu, C. Xue, Y. Yu, and Q. Zhou. "Nanobody Conjugates for Targeted Cancer Therapy and Imaging". en. Technology in Cancer Research & Treatment 20 (Jan. 2021), p. 15330338211010117. DOI: 10.1177/15330338211010117.
- [56] J. Rodriguez-Loya, M. Lerma, and J. L. Gardea-Torresdey. "Dynamic Light Scattering and Its Application to Control Nanoparticle Aggregation in Colloidal Systems: A Review". en. *Micromachines* 15.1 (Dec. 2023), p. 24. DOI: 10.3390/mi15010024.

- [57] M. Keeney, S.-G. Ong, A. Padilla, Z. Yao, S. Goodman, J. C. Wu, and F. Yang. "Development of Poly(-amino ester)-Based Biodegradable Nanoparticles for Non-viral Delivery of Minicircle DNA". en. ACS Nano 7.8 (Aug. 2013), pp. 7241–7250. DOI: 10.1021/nn402657d.
- [58] B. S. Mesquita, M. H. A. M. Fens, A. Di Maggio, E. D. C. Bosman, W. E. Hennink, M. Heger, and S. Oliveira. "The Impact of Nanobody Density on the Targeting Efficiency of PEGylated Liposomes". en. *International Journal of Molecular Sci*ences 23.23 (Nov. 2022), p. 14974. DOI: 10.3390/ijms232314974.
- [59] P. Kesharwani, R. Ma, L. Sang, M. Fatima, A. Sheikh, M. A. S. Abourehab, N. Gupta, Z.-S. Chen, and Y. Zhou. "Gold nanoparticles and gold nanorods in the landscape of cancer therapy". en. *Molecular Cancer* 22.1 (June 2023), p. 98. DOI: 10.1186/s12943-023-01798-8.
- [60] K. Mahato, S. Nagpal, M. A. Shah, A. Srivastava, P. K. Maurya, S. Roy, A. Jaiswal, R. Singh, and P. Chandra. "Gold nanoparticle surface engineering strategies and their applications in biomedicine and diagnostics". en. 3 Biotech 9.2 (Feb. 2019), p. 57. DOI: 10.1007/s13205-019-1577-z.
- [61] A. Anaki, C. Tzror-Azankot, M. Motiei, T. Sadan, and R. Popovtzer. "Impact of synthesis methods on the functionality of antibody-conjugated gold nanoparticles for targeted therapy". en. *Nanoscale Advances* 6.21 (2024), pp. 5420–5429. DOI: 10.1039/D4NA00134F.
- [62] V. Borse and A. N. Konwar. "Synthesis and characterization of gold nanoparticles as a sensing tool for the lateral flow immunoassay development". en. *Sensors International* 1 (2020), p. 100051. DOI: 10.1016/j.sintl.2020.100051.
- [63] H. Jans, X. Liu, L. Austin, G. Maes, and Q. Huo. "Dynamic Light Scattering as a Powerful Tool for Gold Nanoparticle Bioconjugation and Biomolecular Binding Studies". en. Analytical Chemistry 81.22 (Nov. 2009), pp. 9425–9432. DOI: 10. 1021/ac901822w.
- [64] R. T. Busch, F. Karim, J. Weis, Y. Sun, C. Zhao, and E. S. Vasquez. "Optimization and Structural Stability of Gold Nanoparticle-Antibody Bioconjugates". en. ACS Omega 4.12 (Sept. 2019), pp. 15269–15279. DOI: 10.1021/acsomega. 9b02276.
- [65] E. Koushki. "Effect of conjugation with organic molecules on the surface plasmon resonance of gold nanoparticles and application in optical biosensing". en. RSC Advances 11.38 (2021), pp. 23390–23399. DOI: 10.1039/D1RA01842F.

- [66] M. Ghasemi, T. Turnbull, S. Sebastian, and I. Kempson. "The MTT Assay: Utility, Limitations, Pitfalls, and Interpretation in Bulk and Single-Cell Analysis". en. *International Journal of Molecular Sciences* 22.23 (Nov. 2021), p. 12827. DOI: 10.3390/ijms222312827.
- [67] C. Andraos, I. J. Yu, and M. Gulumian. "Interference: A Much-Neglected Aspect in High-Throughput Screening of Nanoparticles". en. *International Journal of Toxicology* 39.5 (Sept. 2020), pp. 397–421. DOI: 10.1177/1091581820938335.
- [68] S. Iqbal, A. F. Martins, M. Sohail, J. Zhao, Q. Deng, M. Li, and Z. Zhao. "Synthesis and Characterization of Poly (-amino Ester) and Applied PEGylated and Non-PEGylated Poly (-amino ester)/Plasmid DNA Nanoparticles for Efficient Gene Delivery". en. Frontiers in Pharmacology 13 (Apr. 2022), p. 854859. DOI: 10.3389/fphar.2022.854859.
- [69] W. Mu, S. Homann, C. Hofmann, A. Gorin, D. Huynh, O. Yang, and T. Kelesidis. "A Flow Cytometric Method to Determine Transfection Efficiency". en. BIO-PROTOCOL 9.10 (2019). DOI: 10.21769/BioProtoc.3244.
- [70] J. J. Uusitalo, H. I. Ingólfsson, P. Akhshi, D. P. Tieleman, and S. J. Marrink. "Martini Coarse-Grained Force Field: Extension to DNA". en. *Journal of Chemical Theory and Computation* 11.8 (Aug. 2015), pp. 3932–3945. DOI: 10.1021/acs.jctc.5b00286.
- [71] J. J. Uusitalo, H. I. Ingólfsson, S. J. Marrink, and I. Faustino. "Martini Coarse-Grained Force Field: Extension to RNA". en. *Biophysical Journal* 113.2 (July 2017), pp. 246–256. DOI: 10.1016/j.bpj.2017.05.043.
- [72] V.-K. Tran-Nguyen and A.-C. Camproux. "Computational modeling of protein-ligand interactions: From binding site identification to pose prediction and beyond". en. *Current Opinion in Structural Biology* 95 (Dec. 2025), p. 103152. DOI: 10.1016/j.sbi.2025.103152.
- [73] N. Wu, R. Zhang, X. Peng, L. Fang, K. Chen, and J. S. Jestilä. "Elucidation of protein–ligand interactions by multiple trajectory analysis methods". en. *Physical Chemistry Chemical Physics* 26.8 (2024), pp. 6903–6915. DOI: 10.1039/D3CP03492E.
- [74] H. Feng, X. Sun, N. Li, Q. Xu, Q. Li, S. Zhang, G. Xing, G. Zhang, and F. Wang. "Machine Learning-Driven Methods for Nanobody Affinity Prediction". en. ACS Omega 9.48 (Dec. 2024), pp. 47893–47902. DOI: 10.1021/acsomega.4c09718.

[75] T. Subramaniam, S. A. Mualif, W. H. Chan, and K. B. Abd Halim. "Unlocking the potential of in silico approach in designing antibodies against SARS-CoV-2". en. *Frontiers in Bioinformatics* 5 (Feb. 2025), p. 1533983. DOI: 10.3389/fbinf. 2025.1533983.